Alma Mater Studiorum · Università di Bologna

Scuola di Scienze
Corso di Laurea Magistrale in Fisica del Sistema Terra

STUDY OF THE 2016 CENTRAL ITALY POST SEISMIC DISPLACEMENT THROUGH AN INDEPENDENT COMPONENT ANALYSIS

Relatore:
Prof. Maria Elina Belardinelli

Correlatore:
Dott. Enrico Serpelloni

Presentata da:
Eugenio Mandler

Sessione II
Anno Accademico 2018/2019

Abstract

Tra l'Agosto e l'Ottobre 2016 una serie di terremoti moderati ha colpito l'Italia centrale. Gli epicentri degli eventi principali sono enucleati vicino i paesi di Amatrice, Visso e Norcia, perciò questa sequenza sismica è anche conosciuta come *sequenza di Amatrice-Visso-Norcia*. Lo scopo di questa tesi è quello di tracciare una mappa afterslip attraverso lo studio della deformazione post-sismica misurata dal Global Positioning System (GPS).

Il primo passo necessario per raggiungere questo obiettivo è la detrendizzazione delle serie temporali geodetiche, che rappresentano l'evoluzione spaziale della posizione di punti sulla superficie terrestre misurata dalle stazioni GPS presenti. Successivamente è stata eseguita una "Independent Component Analysis" (ICA) della distribuzione spazio-temporale del campo di spostamento. L'ICA è una tecnica di analisi statistica multivariata che permette di ricostruire e separare le sorgenti fisiche che producono lo spostamento misurato. Nello specifico, tramite una ICA, è possibile decomporre il segnale geodetico in un numero fissato di Componenti Indipendenti (IC). Il vincolo di indipendenza statistica permette di distinguere meglio gli effetti (segnali) delle diverse sorgenti fisiche che hanno prodotto il dataset, rispetto ad altre tecniche di statistca multivariata.

Lo step finale richiede l'inversione della distribuzione spaziale del segnale post sismico, che nel nostro caso è stato mappato nella prima componente indipendente (IC1) e interpretato come dovuto ad afterslip su faglia. Per fare ciò è necessario fissare la geometria della sorgente sismica che è stata interessata da afterslip, ovverosia quali faglie sono state attivate durante la fase postsismica della sequenza. A tal fine si sono considerate le strutture risultanti dai principali studi cosismici condotti sulla sequenza dell'Italia centrale del 2016 (scegliendo quelle suggerite da lavori basati sul dataset più completo, la cui superficie è stata estesa lungo la direzione di strike e di dip. L'inversione è stata eseguita tramite il codice Matlab ICA Inversion Method (ICAIM) sviluppato da A. Gualandi (Gualandi, 2015) come una estensione del codice PCAIM (cioè Principal Component Analysis-based Inversion Method) sviluppato al California Institute of Technology (CalTech) (Kositsky and Avouac, 2010).

Il risultato finale consiste in una mappa della distribuzione di afterslip sulle faglie considerate, con aree attivate nella fase post sismica compatibili con le zone coinvolte nella fase cosismica e con la distribuzione di sismicità.

A quanto risulta finora, questo è il primo tentativo di vincolare il segnale post sismico della sequenza dell'Italia centrale del 2016.

Contents

Chapter 1

Introduction

The *Amatrice-Visso-Norcia* or *2016 Central Italy* seismic sequence started on August the 24^{th} with an earthquake located nearby the town of Amatrice. In the following months two more mainshocks occurred near Visso (on October the 26^{th}) and Norcia (on October the 30^{th}), the latter being the most intense of the sequence with a $M_w = 6.5$.

In this thesis we focused on the post seismic phase of the sequence, with the aim of constructing a map of afterslip distribution. To achieve this, we exploited the displacement recorded by the available GPS networks which were analyzed through an *Independent Component Analysis*. As far as we know this is the first study carried out on the post-seismic deformation of the Amatrice-Visso-Norcia seismic sequence.

The thesis is structured as follows:

- *This first chapter* introduces to the key concepts that will be used throughout the work. Contextually a short description of post-seismic effects is given, focusing on the afterslip mechanisms.
- in the *second chapter* we go through the main co-seismic studies conducted on this subject. This is done for both selecting the geometry of faults and comparing our post-seismic solution to the coseismic ones.
- *Third chapter* deals with the dataset description and ICAIM theoretical principles. Here the steps taken up to the inversion are described more in detail.
- *Forth chapter* embeds the inversion step description and the outcomes.
- in the *Fifth chapter* conclusions are drawn.

1.1 Faults as earthquakes sources

Faults are discontinuities of the displacement field within the crust. The displacement discontinuity may occur during earthquakes both seismically or aseismically. For this reason they are also called as earthquake sources. They are generally depicted through a planar surface separating two blocks (the "crustal blocks"), the one above is called *hanging wall* whereas the one beneath is the *foot wall*. The parameters that describe a fault are (1.1)

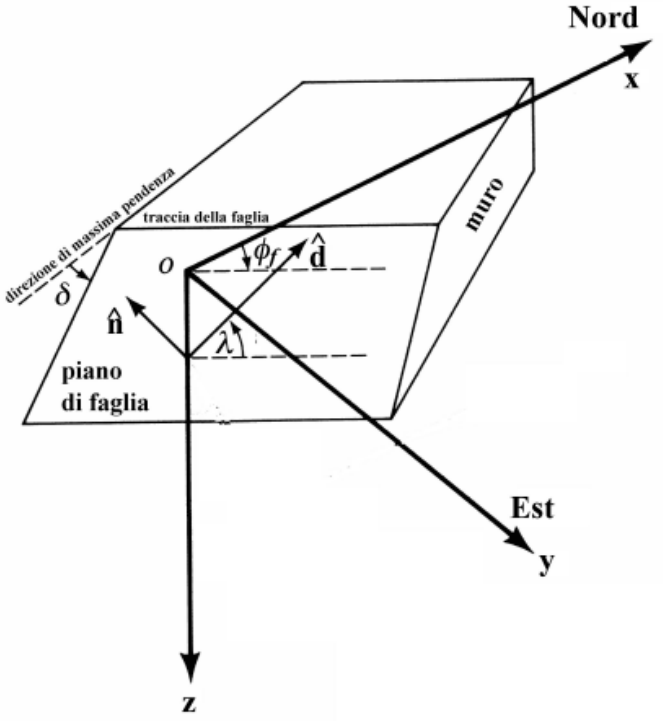

Figure 1.1. Figures summarizes the fault's features, namely trace, slip direction ($\hat{d}$), strike angle (Φ_f), dip angle (δ) and rake angle (λ). $\hat{n}$ is the normal versor to the fault plane.

1. **slip** ($\overrightarrow{\Delta u} = \Delta u \hat{d}$): the displacement discontinuity, i.e. the relative motion of the hanging wall with respect to the foot wall (i.e. "muro" in fig. 1.1), is given by the slip vector which is tangent to fault surface..

2. **trace**: namely the "traccia della faglia" in fig. 1.1, it is the line that describes the intersection between the fault plane (i.e. "piano di faglia" in fig. 1.1) and the earth's surface. It is oriented with the hanging wall laying on its right side.

3. **strike** (Φ_f): it is the clockwise angle ($0 < \Phi_f < 2\pi$) measured on the Earth surface, between the north and trace direction.

4. **dip** (δ): it is the angle between the surface and the fault plane ($0 < \delta < \pi/2$).
5. **rake** (λ): it is the counterclockwise angle between the slip and the strike direction ($-\pi < \delta < +\pi$).

Different types of fault exist depending on the tectonic framework. On the whole they can be grouped in three main types: *normal faults*, *thrust or reverse faults* and *strike-slip faults*.

Normal faults are found in extensional regions, the hanging wall moves downwards with respect to the foot wall. On the other hand, thrusts are found in compressional areas and the hanging wall moves upwards with respect to the foot wall. Normal faults and thrusts are also called "dip-slip" faults, as slip occurs in the direction of dip. Strike-slip faults (slip towards or opposite to the strike direction) are characterized by plates sliding horizontally. It has to be noticed that this is an ideal classification since faults usually show a mixed behaviour.

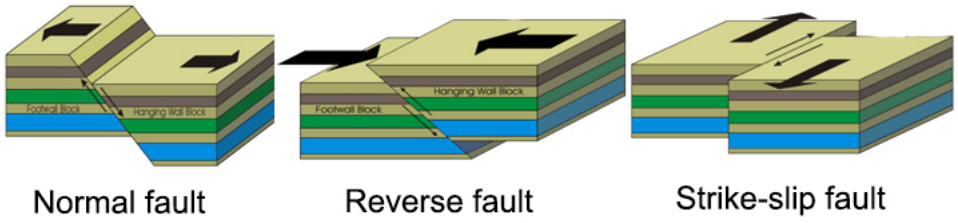

Figure 1.2. Figures portaits the three main classes of faults: normal faults, thrusts and strike-slip faults. Thick black arrows show the direction of principal stress vector.

In a seismic system, minor faults are often associated with major or principal faults. We refer to such smaller faults as to *synthetic* and *antithetic* faults. Synthetic faults dip in the same direction as the major fault while the antithetic faults dip in the opposite direction.

The most common way used to assess the dimension of an earthquake is the *moment magnitude* M_W. It relies on the scalar momentum M_0 associated with the earthquake, which is given by the elastic parameter μ (i.e. the rigidity modulus) times a pseudo-volume (i.e. the amount of slip Δu times the area A of the fault which slipped):

$$M_0 = \mu \times \Delta u \times A \tag{1.1}$$

The relation among the magnitude and the moment taken into account for the study area is the empirical relation:

$$M_W = \frac{2}{3}\Big(logM_0 - 9.05\Big) \tag{1.2}$$

as in Hans and Kanamori (1979).

1.2 Seismic cycle

The 2016 seismic sequence was characterized by three main events in a time range of ~ 3 months. Generally speaking, earthquakes are characterized by a *seismic cycle*. The term "cycle" refers to the fact that they repeteadly rupture a certain fault, even though it does not imply either periodicity or regularity. A seismic cycle can be divided into three phases: *inter-seismic phase*, *co-seismic phase* and *post-seismic phase* (figure 1.3).

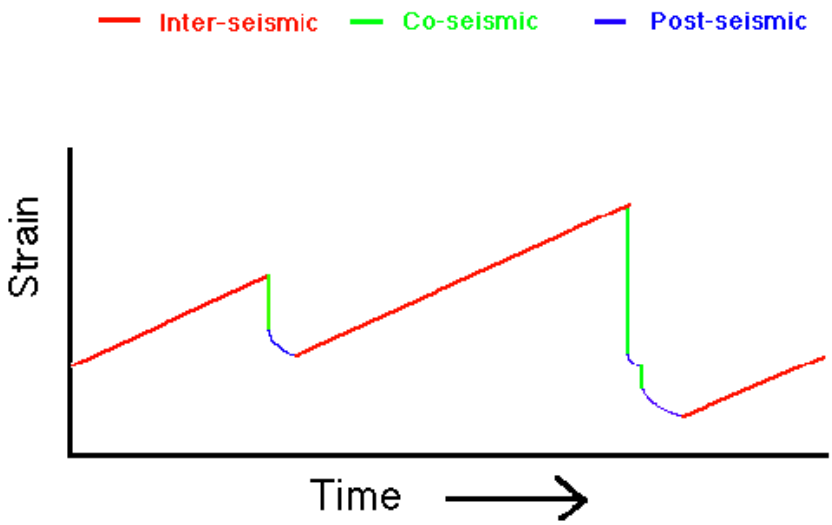

Figure 1.3. Figure shows strain evolution during a seismic cycle in the inter-seismic phase (red lines), co-seismic phase (green lines) and post-seismic phase (blue lines)

- **Inter-seismic phase**: in this phase, which spans in the time range between one earthquake and another, strain is accumulated steadly. This phase occurs when the fault is locked by friction.

- **Co-seismic phase**: in this phase faults slip istantaneously (on a time range $\sim seconds - minutes$), during the earthquake. Such phase occurs when the accumulated stress exceeds friction capability to keep the fault locked.
- **Post-seismic phase**: in this phase, which occurs after an earthquake, faults slip aseismically on a time scale ranging from days to years. Various mechanisms contribute to slip during this period of time as it will be described more in detail in the following section (1.3).

The simpliest representation of a seismic cycle can be given through the 1D spring-slider (figure 1.4) :

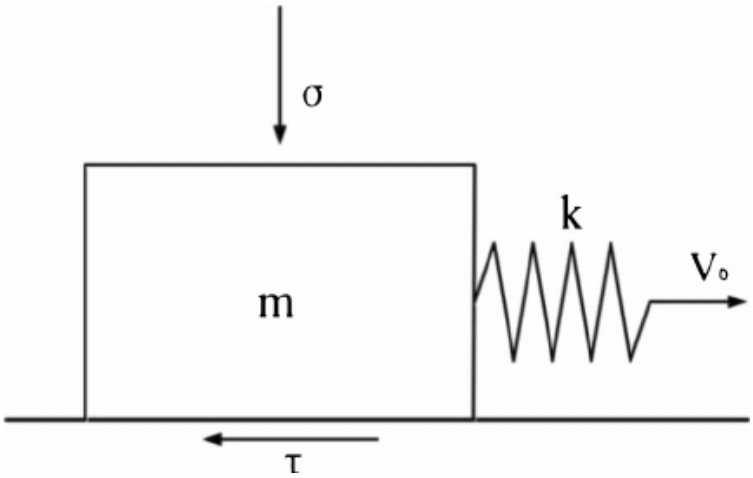

Figure 1.4. The block m stands for the locked area of the fault (i.e. the asperity), σ is the normal stress that keeps the asperity locked, k represents the elasticity of the medium, v_0 is the sliding velocity during the inter-seismic phase, τ is the friction which opposes to sliding.

During the inter-seismic phase plates slide at a constant velocity (v_0) deforming the elastic medium (i.e. elonging the spring) and shear stress builds up. The elasticity of the medium (represented by k) can be derived from crack theory:

$$k = \frac{G}{H} \tag{1.3}$$

where G is the medium rigidity modulus and H a typical lenght for the fault.

When the frictional locking (exerted by σ) is outstripped the block istantaneously slides recovering the accumulated deformation and comes back to a state of equilibrium (co-seismic phase). Afterwards, plates start sliding and the cycle begins all over again.

Although here it is not considered, the co-seismic phase is followed by a post-seismic slipping. Noteworthy, as the asperities (i.e. the locked areas of the fault) relax stress in the coseismic phase, slip during the post-seismic phase occurs (aseismically) out of these regions.

1.3 Post-seismic deformation

The effects that follow an earthquake range from aftershocks occurring in the area struck by the main event and anomalies related to groundwater and deformation, to the triggering of other earthquakes in locations at hundreds of kilometers apart. If, on the one hand, coseismic stress changes seem too small to induce such aftereffects at large distances, on the other hand, as relaxation of stress takes place, significant stress changes can occur in the seismogenetic layer even at distant locations.

In the following figure, taken from Rice and Gu (1983) work, effects following a major earthquake are summed up:

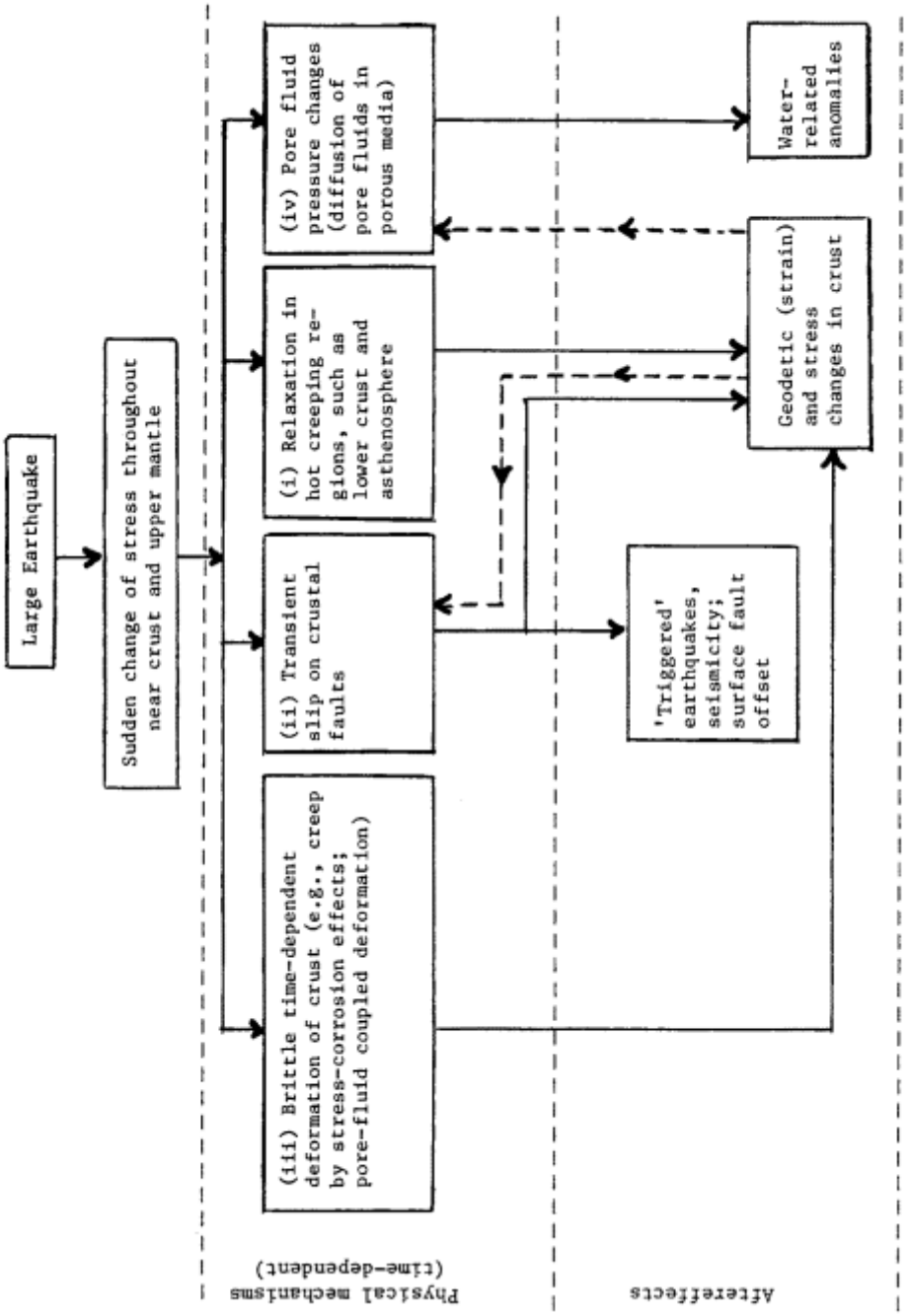

Figure 1.5. Aftereffects following major earthquakes from Rice and Gu (1983) work

- The upper panels describe the effects caused by the earthquake, namely the reduction of stress in the hypocentral area and its redistribution in adjacent regions.
- The central panels describe the mechanisms activated by the stress change:

1. *Relaxation in hot creeping regions*, generally the asthenosphere (100 < depth < 300 km) and, if temperature is high enough, the lower crust (avarage depth < 35 km). Stress migrates to these regions which, relaxing, produce a time-dependent restressing of the fault surface close to the ruptured zone.
2. *Transient or time-dependent slip on crustal faults* is activated by sudden change in stress and may either accelerate to instability (causing aftershocks) or definitely be halted as during aseismic slip or afterslip.
3. *Brittle deformation of the crust* is a time-dependent anelastic deformation that can be activated at high stress levels owing to microcracking. Besides that, pore-fluid diffusion may lead to time-dependent straining in porous rocks too.
4. *Pore fluid pressure changes* are induced by fluid time-dependent motions (diffusion). This mechanism is related to the previous one, but here the time dependent motion of fluid is highlighted rather than rock deformation.

- Finally in the lower panels we find the observable effects caused by these mechanisms. Such aftereffects will not result from just one mechanism as lines in figure show.

To sum up, the major mechanisms held responsible for the post seismic deformation are *visco-elastic relaxation*, *poro-elastic deformation* and *afterslip*. In the next section we will focus on the latter as visco-elastic relaxation occurs on a different time scale than the other two mechanisms (longer than the time span considered in this thesis), and poro-elastic deformation is hard to detect with the GPS network employed in this thesis because it usually confined in near-field (e.g. Nespoli et al. 2018).

1.4 Afterslip

It has been shown through laboratory experiments that the *frictional process* (or *rheology*) that describes slip on faults at low temperatures (at depths < 15 km) depends on the rate of sliding (i.e. slip velocity) and the state of contact of asperities. Such laws go by the name of *rate and state dependent friction laws*. As a matter of fact, at $T < 250$ °C faults are thought to have a stick slip behaviour, whereas at 250 °C < T < 400 °C (Perfettini and Avouac, 2004) they show a brittle creep behaviour. Stick slip models are characterized by a static phase during which potential energy is gathered, and a dynamic phase in which it is released in the form of kinetic energy and heat. The simpliest example is the 1-D spring-slider system already mentioned in the introduction (fig 1.4).

Models of this micromechanical process are explored in Marone at al. (1990); Sleep (1995,1997); Segall and Rice (1995); Main (2000).

Rate and state friction laws are consistent with brittle creep formalism as we will see later on.

Such laws, in the Dieterich-Ruina formulation, are:

$$\tau_f(v,\theta) = \sigma \left[\mu + a\, ln\left(\frac{v}{v_*}\right) + b\, ln\left(\theta\frac{v_*}{d_c}\right)\right] \tag{1.4}$$

where τ_f is the frictional resistance to sliding (i.e. τ in figure 1.4) ; σ is the normal stress; v is the sliding velocity; θ is a variable describing the state of the surface; μ is the friction coefficient at steady reference velocity (v_*); a, b are some laboratory derived constants; d_c is the critical distance, namely a typical size of asperities.

The evolution of the state variable is described through the equation:

$$\frac{d\theta}{dt} = 1 - \frac{v\theta}{d_c} \tag{1.5}$$

here θ may be seen as the average asperity contact time because it increases linearly with time at $v = 0$.

If θ does not depend on time, i.e. for sliding at *steady state*, we get the equations:

$$\frac{d\theta}{dt} = 0 \quad \longrightarrow \quad \theta_{ss} = \frac{d_c}{v}$$

and therefore

$$\tau_f^{ss}(v) = \sigma\left[\mu' + (a-b)\, ln(v)\right]$$

where

$$\mu' = \mu - (a-b)\, ln(v_*)$$

For $a > b$ friction evolves to a higher value for increasing velocities, and vice versa. We refer to the $a > b$ condition as *velocity strenghtening* and to $a < b$ as *velocity weakening*. The former case can only undergo aseismic sliding, which means that portion of faults described by this law are stable and do not spontaneously rupture. In the velocity-weakening situation, sliding is unstable under certain circumnstances and can lead to stick slip when the equivalent stiffness k (equation 1.3) of the fault is lower than a critical value k_c (Rice and Ruina, 1983). The critical value can be found balancing the equation of motion of the spring-slider system:

$$k_c = \frac{(b-a)\sigma}{d_c}$$

Marone et al. (1991) showed that afterslip represented through a spring-slider system may be described by an approximated rate-state friction law. Such approximation takes $b = 0$ (i.e. steady-state equation), and it holds under certain conditions generally valid except in transition areas from velocity weakening to strenghtening (see appendix of Johnson and Burgmann (2006) for more details).

We will derive now the time evolution of the afterslip $\delta(t)$ following the Perfettini and Avouac (2004) formulation. The equation of motion of a spring-slider system is

$$\tau_f(v) = \tau_i + k(v_0 t - \delta) + \Delta\tau(t) \tag{1.6}$$

where τ_i is the initial shear stress, kv_0t is the interseismic shear stressing, δ is the block's slip and $\Delta\tau$ the shear stress perturbation which acts for $t > 0$. Remarkably, for stress perturbations involving both normal and shear stress $\Delta\tau$ is replaced by Coulomb stress change ΔCFF.

Using now the steady state frictional approximation

$$\tau_f(v) = \sigma\mu + a\sigma\, ln\left(\frac{v}{v_*}\right)$$

Hence balancing the equation of motion:

$$\sigma\mu + a\sigma\, ln\left(\frac{v}{v_*}\right) \quad = \quad \tau_i + k(v_0 t - \delta) + \Delta\tau(t) \tag{1.7}$$

Given the initial stress balance (for $t = 0$ and $v(t = 0) = v_i$)

$$\sigma\mu + a\sigma ln\left(\frac{v_i}{v_*}\right) = \tau_i - k\delta_i$$

and subtracting it from equation 1.7

$$\Rightarrow a\sigma\, ln\left(\frac{v}{v_i}\right) = k(v_0 t - \delta + \delta_i) + \Delta\tau(t)$$

Introducing the slip increment $U = \delta - \delta_i$, and noticing that $v = \dfrac{d\delta}{dt} \simeq \dfrac{dU}{dt}$

$$\frac{dU}{dt} = v_i\, exp\Big\{c(v_0 t - U) + \frac{\Delta\tau}{a\sigma}\Big\}$$

where $c = \frac{k}{a\sigma}$. Introducing a characteristic time $t_r = \frac{a\sigma}{kv_0}$ and integrating we get to

$$\delta(t) = \delta_i + \frac{1}{c} ln\left(1 + cv_i F(t)\right) \tag{1.8}$$

where

$$F(t) = \int_0^t exp\Big\{\frac{t'}{t_r} + \frac{\Delta\tau}{a\sigma}\Big\} dt'$$

And a slip velocity

$$v(t) = v_i \frac{exp\Big\{\frac{t}{t_r} + \frac{\Delta\tau}{a\sigma}\Big\}}{1 + cv_i F(t)} \tag{1.9}$$

Let us now consider the coseismic perturbation brought by an earthquake $\Delta\tau(t) = \Delta\tau H(t)$, where $H(t)$ is the step function. Carrying out the calculations we get to:

$$\delta(t) = \delta_i + \frac{1}{c} ln\left(1 + d\frac{v_i}{v_0}\left(e^{\frac{t}{t_r}} - 1\right)\right) \tag{1.10}$$

$$v(t) = v_i d \frac{e^{\frac{t}{t_r}}}{1 + d\frac{v_i}{v_0}\left(e^{\frac{t}{t_r}} - 1\right)} \tag{1.11}$$

with $d = exp\Big\{\frac{\Delta\tau}{a\sigma}\Big\}$.

We have to notice that $\Delta\tau$ leads to a sudden change in sliding velocity which relaxes and goes back to the interseismic slipping velocity v_0, provided that t is much larger than t_r.

This velocity-strenghtening formulation allows us to describe the deceleration of a spring slider system which leads to the post seismic transient slip. This is in agreement with some observations, while other cases are better described by a power law or exponential function.

Just like for seismic events (equation 1.1), a *post seismic* M_0 can be associated with aseismic slip, evaluating the amount of post seismic slip and the area of regions involved in slipping. The post seismic M_0 is an assessment of the aseismic slip of the faults.

Chapter 2

Amatrice - Visso - Norcia seismic sequence

We refer to the *Amatrice-Visso-Norcia* sequence as to the seismic sequence, starting on 24^{th} of August 2016 at 01:36 UTC when a $M_w = 6$ earthquake occurred nearby the town of Amatrice. This event was followed by other two mainshocks, on the 26^{th} of October at 19:18 UTC (Visso earthquake) and the 30^{th} of October at 06:40 UTC (Norcia earthquake), both of them striking with a $M_w \geq 5.9$ (table 2.1). Beside the distruction of many towns in the area, the seismic sequence of Central Italy resulted in hundreds of fatalities.

In continental regions, as the one taken into account, faults have a typical length comparable to the crust thickness ($\sim 10 - 25$ km) (Walters et al., 2018), therefore the earthquakes produced show a maximum $M_w \sim 6-7$ (Pacheco et al., 1992; Triep and Sykes, 1997). As the Amatrice-Visso-Norcia sequence was characterized by several $M_w \sim 6$ earthquakes, it is reasonable to assume the activation of more than one fault: this fact is in agreement with the spatio-temporal clustering observed, with different events occurring in the very same region within a much shorter period of time than the usual recurrence interval (Walters et al., 2018). More specifically, the Amatrice earthquake was followed by the event of 26^{th} of October originating between the towns of Visso and Ussica, about 25 km NW. The third event nucleated four days later nearby Norcia, in between the previous earthquakes. In table 2.1 the seismic sequence features are summarized (data from INGV catalogue)

Table 2.1

	Date	Longitude (°)	Latitude (°)	Depth (km)	M_w
Amatrice	24/08/2016	13.22	42.71	5	6
Visso	26/10/2016	13.09	42.90	10	5.9
Norcia	30/10/2016	13.11	42.83	10	6.5

In the Appennines area, episodes of extension and compression alternated in time (R. Civico, S. Pucci, F. Villani, L. Pizzimenti, P. M. De Martini, R.Nappi and the Open EMERGEO Working Group (2018) Surface ruptures following the 30 October 2016 Mw 6.5 Norcia earthquake, central Italy), at first during the Tethys evolution (i.e. the one responsible for the Mediterranean evolution), and then during the Appennienes chain building phase. As a result, a complex and irregular fault geometry originated.

Structures deriving from large-scale extension phase during the Tethys ocean formation are not well constrained. A second set of extensional faults has been associated with the Miocene bending of the Adria paleo margin foreland domain (about 23 to 5 million of years ago). The Appennines compression, which led to the mountains chain building, brought former extensional areas to be in compression and viceversa. This alternation enhances the faults complexity and segmentation that we observe today. Nowadays, the sector of the Appennines struck by the studied seismic sequence accomodates a $\sim 3-4$ mm/yr extension rate along a NE-SW axis (D'Agostino et al., 2014; Devoti et al., 2017). Extension is accommodated by a complex array of NW-SE and NNW-SSE striking, mainly SW dipping, active normal fault system, and due to former compressive phases these structures are often segmented. The main active tectonic structures in the study area are the Mount Vettore – Mount Bove, the Laga mountains (also known as Gorzano fault), the Norcia and Montereale fault system (figure 2.1). The EMERGEO working group (Civico et al., 2018) provided a map of surface ruptures occurred during the seismic sequence. Indeed, after the 24^{th} of August shock, coseismic surface ruptures were observed along the southern portion of Mount Vettore and Bove fault system as a result of primary surface faulting (Livio et al., 2016; Aringoli et al., 2016; Pucci et al.,2017), while less clear coseismic features were recorded along the Laga Mountains. In the very same area ground ruptures were observed after Visso earthquake even though they were sparse and discontinuos. Both events showed a $\sim N150°E$ strike, prevalently dip-slip kinematics. Coseismic effects following Norcia earthquake consisted of both primary surface ruptures and effects related to ground shaking and permanent deformation (for instance landslides, hydrological variations and liquefaction; EMERGEO working group (2018)). Primary ruptures overlapped with the 24^{th} of August and 26^{th} of October ground fractures, exhibiting a prevalently normal dip-slip kinematics. Contestually, ruptures were also observed on antithetic NE dipping faults.

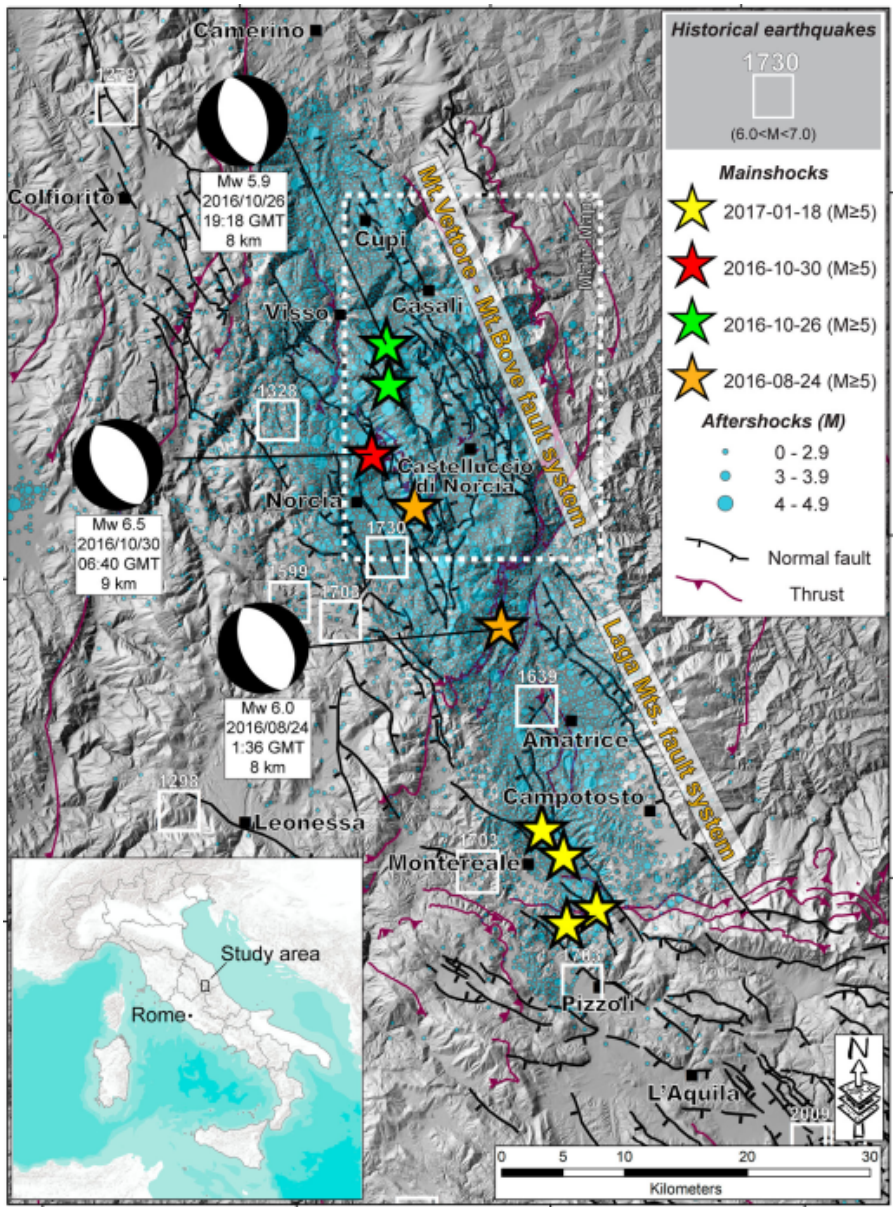

Figure 2.1. The central Italy seismic sequence for the time period 24 August 2016 to 23 January 2017. Stars indicate the mainshocks of the sequence (for whom the focal mechanism is provided). The white-dashed box encloses the study area. Figure from R. Civico, S. Pucci, F. Villani, L. Pizzimenti, P. M. De Martini, R. Nappi and the Open EMERGEO Working Group (2018) Surface ruptures following the 30 October 2016 Mw 6.5 Norcia earthquake, central Italy, Journal of Maps.

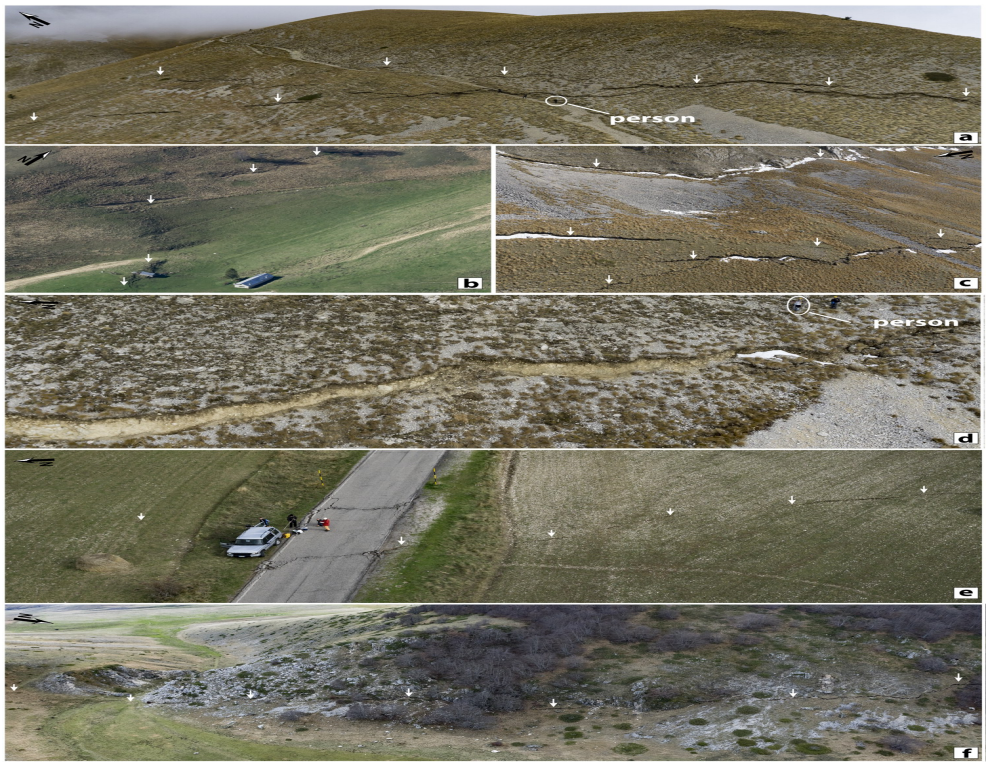

Figure 2.2. Coseismic ruptures along the mount Vettore and Bove fault system. Arrows depict the trace of surface fractures. (a) View of the continuous and stepping splay of the coseismic ruptures along the western Mt. Vettoretto flank; (b) antithetic coseismic rupture in the middle sector of the Vettore Bove fault system; (c) set of parallel coseismic ruptures along the western Mt. Vettore flank; (d) Cordone del Vettore ruptured splay; (e) coseismic ruptures along the Piano Grande di Castelluccio fault splay and (f) antithetic coseismic free-face following a cumulative fault scarp in both bedrock and alluvium (from Civico et al., 2018)

All the main events nucleated at the base of a SW dipping normal fault system segmented by the presence of crosscutting compressional structures, late Miocene in age (Chiaraluce et al., 2017). The presence of these inherited faults, separating diverse geological domains, appears to modulate the evolution of the sequence interfering with coseismic slip distribution and fault segments interaction (Chiaraluce et al., 2017; Lavecchia et al.,2016). Indeed the seismicity pattern occurred throughout the 2016-2017 sequence stresses a common feature among the Appenninic extensional system, which is the strong interaction between the ancient compressional thrusts and the more recent active normal faults.

2.1 Co-seismic models

In the next sections we will go through three different co-seismic solutions. These solutions, which are presented in chronological order, are based on different datasets as new data become available with time. They were also retrieved through different means, including geodetic measurements, geological constrains, seismicity distribution and so on. In the last section of this chapter we will shortly compare the presented solutions, stressing similarities and differences among them.

2.1.1 Early Geometry

An early study of the 2016 Central Italy sequence was conducted by Chiaraluce et al. (2016). Accordingly, the Amatrice-Visso-Norcia sequence activated a 60 km long normal fault system with a principal plane striking N$(150 \pm 10)^\circ$ E (the "principal structure"), made of a set of principal $(50 \pm 5)^\circ$ SW dipping fault segments breaking through the whole upper crust from about $6 - 8$ km depth. Moreover, this principal plane results connected, at shallower depths, with both synthetic and antithetic structures located on the footwall and hanging wall of the mentioned principal structure.

The geometry proposed has been retrieved analyzing the spatial distribution of a subset of aftershocks (more than 25000 in number) with a $M_w \in [0.1, 6.5]$ occurred in the 24^{th} August - 29^{th} November period of time. Such events were relocated inverting P,S waves arrival times, recorded by INGV to retrieve a slip distribution on the considered structures. Note that no station installed after the first main shock was included in the dataset used.

Starting off from the southern portion of Mount Vettore-Bove structure, seismicity suggests the reactivation of the low-dip Campotosto fault segment located about 10 km south from Amatrice (fault activated during the 2009 L'Aquila earthquake, Gualandi, 2014). Moving northward, aftershocks clustered almost horizontally suggesting the presence of an almost flat structure located between 8 and 10 km of depth. The geometry of this hypothetical structure is likely to be slightly east dipping. The Amatrice event was characterized by a bilateral rupture (Chiaraluce et al., 2016): a southernmost patch would be located 4 km up-dip from the hypocenter (at 8 km depth)(figure 2.3), while a northern patch would be located just below Mount Vettore. Data support the idea of a single event, the gap in slip has been associated with the Olevano-Antrodoco-Sibillini (OAS) tectonic alignment crosscutting the normal fault plane and representing a strong lateral heterogeneity for the rupture propagation. Going northward, beyond the OAS, the structure becomes more complex but the main southwest-dipping plane at about 50° becomes clearer on the basis of seismicity distribution. Here, aftershock recordings, reveal the presence of an antithetic fault right in the northern patches area. Besides that, the flat deep structure

seems to be still present and located below this portion of the system (it reaches 12 km depth). Keeping on moving northward we find the part of the structure responsible for the Norcia earthquake. The seismicity distribution shows that this event nucleated at 8 km depth at the base of the 55° SW dipping fault plane and again at the intersection with the deeper structure, here dipping more clearly eastward at about 20°. This main structure branches upward with both synthetic and antithetic faults (respectively on its hanging wall and footwall). Furthermore shallow seismicity suggests the activation of the north–south-trending OAS thrust front. Visso earthquake involved the northernmost part of the "principal structure", reaching the southern termination of the 1997 Colfiorito system, being subparallel to the so-called Sellano segment (Chiaraluce et al., 2003). The almost flat structure seems to be still present (even below the Colfiorito fault), even though less active.

The slip distribution retrieved by Chiaraluce et al. (2016) shows the following features (figure 2.3)

- *Amatrice earthquake* (fault plane striking $N155°E$ and SW dipping at 49°). As it has already been stated, the event was characterized by a bilateral rupture, which propagated at high speed, and a slip distribution occurring mainly on 2 patches, the southernmost patch with maximum slip ~ 1 m; the northern patch characterized by a bigger area and a ~ 0.6 m mean slip.
- *Visso earthquake* (fault plane striking $N159°E$ and SW dipping at 47°) seems to be a double event with a 0.8 s time separation and hypocenters located ~ 4 km apart. Owing to the short time separating the ruptures, the second location is less costrained. The first event began in the southernmost hypocenter and propagated down-dip; the second event ruptured unilaterally NWwards. Slip (~ 1.1 m) results distributed on an elongated patch 8×4 km^2 reaching its maximum at depths of $3.5 - 6.5$ km. The mean rake on the slipping area is $\sim -75°$.
- *Norcia earthquake* (fault plane striking $N151°E$ and SW dipping at 55°) appears to be characterized by slip occurring mainly on a single patch, ~ 5 km up-dip from hypocentral location, of 10×6 km^2 area. This patch results in an avarage 1.3 m slip but it reaches peaks of 2.6 m. The solution proposed puts large amount of slip on the nothern part of the fault, in the shallower portion, thus suggesting that rupture reached the surface (in agreement with coseismic offsets recorded). The patch shows a $\sim -95°$ rake. Noteworthy, the solution shows a secondary slipping area located 16 km southeast of the hypocenter, although this patch is less stable (it is required by southern station recordings).

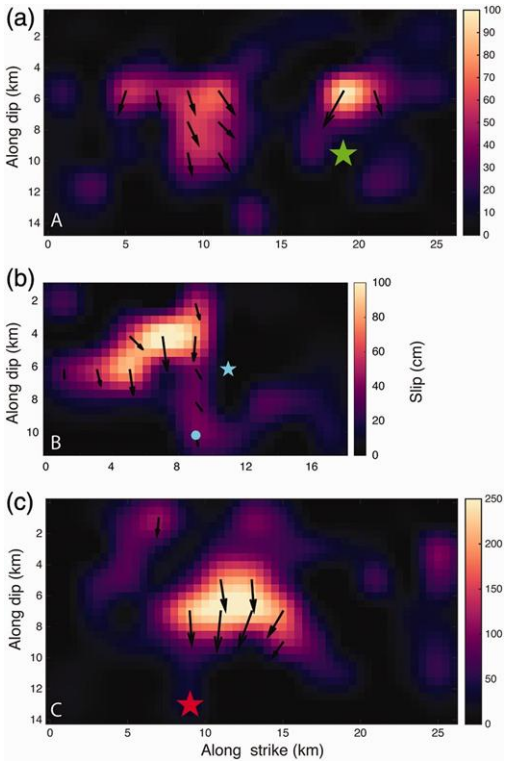

Figure 2.3. Map of slip distribution for the 3 main events of 2016-2017 sequence. Black arrows show slip direction. Stars show the event location, in panel (b) the circle locates the second event. Figure has been obtained by inverting strong-motion data (from Chiaraluce et al., 2017)

2.1.2 MGVB Geometry

A second geometry of the activated faults we are taking into account in this thesis was proposed by Cheloni et al. (2017). It is based on InSAR data acquired by different satellites during the seismic sequence, and also on data acquired by several GPS stations, both in continuum and survey acquisition mode. Compared to previous studies, Cheloni et al. (2017) enhanced the GPS dataset and made use of data retrieved from InSAR, which had not been done previously.

According to the proposed solution, the sequence is associated with the failure of four main asperities belonging to the SW dipping normal fault system of Monte Gorzano, Monte Vettore, Monte Bove ("MVGB system"). Alongside these, in order to better describe Norcia earthquake (i.e. to explain the complex deformation pattern recorded), secondary faults were introduced pointing towards NE e/o WNW with respect to the principal system hanging wall (figure 2.5 and 2.6).

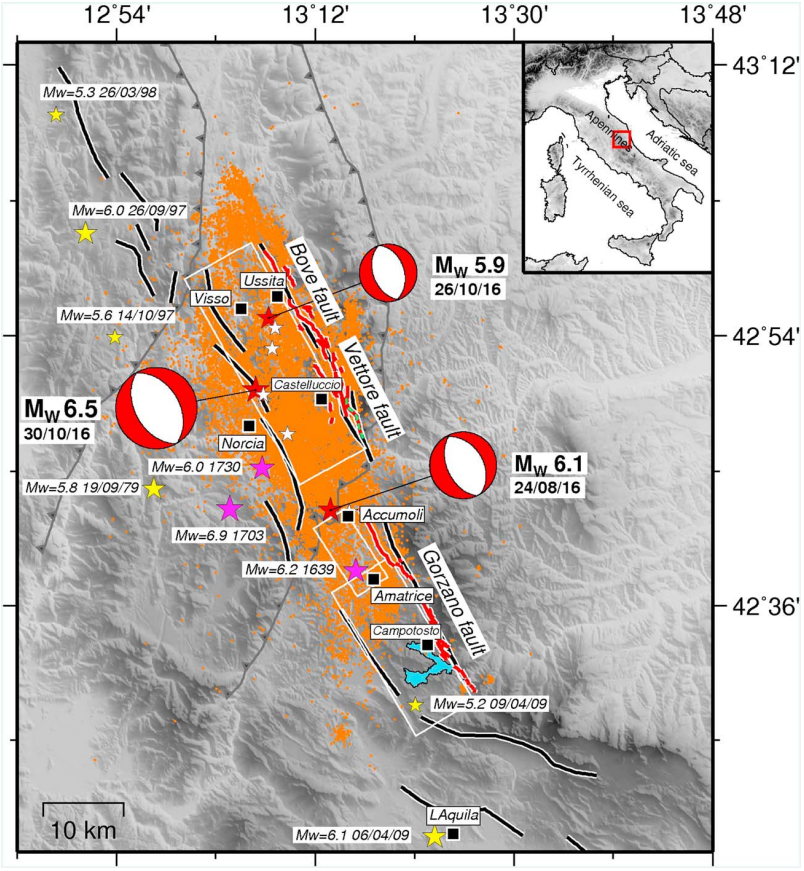

Figure 2.4. Seismotectonic framework of the study area. Solid black lines are surface expression of the major active faults of the area, while the red ones represent the MGVB fault system, with the associated seismogenic sources (white boxes). (from Cheloni et al.,2017)

More in detail:

1. The first event, Amatrice 24^{th} August $M_w = 6.1$, ruptured two different segments of this system: the northern part of Mount Gorzano fault with a $\sim 50°$ SW dipping and a maximum slip ~ 1.4 m (this fault had already been partly activated by the 2009 L'Aquila earthquake); the southern part of Mount Vettore fault with $\sim 40°$ SW dipping and a maximum slip ~ 1.0 m (figure 2.5).

   It has to be stressed that the Amatrice earthquake is deemed to be characterized by the failure of these two segments quoted above, merging in a single structure located at hypocentral depth (Lavecchia et al., 2016; Tinti et al., 2016).

2. The second event, Visso 26^{th} October $M_w = 5.9$, ruptured a ~ 15 km long segment of the system, corresponding to the Mount Bove fault. Results provide a $\sim 40°$ SW dipping fault and the failure of a single asperity, with a fracture directed northwards and a maximum slip ~ 0.8 m (figure 2.5).

3. The third event, Norcia 30^{th} October $M_w = 6.5$, ruptured a ~ 20 km long portion of the main system, striking a part of Mount Vettore fault which had previously remained unbroken. The main asperity failure resulted in a > 2 m slip but, in order to explain the recorded signal, Cheloni et al. (2017) allow some slip to occur in the shallower portion of the plane where ruptures were observed (figure 2.4), and in the deeper southeastern part of the fault, below the main coseismic asperity of the 24 August event (which ruptured only a portion of the Mount Vettore Fault) with a maximum slip ~ 1 m (figure 2.5).

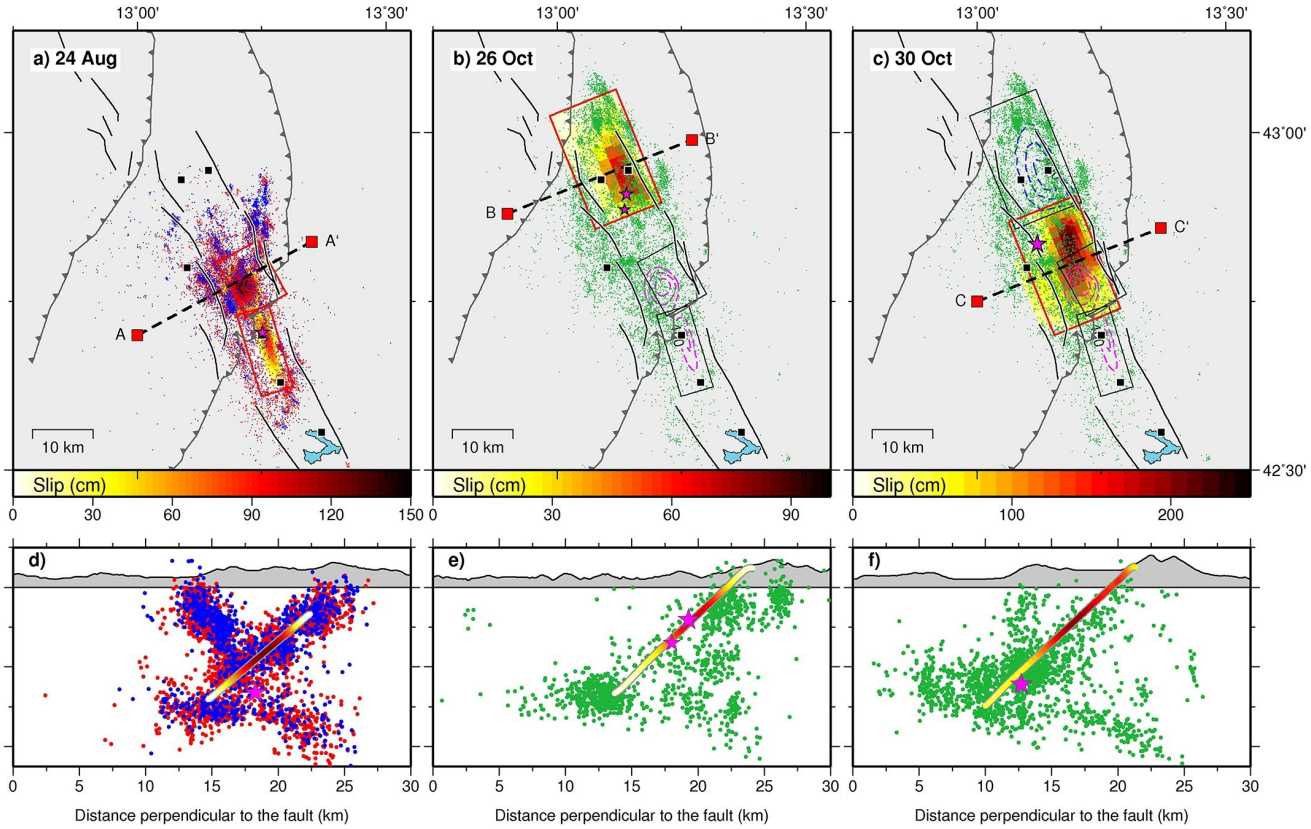

Figure 2.5. The inferred geodetic model of slip distribution on main faults for each event. Red boxes represent the activated faults for the specific event, whereas grey boxes the faults activated during the seismic sequence up to that date. Dashed lines show the coseismic slip distribution up to that moment. Figures d), e) and f) representing the projection along AA', BB' and CC' direction, dots show the seismicity and stars the epicenters. (from Cheloni et al.,2017)

As it has already been stated, in order to better explain the displacement field observed, it is necessary to introduce some secondary faults (figure 2.6), both antithetic

and low-angle compressive structures, in agreement with the usual tectonic environment of Central Appennines (see the beginning of this chapter for geolocigal framework). The antithetic fault appears to be a NE normal dipping fault located in the Norcia area; the compressive structure is a preexisting low-angle WNW dipping thrust segment below the Castelluccio plain partly linked to the Sibillini Thrust. Both the hypotesized solutions show a main patch of slip located between 2 and 4 km depth, with maximum slip of $\sim 0.7 - 0.8$ m. These additional structures are deemed to have slipped aseismically since no large aftershocks occurred around the two hypothesized ancillary faults.

In principle, according to available data, neither the anthitetic nor the ancillary fault can be ruled out (Cheloni et al., 2017).

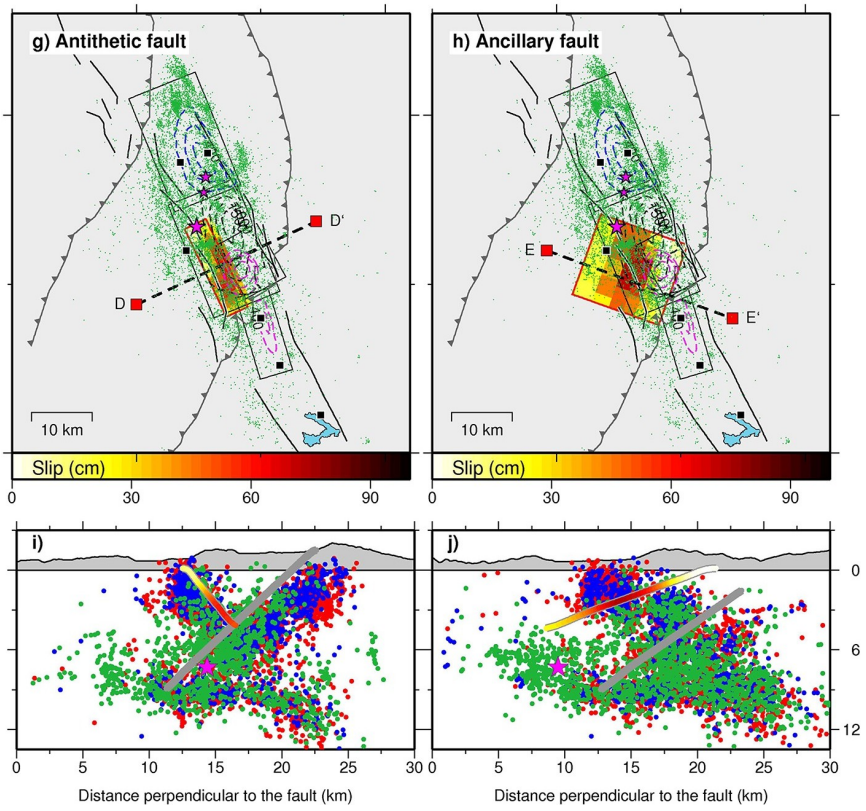

Figure 2.6. The inferred geodetic model of slip distribution on secondary faults for the 30^{th} October event. Graphic symbols used are the same as previous image. Figure g) stands for the antithetic fault case, whereas figures h) stands for the low angle compressional preexisting structure. Figures i) and j) representing respectively g),h) projection along DD' and EE' direction. (from Cheloni et al.,2017)

Cheloni's solution has been reviewed in 2019 after a new data collection, which included: new field observations, new near-field survey mode GPS measurements (both global and regional), new static displacements derived from strong-motion stations.

Although rupture is complicated, Cheloni et al. (2019) suggested that it is not necessary to support a complex fault system by invoking the activation of oblique structures to explain the seismic sequence (as in Scognamiglio et al., 2018; Walters et al., 2018). In fact, the activation of a half-graben normal fault system that simultaneously ruptured both the master MVB normal fault and a number of syntethic and antithetic faults can explain the complexity of fractures observed (Cheloni et al., 2019).

According to this new solution (figure 2.7 and 2.8), the best fault model consists of a main fault plane striking $N159°$ and dipping $38°SW$ in agreement with geometries proposed in Cheloni et al. (2017), Xu et al. (2017) and Walters et al. (2018). Such plane fits the data and its trace matches surface ruptures mapped along the MVB fault system. However to improve the fitting of geodetic data two more antithetic faults have to be taken into account. The major one is a blind splay highlighted by the aftershock distribution. Adding this plane fully explains the displacement observed in the Norcia area (Cheloni et al., 2019). The introduction of a third (minor) steep antithetic fault ($65°NE$ dipping) further reduces the RMS of geodetic data and allows to explain the displacement in the Castelluccio plain.

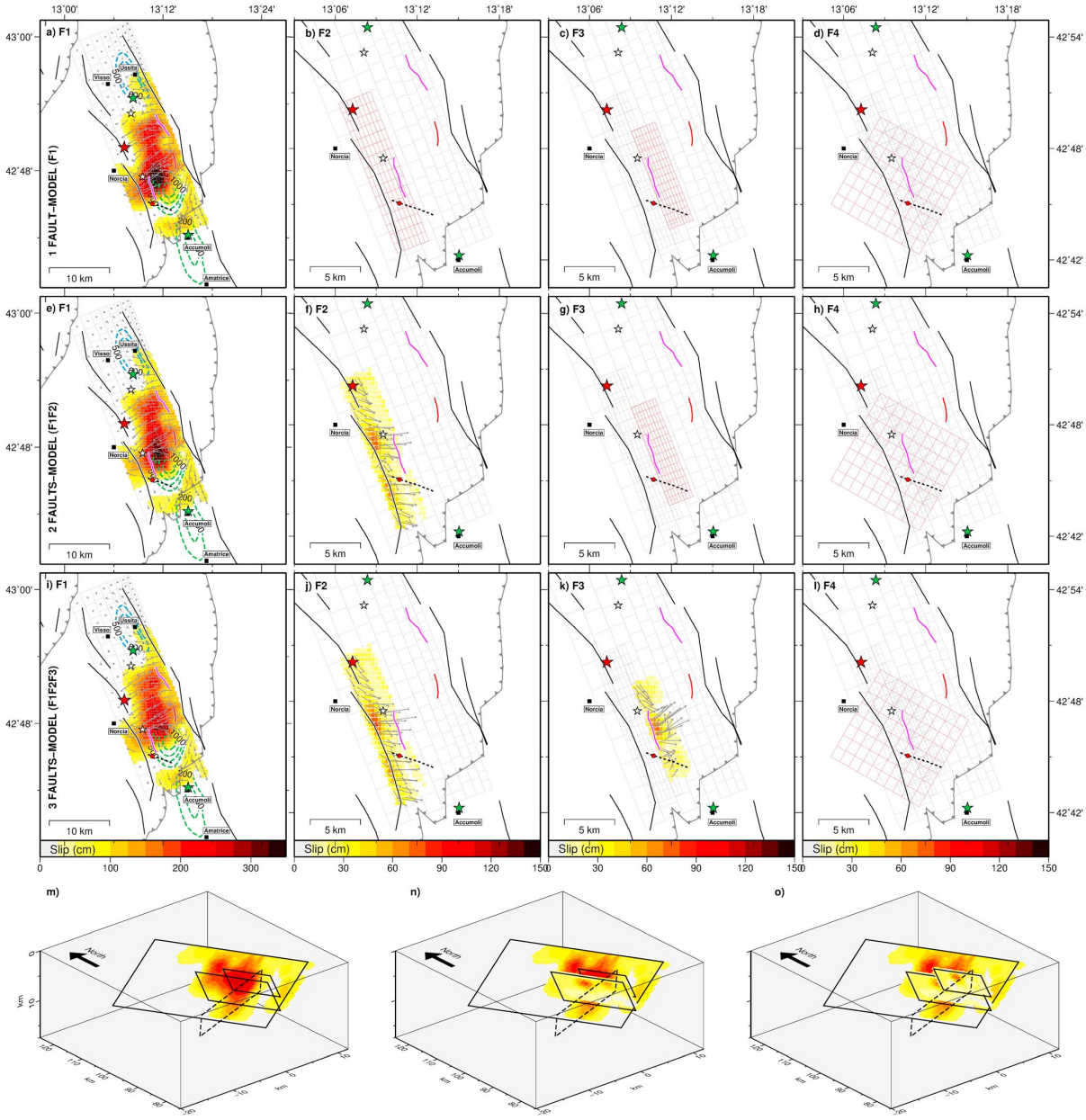

Figure 2.7. Coseismic slip model for Norcia earthquake: panels (a-d) assume slip only on the master fault (F1) and figure (m) shows its oblique view; panels (e-h) assume slip on the master fault and the major antithetic fault (F2) and figure (n) shows their oblique view; panels (i-l) assume the three-faults model described above (F3 is the minor antithetic fault) and figure (o) shows the oblique view. The black dashed fault plane represents an oblique dislocation which has not been included in this model. The green and blue dashed lines show respectively the modeled slip distribution for the Amatrice and Visso earthquake as in Cheloni et al. (2017). (from Cheloni et al.,2019)

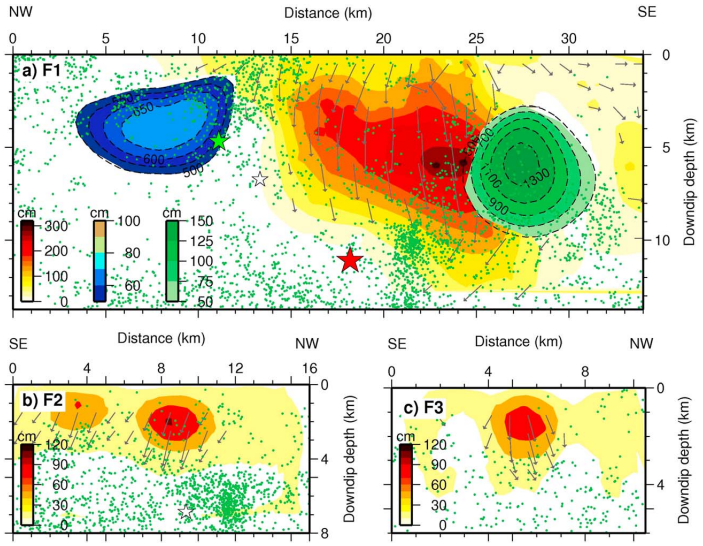

Figure 2.8. Geodetic model for Norcia earthquake: coseismic slip distribution on the F1 (figure a), F2 (figure b) and F3 (figure c). Green dots are relocated aftershocks that occurred within 2 km on each side of the fault plane. The red star locates Norcia mainshock, the green star is Visso event, and the white stars are $M_W > 5.4$ earthquakes. Dashed lines as in figure 2.7. Gray arrows indicate the slip direction. (from Cheloni et al.,2019)

Cheloni et al. (2019) claims that adding more faults does not contribute to a better fitting of data, as their vicinity to the main structure and their small dimensions makes them difficult to detect.

2.1.3 Mount Vettore and Laga fault

The last geometry of faults we are accounting for is the one proposed by *Walters et al., (2018)*. This other model relies on: data retrieved by a regional GNSS dataset for each event, a short-baseline GNSS for Norcia earthquake (which had not been used by Cheloni et al.), a InSAR dataset more extended than those exploited by previous studies. Furthermore, geologic and geophysic costrains were used for the first time, for instance discontinuties and regions of low-coherence of InSAR data were used (which indicate surface faulting) as well as mapping of surface ruptures.

The solution proposed by Walters at al., includes (fig. 2.2):

1. four principal segments (3 for Mount Vettore fault, 1 for Laga fault) which are well represented by the dataset exploited;

2. three secondary faults on Mount Vettore's hanging wall, two synthetic faults and one antithetic fault;

3. Norcia fault, which is antithetic with respect to Mount Vettore. This structure would be 12 km long with a ENE dipping;

4. Pian Piccolo normal fault, which would result in a 14 km long structure.

The faults' situation is summarized in figure and in table:

Table 2.2. Features of Walters et al. (2018) faults geometry.

Fault name	Strike (°)	Dip (°)	Length (km)	Bottom depth (km)
Minor synthetic	158	40	12	2
Vettore (1)	155	40	18	10
Vettore (2)	155	40	8	10
Vettore (3)	165	45	15	10
Laga	163	45	15	10
Minor synthetic	165	40	10	2
Minor antithetic	325	65	6	1
Norcia antithetic	340	65	12	6
Pian Piccolo	222	40	14	8

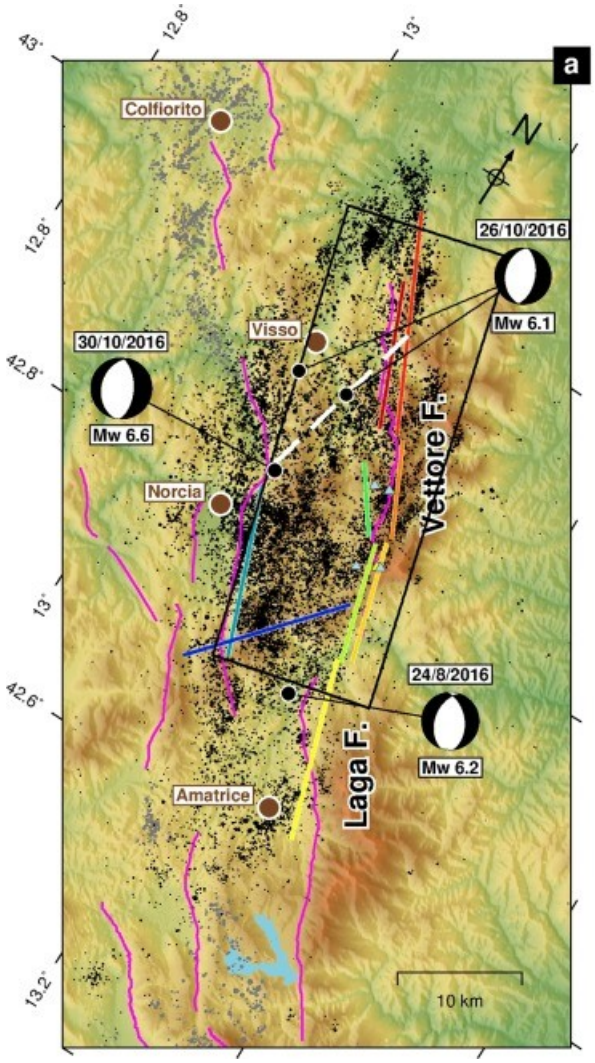

Figure 2.9. The up-dip projection of fault geometry proposed is shown in figure together with the bodywave focal mechanism. Lines in nuance of orange represent the M. Vettore faults whereas lines in nuance of yellow represent the M. Bove faults. Mapping active normal faults are represented by magenta lines (from Walter et al.,2018)

The 3 secondary faults are needed to explain both geodetic displacements and rupture field mapping.

Norcia fault is well highlighted in the aftershock data (Chiaraluce at al., 2017); whereas Pian Piccolo fault is supported by Castelluccio plain geomorphology, by geological mapping (Coltorti e Farabollini 1995) and by the relocalization of aftershocks.

Although the relative position of these two structures is not univocally determined, we shall bear in mind that they do not affect slip distribution on the principal structure represented by the Vettore-Laga system, which is, as it has already been said, well

constrained by data.

On the contrary, secondary faults, introduced in this work for the first time, play an important role to retrieve the slip distribution on Vettore fault after Visso and Norcia earthquakes.

The inversion was carried out dividing each of the nine segments in 1×1 km patches (parallel to strike and depth direction). The inversion method followed Floyd et al. (2016), and displacements result from slip on rectangular dislocations in an elastic half-space (Okada, 1985). The solution for each patch has been found for a $2D$ slip model, leaving rake free to vary. Slip has been forced to be zero in some regions not to fit noise in geodetic data and to prevent high slip in shallow patches where field mapping shows no sign of it.

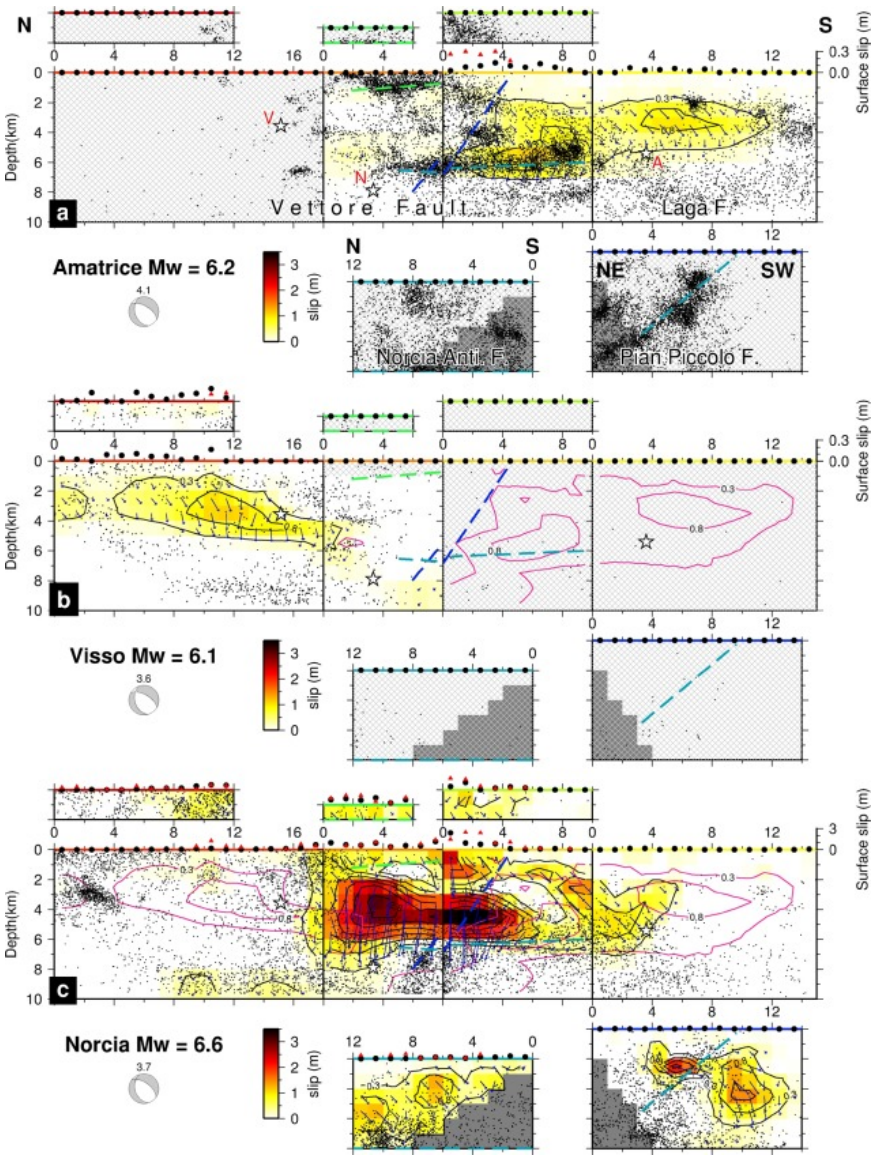

Figure 2.10. Slip distribution models for the Amatrice (a), Visso (b) and Norcia (c) earthquakes. Hypocenters are marked by stars. Different pannels stand for different segments activated. Black contours show slip's magnitude and pink contours show the cumulative slip up to that event. Dashed coloured lines show the intersection of the different model faults. (from Walter et al.,2018)

The geodetic solution represented matches the solution found by a body-waves method (i.e. total moment release, the centroid depth, and the geometry of the SW-dipping nodal plane are comparable), see Walters at al.(2018) for more details. However, the geodetic moment tensors include a slight oblique component (the seismological moment tensors

are almost dip-slip pure). In the following figure we show the solution obtained through seismological means.

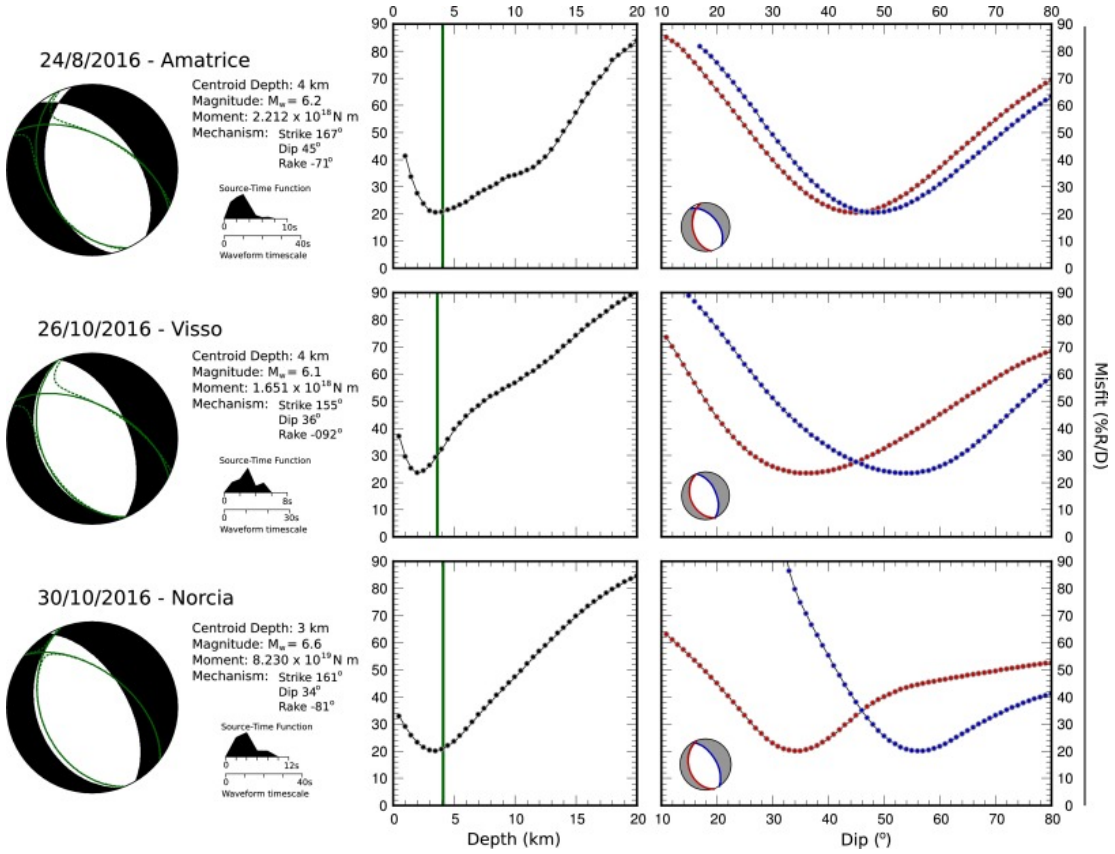

Figure 2.11. Seismological solution. Left column shows the best-fit seismological focal mechanism, the green line represents the geodetic mechanism. Central panels show depth-misfit curves, vertical green line shows the geodetical solution. Right panels show dip-misfit plots. On each, red indicates the SW-dipping plane, blue the NE-dipping plane. (from Walter et al.,2018)

2.2 Comparison of solutions

The retrieved solutions of these different studies show both some common features and differences. All of the solutions imply the activation of a system which fills the gap between the Campotosto fault (held responsible for L'Aquila 2009 earthquake), and the Colfiorito fault (responsible for Colfiorito sequence 1997). Having said that, the proposed segmentation of this system is slightly different in terms of precise fault location, fault size, fault dip angle, and slip distribution along the ruptured plane. This is mainly due to the complicated pattern of deformation caused by this earthquake. Chiaraluce et al. (2016) and Cheloni et al. (2017) proposed almost the same structure (although Cheloni divided the fault responsible for Amatrice's earthquake into two, namely Vettore and Gorzano faults, while Chiaraluce proposed a single plane). This similarity of geometries produced solutions which are much alike one another. Walters et al. proposed four principal segments which match the previous ones (see figure 4.3) with a comparable amount of slip occurring in the same regions but, in Walters et al. (2018) solution, it is located in the shallower portions of the planes (see figures 2.5, 2.8 and 2.10). As a matter of fact both geodetic and seismological solutions proposed by Walters constrain slip above 6 km depth and this is in contrast with the two previous studies who suggested significant slip deeper than 6 km for Norcia earthquake on Mount Vettore fault.

We should notice that Pian Piccolo and Norcia fault resemble the two additional secondary faults introduced by Cheloni at al. In particular, the former shares some common features with the fault associated with a reactivation of Sibillini Thrust proposed by Cheloni et al. (2017), although few differences in structure arise (Pian Piccolo fault has a steeper dip and projects to the surface $\sim$ 2 km further to the N). Nevertheless, both solutions proposed recover the same oblique sense of slip on the faults mentioned.

Eventually a simplier solution for Norcia event was proposed in Cheloni et al. (2019), where the main structures were gathered in a single major fault plain, as data allow the existence of an easier solution.

Clearly, differences in the solutions proposed derive both from the different geometry of principal faults introduced and from different dataset exploited.

Chapter 3

GPS Data analysis

3.1 Introduction

The *Global Positioning System* was originally invented in 1973 by the US government for military purposes. Later on, its use was extended to civilians and to the scientific environment, and enhanced in its accuracy.

GPS exploits time and distances measurements to navigation satellites. GPS is widely used in Earth sciences (Segall et al., 1997), and in particular the Differential Positioning technique is usually adopted to investigate tectonic frameworks and for geodetic purposes. Such technique permits to determine the distance between a certain point and another point of known position (Hager et al., 1991). GPS signals are radio signals broadcasted by two modulated carrier phases and the precision that can be reached through phase measurements is 2-5 mm as described in Dixon et al (1991).

In this study, GPS data were used to detect the displacement related to post seismic slip. In the following sections we will introduce the network employed in this study, we will go through the three-steps process that leads to the time series analysis and we will describe how these GPS time series have been treated. The *Independent Component Analysis* technique will be described in the second part of this chapter.

3.2 Central Italy GPS network

A GPS network can, in principle, consist of both stations acquiring data continuously (i.e. "continuous stations" or "cGPS") and stations acquiring data sporadically ("epoch stations" or "eGPS"). cGPS stations provide position once a day with high accuracy (up to a few millimiters) giving temporal continuity to the dataset. To supply for the lack in spatial coverage, a cGPS network can be temporally enhanced deploying eGPS stations. cGPS and eGPS stations have structural differences, i.e. their "monumentation" is different, and therefore provide data with different precision and can be weighted differently in the

analysis step. GPS data are processed to estimate the stations' position once a day and can be exploited to investigate a wide range of tectonic processes.

Figure 3.1. The cGPS station "ARQT", from RING network

The study area is populated by various GPS networks. Among these, we find the permanent GPS stations used for topographic and civil purposes, the "Rete Integrata Nationale GPS" (RING) and the Central Appennines Geodetic Network (CaGeoNet) both managed by the Istituto Nazionale Geofisica e Vulcanologia (INGV) for scientific purposes (see Appendices for the complete list).

In order to better investigate the post seismic signal some stations were installed after the 24^{th} of August main shock both in the near and far field.

In this study 139 stations were used. Coseismic displacements can be significantly biased by the presence of a fast initial post-seismic transient. This is particularly critical for those GPS stations missing data for some time interval after the mainshock (i.e. eGPS stations reoccupied later after the mainshock). Thus, of the whole discontinuos network available in the area, only one eGPS station could provide reliable information.

Positions and names of stations used are reported in the next figures:

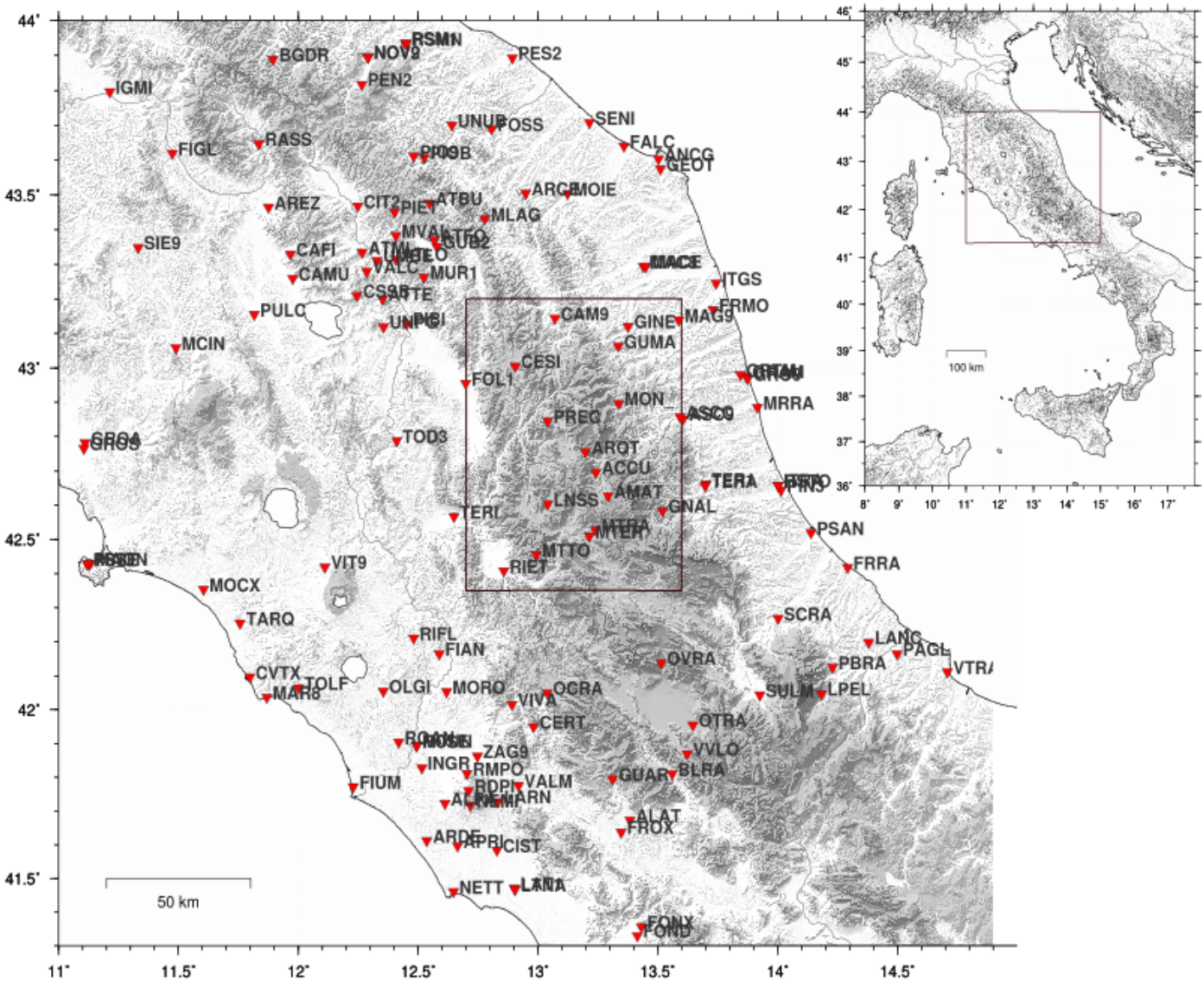

Figure 3.2. Figure shows the complete GPS network employed in this thesis. The rectangle embeds the study area.

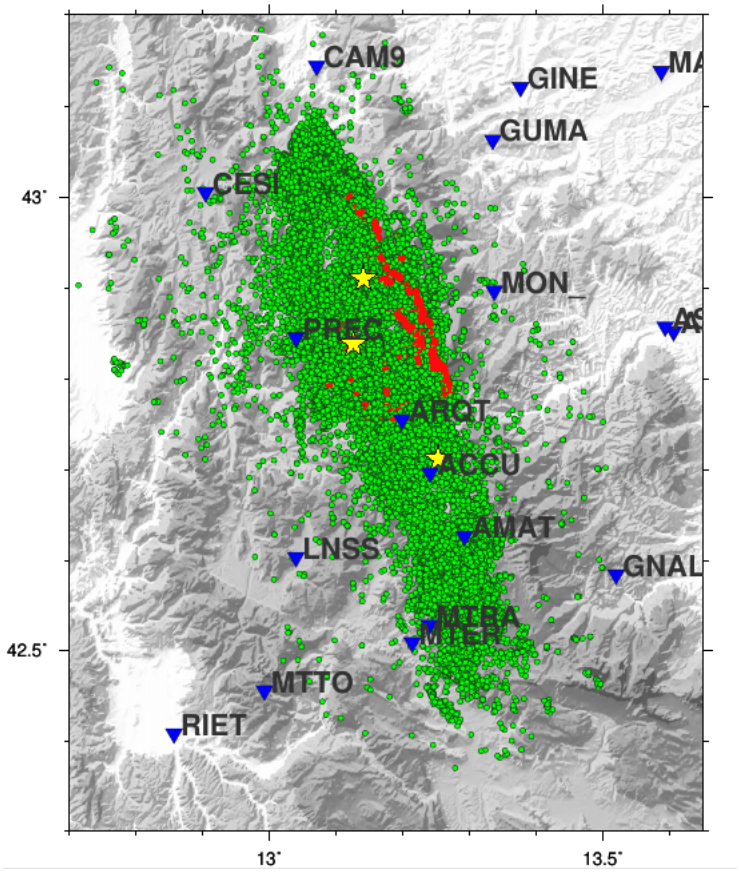

Figure 3.3. Zoom of the study area. Triangles show GPS stations position; yellow stars represent the epicenters; red traces show the location of the mapped coseismic surface ruptures; green dots show the complete aftershock distribution recorded after the Amatrice earthquake.

3.3 Data analysis

GPS data go through a three-step process which (1) reduces raw phase data, (2) combines loosely constrained solution and defines the reference frame, and (3) analyses time series (Serpelloni et al., 2006, 2010).

In the first step GPS phase observations are used to estimate site position as well as to adjust satellite orbital parameters and tropospheric delay parameters through the GAMIT (V10.4) software (Herring et al., 2010). Ocean loading and pole-tide correction model FES2004 is applied, and the Global Mapping Function is used to determine the tropospheric delay model and the global pressure and temperature model (see Boehm et al., 2006 for more details). The loosely constrained solution obtained is consistent with the orbital solution from the Scripps Orbit and Permanent Array Center (SOPAC), it is

stored and contributes to the INGV combined solution.

In the second step the loosely constrained solutions are combined with the solution provided by the IGS network made available by MIT (Serpelloni et al., 2018) through the ST-FILTER program of QOCA software (Dong et al.,2002), contextually a global reference frame is realized applying generalized constraints (Dong et al., 1998).

In the last step the secular trend (i.e. the velocity of sites with respect to Eurasian plate motion) and the tectonic and non-tectonic offsets (such as changes in antennas) are removed from time series. Such analysis has been done using the TSfit Matlab code through the "lsqcurve" function. Such function performs a nonlinear curve-fitting solving problems in a least-squares sense. Each component of the recorded position of a station at time t has been parametrized through the function

$$x(t) = x_0 + v_0 t + C_2 cos(2\pi\Delta t) + S_2 sen(2\pi\Delta t) + C_4 cos(4\pi\Delta t) + S_4 sen(4\pi\Delta t) +$$

$$+ \sum_{j}^{N_{off}} O_j H(t - t_j^{off}) + \sum_{j}^{N_{eq}} \left(A_j + B_j f(t - t_j^{eq}) \right) H(t - t_j^{eq})$$

as in Mavrommatis et al. (2014).

This function embeds the contribution of a linear motion (first two terms), annual and multiannual periodic terms, N_{off} step functions which account for non-tectonic offsets that stations recorded, N_{eq} tectonic offsets ($A_j H(t - t_j^{eq})$) and post seismic transients.

The post seismic term is usually parametrized as a logarithmic or exponential function:

$$f(t - t_j^{eq}) = \begin{cases} \left(1 - e^{-\frac{t - t_{eq}}{\tau_j}}\right) \\ ln\left(1 + \frac{t - t_{eq}}{\tau_j}\right) \end{cases}$$

Boundaries on the offsets amplitude (A_j and O_j) have been imposed through an estimation of both tectonic and non-tectonic jumps; boundaries of ± 1 cm have been imposed to x_0 and on the characteristic time ($\tau \in [0; 2.5]$ yr). In order to constrain v_0, a velocity field has been constructed using those stations with time series longer than 5 yrs. Through an interpolation, a velocity has been associated with discontinuos or short time series (with less than 5 years of recorded data). This resulted in boundaries of $v_0 \in [-3; 3]$ mm/yr along east, $v_0 \in [-1; 5]$ mm/yr along north, and $v_0 \in [-7; 3]$ mm/yr along up direction. Remarkably, boundaries on the velocity have not been imposed to GPS stations with more than 5 years of data (first epoch before 2013). For such stations v_0 is another parameter to be estimated by the fit. Fitting the time series and determining the best

parameters it is possible to remove the secular trend and the offsets by subtracting from the recorded signal the parametrized one.

Once the time series cleaning has been carried out, it is possible to perform an *Independent Component Analysis*: the ICA code cannot deal with offsets and it is not capable of properly separating a linear trend which would cause a cross talk among the ICs. Failing in removing these signals results in a bad extracion of the ICs from the recorded signal (see next sections for more details).

In the following figures a raw time series and a filtered one are shown: it can be seen from the second image that the linear trend and the offsets have been removed.

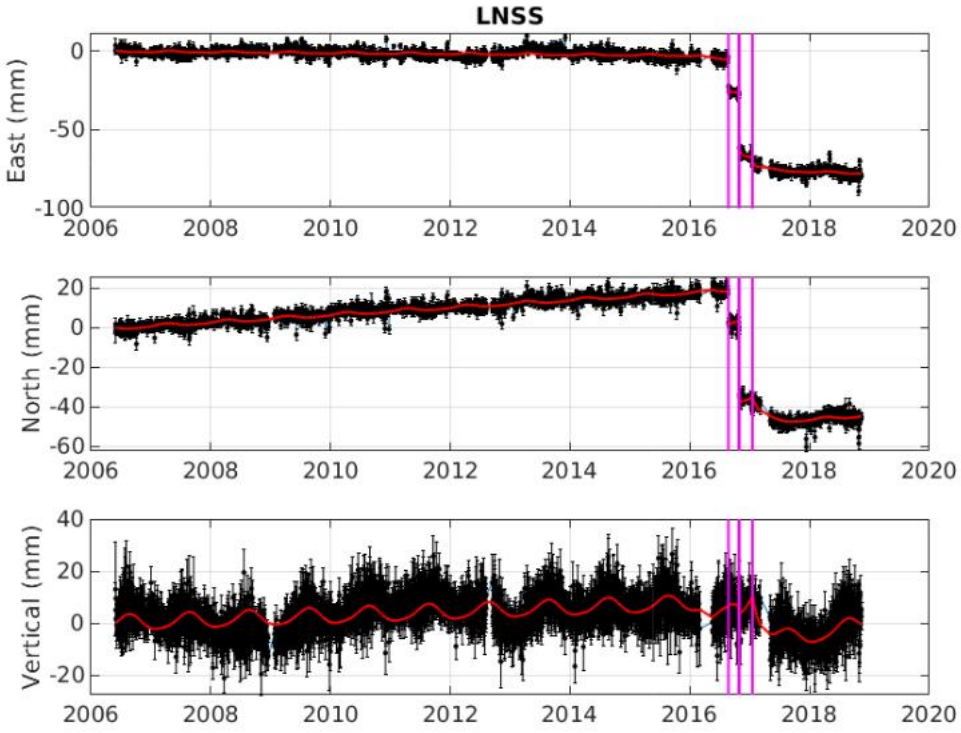

Figure 3.4. Raw time series recorded by LNSS station. Red line shows the fitting function, vertical lines show offsets' epochs.

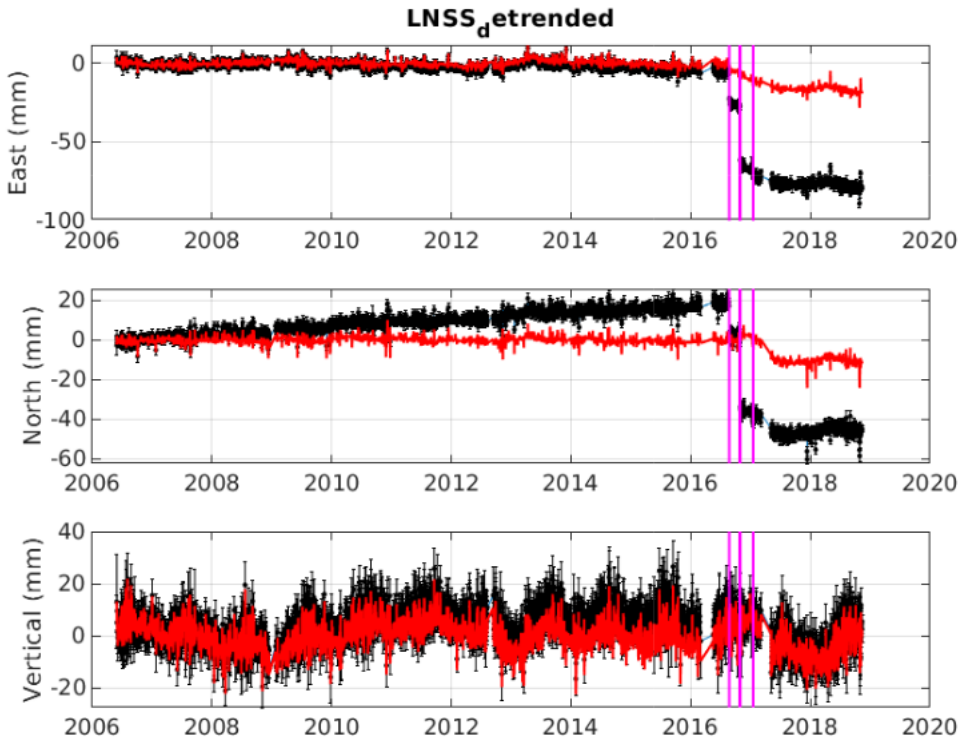

Figure 3.5. LNSS time series after offsets and secular trend removal, red lines show the detrended time series whereas vertical lines show the offsets' epochs. It is evident the correction for the linear trend (central panel), and for the offsets (upper and central panels).

3.4 ICAIM theory - A Blind Source Separation technique application

A Blind Source Separation (BSS) problem's solution holds with recovering and separating those sources that originated the observed dataset. In our case, the data consist of time series of surface displacements recorded through a GPS network (the position of each station at some epochs).

Many different multivariate statistic approaches exist, among which the Principal Component Analysis (*PCA*) is widely used. A PCA allows us to reduce the dimension of data space, keeping most of the variance of our dataset explained. However, as the PCA projects data space into a new Euclidean space (minimizing the misfit with a $\mathbf{L}^2$ norm) imposing uncorrelation, it is not the best approach.

As a matter of fact, when dealing with the separation of geophysical signals, an *Independent Component Analysis* (ICA) is more suitable, as it imposes the independence

of sources instead of their uncorrelation. If, on the one hand, a PCA decomposition is able to reproduce better the original signal, on the other hand an ICA decomposition allows us to better give a physical meaning to the different components. Some approximations are needed to make up for missing data and a *variational Bayesian ICA* (*vbICA*) can be used. The vbICA models the probability density function of each source signal through a mix of Gaussian distributions.

The specific aim of this thesis is to separate those sources that originated the observed dataset: the ICA gives as an output a fixed number of signals that describe the temporal evolution of a deformation source and the associated displacement recorded by the GPS stations. Among these signals we focused on the one representing the post seismic transient which was pointed out and eventually inverted. The final result is the distribution of afterslip occurred on the faults that were activated during the Amatrice - Visso - Norcia sequence by inversion of the so-called ICA-reconstructed effects of postseismic signal on all the recording stations.

In order to do so, we need to set the geometry of faults and to discretize them in subfaults or *patches*. Faults are assumed of rectangular shape, and on each patch slip is assumed of uniform dimension. We furtherly assume that such faults are embedded in an elastic Poissonian medium (Poisson ratio $\nu = 0.25$).

In the next paragraphs we will describe the ICA technique principles. This technique allows us to point out the post- seismic contribution to our total displacement, which is what we need to invert.

3.5 Principles of ICA

Let us consider our network made by N GPS stations recording their positions (east, north, vertical) once a day. Our dataset will therefore consist of $M = 3N$ time series, each one with T-epochs recorded. Let us call $X_{M\times T} = \begin{pmatrix} x_{11} & \dots & x_{1T} \\ x_{M1} & \dots & x_{MT} \end{pmatrix}$ our data matrix. From a multivariate statistical point of view each time series is a sample describing a random variable (rv). Furthermore we will assume that our dataset is produced by $L-$sources ($L < M$) which, combined, produce the observed dataset. On top of this, the sources are deemed to be investigated separately. This means that we are making the following assumptions

- *Low-rank:* the data matrix $\mathbf{X}$ has a low-rank, i.e. most of the data can be represented through a small number of components. This assumption allows us to truncate the decomposition and thus to approximate the original matrix.
- *Independence* of different sources producing our dataset. This allows us to select and isolate the physical sources which we are most interested in.

- *Linearity:* our observations result from a linear combination of the different sources, acting on our system through the Green's functions, which are linear both in time and space.

Let us rewrite our dataset as

$$\mathbf{X}_{M\times T} = \mathbf{A}_{M\times L}\mathbf{S}_{L\times T} + \mathbf{N}_{M\times T} \tag{3.1}$$

where $\mathbf{S}$ is called *source matrix* and embeds the time evolution of the L sources; $\mathbf{A}$ is called *mixing matrix*; $\mathbf{N}$ is the gaussian noise associated with the measurements. What we are willing to do is identifying $\mathbf{S}$ constraining to independence the probability density functions of the L sources. This condition is expressed by the equation:

$$p(s_1, .., s_L) = \prod_i^L p(s_i)$$

with each of the s_i being the time evolution of one source.

To achieve this, the strategy adopted by a vbICA method is based on the creation of a generative model, seeking those parameters that better explain our data. This requires the *Likelihood* function or, in our Bayesian context, the posterior probability density function of parameters, to be maximized. This will be explored more in detail in the next section.

3.6 vbICA

A generative model $\mathbf{M}$ is characterized by observed variables, hidden variables ($\mathbf{H}$), hidden parameters ($\boldsymbol{\theta}$) and the relations among them. Distributions describing the parameters of our model are regulated through further parameters called "hyper-parameters".

Hidden parameters and variables go by the name of weights $\mathbf{W} = \{\mathbf{H}, \boldsymbol{\theta}\}$. A generative model aims to find the best weigths explaining observations and matching the a priori knowledge $p(\mathbf{W}|\mathbf{M})$. From a Bayesian point of view, this means maximizing the posterior probability density function over $\mathbf{W}$, given $\mathbf{X}$

$$p(\mathbf{W}|\mathbf{X}, \mathbf{M}) = \frac{p(\mathbf{X}|\mathbf{W}, \mathbf{M})p(\mathbf{W}|\mathbf{M})}{p(\mathbf{X}|\mathbf{M})}$$

where

$$p(\mathbf{X}|\mathbf{M}) = \int p(\mathbf{X}|\mathbf{W}, \mathbf{M})p(\mathbf{W}|\mathbf{M}) \quad d\mathbf{W}$$

As in most cases $p(\mathbf{X}|\mathbf{M})$ cannot be solved, Choudrey proposed a variational approximation. According to Choudrey, maximizing a quantity called *Negative Free Energy* (NFE) it is possible to find a good approximation of the true $p(\mathbf{W}|\mathbf{X},\mathbf{M})$. The *NFE* is defined as

$$NFE[\mathbf{X}] = \Big\langle ln\Big(p(\mathbf{W}|\mathbf{X})\Big)_{p'(\mathbf{W})}\Big\rangle + H[\mathbf{W}]$$

(dependence on $\mathbf{M}$ is dropped for conciseness)

where $\Big\langle . \Big\rangle$ is the expected value given $p'(\mathbf{W})$ and $H[\mathbf{W}]$ is the entropy of $p'(\mathbf{W})$. We now need to choose a pdf of weights $p'(\mathbf{W})$. This is usually done through a factorization of the form

$$p'(\mathbf{W}) = \prod_{i}^{N} p'(w_i) \tag{3.2}$$

for some partition of $\mathbf{W}$.

Each w_i is a rv, and in the vbICA case the partition $\mathbf{W} = \{\mathbf{A}, \mathbf{S}, \mathbf{\Lambda}, \mathbf{q}, \mathbf{\Theta}\}$ for the weights is generally used: $\mathbf{A}$ is a set of rvs describing the mixing matrix; $\mathbf{S}$ is a set of rvs describing the source matrix; Λ is a set of rvs describing precision (i.e. inverse of variance). Each source s_i is obtained through a mix of Gaussian distributions. The variable $q_i = 1, .., m_i$ tells us which Gaussian component of the $i-th$ source is used to produced the s_i, and $\mathbf{q} = \{q_1, .., q_m\}$. How these Gaussian components are mixed is described by the rvs θ_i.

Remarkably, the constrain $\prod_i p'(w_i)$ automatically satisfies the independence condition (as the M time series are approximately produced by the L sources).

3.7 ICAIM operatively

In this section we will go through the various steps the ICAIM algorithm takes. The first step of a vbICA method is to initialize a trial value for $\mathbf{A}$ and $\mathbf{S}$ (namely $\mathbf{A}_0$ and $\mathbf{S}_0$). This can be done using the results from a PCA in the form of a linear decomposition:

$$\mathbf{X}_{M\times T} = \mathbf{U}_{M\times L}\mathbf{\Sigma}_{L\times L}\mathbf{V}^T_{L\times T} \tag{3.3}$$

then the product $\mathbf{U\Sigma}$ is used as a starting point for $\mathbf{A}$ and $\mathbf{V}$ as a starting point for $\mathbf{S}$. An important step which is taken when performing a PCA decomposition is called

centering, which deals with the fact that the rows of our data matrix $\mathbf{X}$ (i.e. our time series) have arbitrary offsets. Let us give an explainatory example:
given the two data matrix $\boldsymbol{X}_1 = \begin{pmatrix} 0 & 1 & 2 & 3 \\ 0 & 1 & 2 & 3 \end{pmatrix}$ and $\boldsymbol{X}_2 = \begin{pmatrix} 0 & 1 & 2 & 3 \\ 1000 & 1001 & 1002 & 1003 \end{pmatrix}$ it is clear that both matrixes represent the same displacement at 4 epochs with the only difference of a 1000-offset. Nevertheless a 1-component decomposition can fully explain $\mathbf{X}_1$ but cannot explain $\mathbf{X}_2$. Meaning that if different stations have different chunks of missing data at different epochs, non-physical offsets can be introduced . Basically a proper centering translates our time series so that the barycenter of points is located in the origin of axes.

Having the centering step carried out, we now proceed with a linear decomposition with a small number of components, such as a *Singular Value Decomposition* (SVD). The goodness of our decomposition is often assessed by:

$$\chi^2 = \sum_{i,j} \left(\frac{X_{model}(i,j) - X_{data}(i,j)}{\sigma(i,j)} \right)^2$$

with $\sigma(i,j)$ being the variance associated. Alternatively:

$$\chi^2_{red} = \frac{1}{dof} \chi^2$$

where the number of degree of freedom (dof) used to compute the χ^2_{red} is given by

$$dof = N - r \times (m + n - 1) - 2 \times p$$

where N is the total number of data, i.e. the total number of positions recorded by the GPS network; r is the number of ICs used in the decomposition; m is the number of time series; n is the number of epochs and p is the total number of patches of the fault system.

However, as the time series might not be as complete as a SVD would require, two different algorithms were proposed to deal with missing data. The first one was developed by *Srebro and Jaakola* (2003) and it weights missing data as zero; the second one developed by *Bailey* (2012) which is an Expectation-Maximization algorithm (EMPCA). The main difference between these two is that the former does not impose orthogonality of eigenvectors.

Once these steps have been carried out, we have the starting point for $\mathbf{A}$ and $\mathbf{S}$ (respectively $\mathbf{A}_0$ and $\mathbf{S}_0$) and we are able to proceed to maximize the NFE previously introduced. This process eventually leads to our final ICA decomposition

$$\mathbf{X}_{ICA} = \mathbf{A}\ \mathbf{S} = \mathbf{U}_{ICA} \mathbf{\Sigma}_{ICA} \mathbf{V}^T_{ICA} \tag{3.4}$$

exploiting the propriety that a linear decomposition is always possible. Columns of $\mathbf{U}_{ICA}$ and $\mathbf{V}_{ICA}$ are unit norm non-dimensional and non-orthogonal vectors. $\mathbf{U}_{ICA}$ and $\mathbf{V}_{ICA}$ contain respectively spatial and temporal information of the dataset; $\mathbf{\Sigma}_{ICA}$ is a diagonal matrix containing the weights of the ICs.

As it has already been stated, the final step requires the inversion of the chosen ICs embeded in the $\mathbf{U}_{ICA}$. In our case, we have only one IC to invert. Our linear system is:

$$\mathbf{d} = \mathbf{G}\mathbf{m} \tag{3.5}$$

where the data vector $\mathbf{d}$ coincides with first column of matrix $\mathbf{U}_{ICA}$, $\mathbf{G}$ is the Green's function for the fault and $\mathbf{m}$ is the a posteriori IC slip model.

Following *Tarantola* (2005) least square formulation, naming $\mathbf{C}_m$ the covariance matrix associated with $\mathbf{m}$:

$$\mathbf{m} = \mathbf{m}_0 + \mathbf{C}_{m0}\mathbf{G}^T \left(\mathbf{G}\mathbf{C}_{m0}\mathbf{G}^T + \mathbf{C}_D\right)^{-1} (\mathbf{d} - \mathbf{G}\mathbf{m}_0)$$

$$\mathbf{C}_m = \mathbf{C}_{m0} - \mathbf{C}_{m0}\mathbf{G}^T \left(\mathbf{G}\mathbf{C}_{m0}\mathbf{G}^T + \mathbf{C}_D\right) \mathbf{G}\mathbf{C}_{m0}$$

where $\mathbf{m}_0$ is the a priori model (assumed null as in Radiguet et al., 2011), $\mathbf{C}_{m0}$ is its corresponding covariance matrix, $\mathbf{G}$ embeds Green's functions and $\mathbf{d}$ stands for the data vector, $\mathbf{C}_D$ is the covariance matrix of data.

The a priori model covariance matrix used is the one proposed by Radiguet at al. (2006): an exponentially decaying in space correlation is selected, which is used to introduce correlation between nearby parameters (i.e. spatial smoothing). Given two patches A and B at a distance d_{AB}:

$$C_{m0}^{AB} = \left(\sigma_m \frac{\lambda_0}{\lambda}\right)^2 e^{-\frac{d_{AB}}{\lambda}} \tag{3.6}$$

where λ is the characteristic decay length, λ_0 is a scaling length factor fixed to the root mean square of the avarage patch area, σ_m is a standard deviation of the model parameters.

Number of components: The number of components used in our ICA decomposition is fixed a priori. One may wonder which is the most appropriate number of ICs that should be used. The straightforward answer is to compare the NFE resulting from the decompositions carried out with a different number of ICs, checking which one is the largest (i.e. the closest to zero). However the NFE might lead us to add more components than necessary: a higher number of ICs is expected to better reproduce the dataset but not all of the components may be needed to explain it (for instance adding noise).

Another possible answer is provided by the *F-test* that was proposed by Kositsky and Avouac (2010):

$$F = \frac{\chi^2_L - \chi^2_{L+1}}{\chi^2_{L+1}} \frac{\nu_{L+1}}{\nu_{L+1} - \nu_L}$$

where ν_L is the number of degree of freedom of the $L-th$ component. In a nutshell, this test assesses the relevance of a component depending on the reduction of variance that it brings along.

A further possibility is to use the automatic relevance determination method (ARD). This method associates a precision value α_i, the inverse of the variance, with every column of the mixing matrix (i.e. to every source). A certain α_i describes how relevant is the $i-th$ source to explain our data. A large α_i corresponds to a small variance i.e. a dominance of the a priori density function on the $i-th$ column of A, therefore the $i-th$ source contribution to data explanation is suppressed. Operatively the variance associated with the posterior of each column is assessed, and if the maximum variance is more than ten times the minimum variance, the $i-th$ component in unneeded.

3.8 IC Analysis of GPS time series

The analysis spanned from 2015 to March 2018. The starting epoch was chosen to correctly highlight the seasonal signals, whereas the ending epoch was fixed considering a likely characterisitc time of $\sim$ 6 months - 1 year. The threshold of missing data, i.e. the percentage of missing data allowed in a time series in order to be included in the analysis, was fixed to 100% as those stations with large chunks of missing data and short time series were manually removed from the dataset.

In order to fix the other parameters of the analysis the *ICA search driver* Matlab code was used. It performs the IC analysis trying out all the possible combinations of centering and decomposition with different numbers of components. A basic centering was performed and a EMPCA decomposition was used as they proved to better separate the post seismic transient.

The number of ICs tried in the analysis ranged from three to five: in the study area annual and multi-annual signals are well known, this is why a minimum of three components is required. The decomposition of the signal with more than five components

added ICs which could only be associated with noise (fig. 3.6). However a three component decomposition seemed visually unsatisfactory due to a trade off among components.

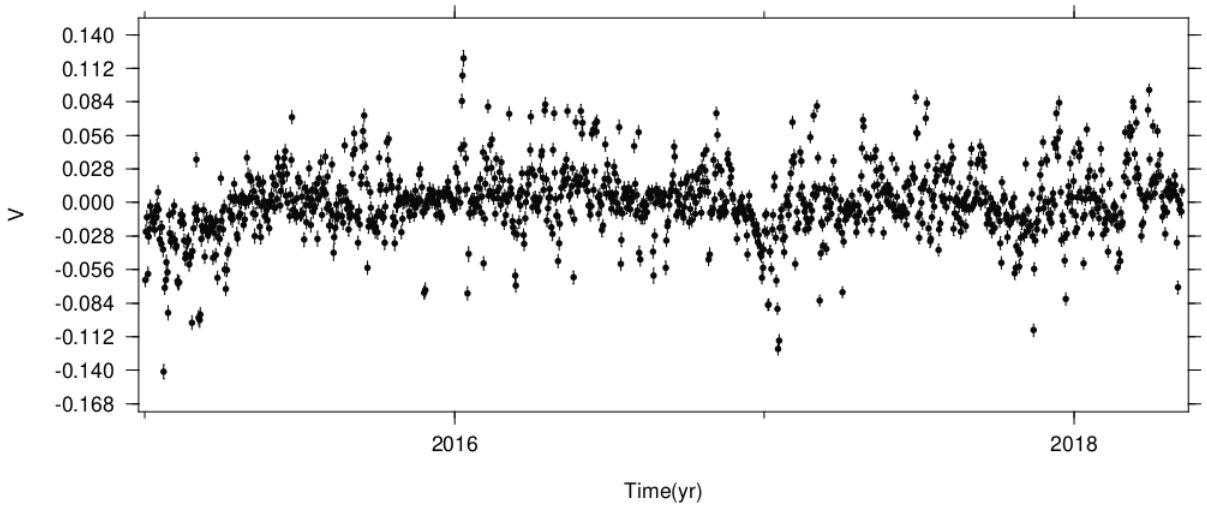

Figure 3.6. The V_6 of a six-component decomposition.

To assess the best choice, between 4 and 5 ICs, statistical tests were made:

Table 3.1

	NFE	χ^2_{red}	ARD test
4 ICs	-915628	1,25	Add component
5 ICs	-909555	1,23	Add component

Although the NFE and χ^2_{red} suggested a five component decomposition, the values obtained are comparable and eventually four ICs have been employed. The reasons for this are that even though the retrieved post seismic signal was very similar (see figure 3.7) a 4 ICs decomposition seemed to produced a cleaner transient. Furthermore the addition of the fifth component could not be associated with any phisical source.

In both cases, the post seismic transient is mapped in the first IC.

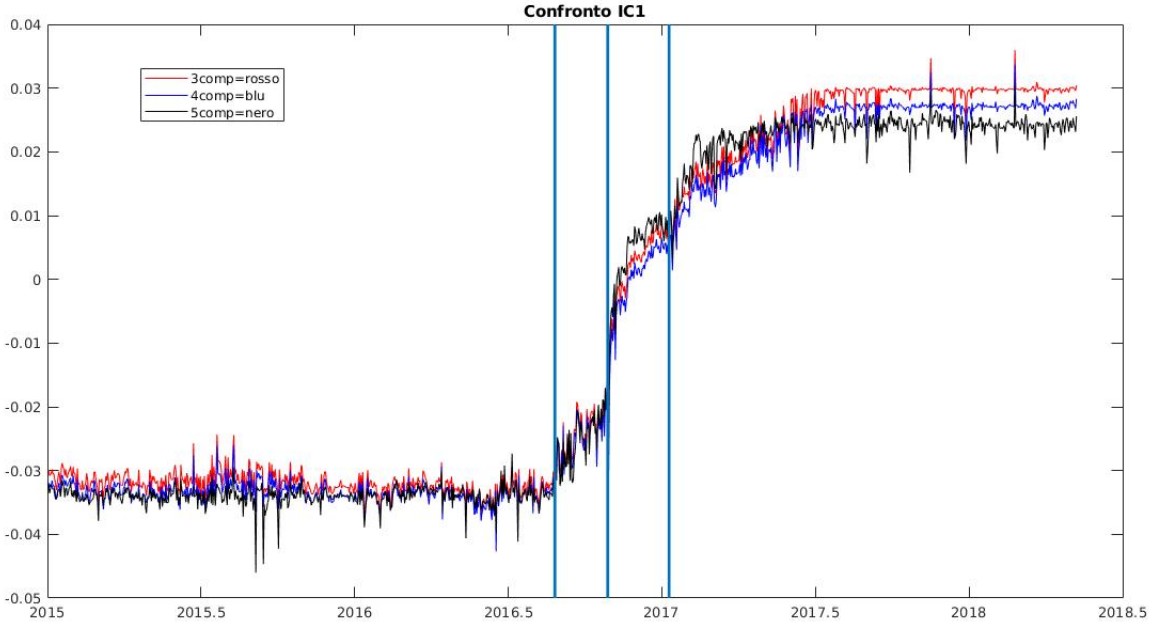

Figure 3.7. In figure the comparison of the post seismic transient mapped in the first IC, for a 3,4 and 5 components decomposition. Vertical lines mark the earthquakes epochs.

It is evident from figure 3.7 the presence of three post seismic transients: the first followed the Amatrice event, the second one followed the Norcia event (the Visso earthquake is too close in time to the Norcia earthquake to be seen), and the third one followed minor events occurred in January 2017. In our analysis these transients are mixed. An attempt to separate them through two IC analysis spanning from 2015 to the beginning of October 2016 and from the beginning of October 2016 to March 2018 has been made. It has to be stressed that the events of January 2017 showed a much smaller magnitude ($M_w \leq 5.5$, from INGV catalogue) and were not taken into account in the post seismic analysis. However the two separated analysis could not produce any component associated with the afterslip, thus a single post seismic signal, retrieved from the vbICA, has been considered for the whole sequence.

In the next figures the four temporal evolution of the Independent Components for the chosen decomposition are shown (figure 3.8) together with the detail of the temporal evolution (figures 3.9 , 3.10) and spatial response (fig 3.12) of the first component.

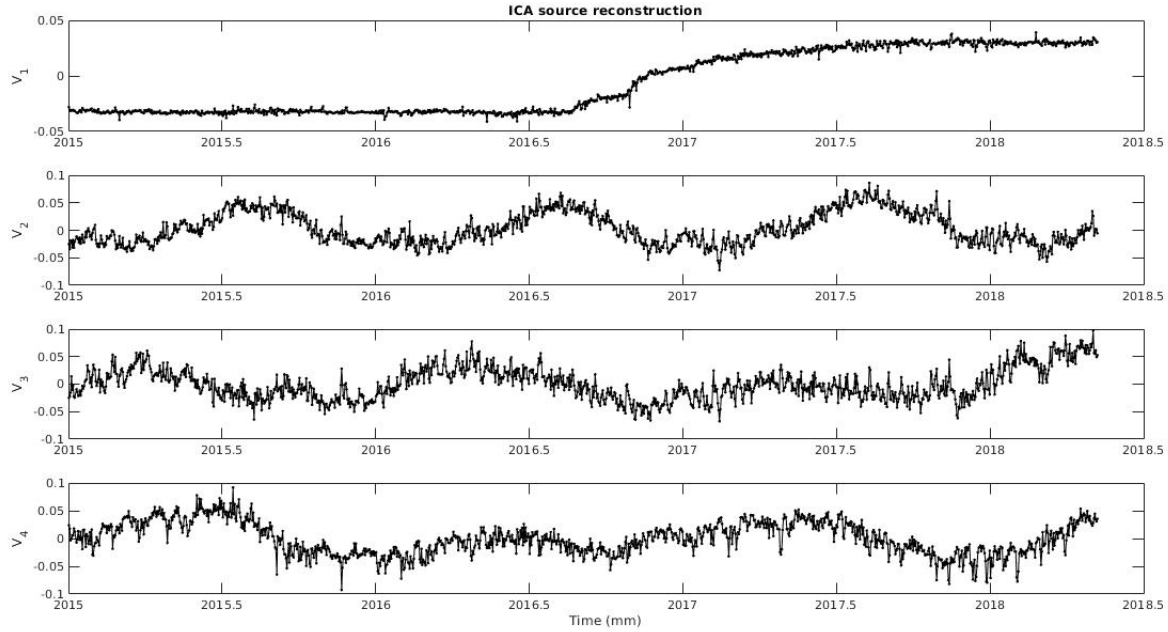

Figure 3.8. The four temporal components for the final decomposition

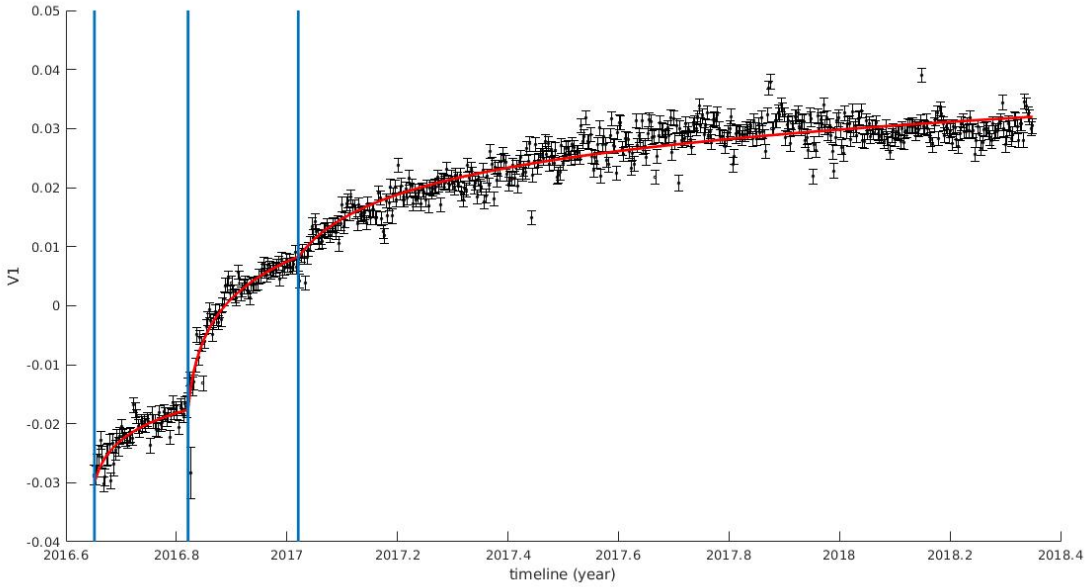

Figure 3.9. Temporal evolution of the first component (V_1) and a logarithmic fit (red line). Cyan vertical lines mark the offsets epochs.

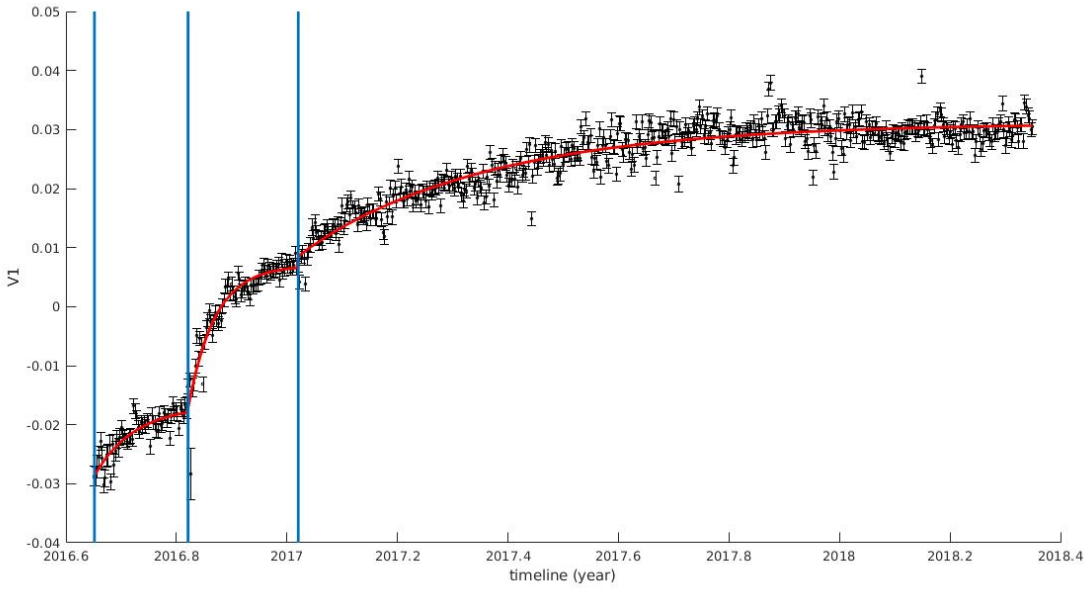

Figure 3.10. Temporal evolution of the first component (V_1) and an exponential fit (red line). Cyan vertical lines mark the offsets epochs.

Table 3.2. In table the decay time estimated through the logarithmic and exponential fit

Event	τ_{log} (days)	τ_{exp} (days)
Amatrice	6	26
Visso-Norcia	3	17
January 2017	20	125

The logarithmic fitting function for figure 3.9 is in the form of equation 1.10 section 1.4, as proposed by Marone et al. (1991). The fitting function used in figure 3.10 is as in Savage (2003). Different functions result in different decay times (table 3.2). Remarkably, the exponential form reproduces better the transient that followed the first event and the long term plateau (whereas the logarithmic function shows a consistent growth in the long period), as testified by table 3.3.

Table 3.3. In table the discrepancy among the data and the logarithmic and exponential fit

Fit	Weighted RMS	Unweighted RMS
Logarithmic	47.1	0.059
Exponential	44.3	0.055

The fit of the V_1 has been repeated in figure 3.11 considering only one post seismic transient. The decay times and the statistical values are summarized in table 3.4:

Table 3.4. In table the extimated decay times and the RMS of the logarithmic and exponential fit for a single post seismic transient

Fit	τ (days)	Weighted RMS	Unweighted RMS
Logarithmic	26	87.3	0.108
Exponential	25	53.6	0.069

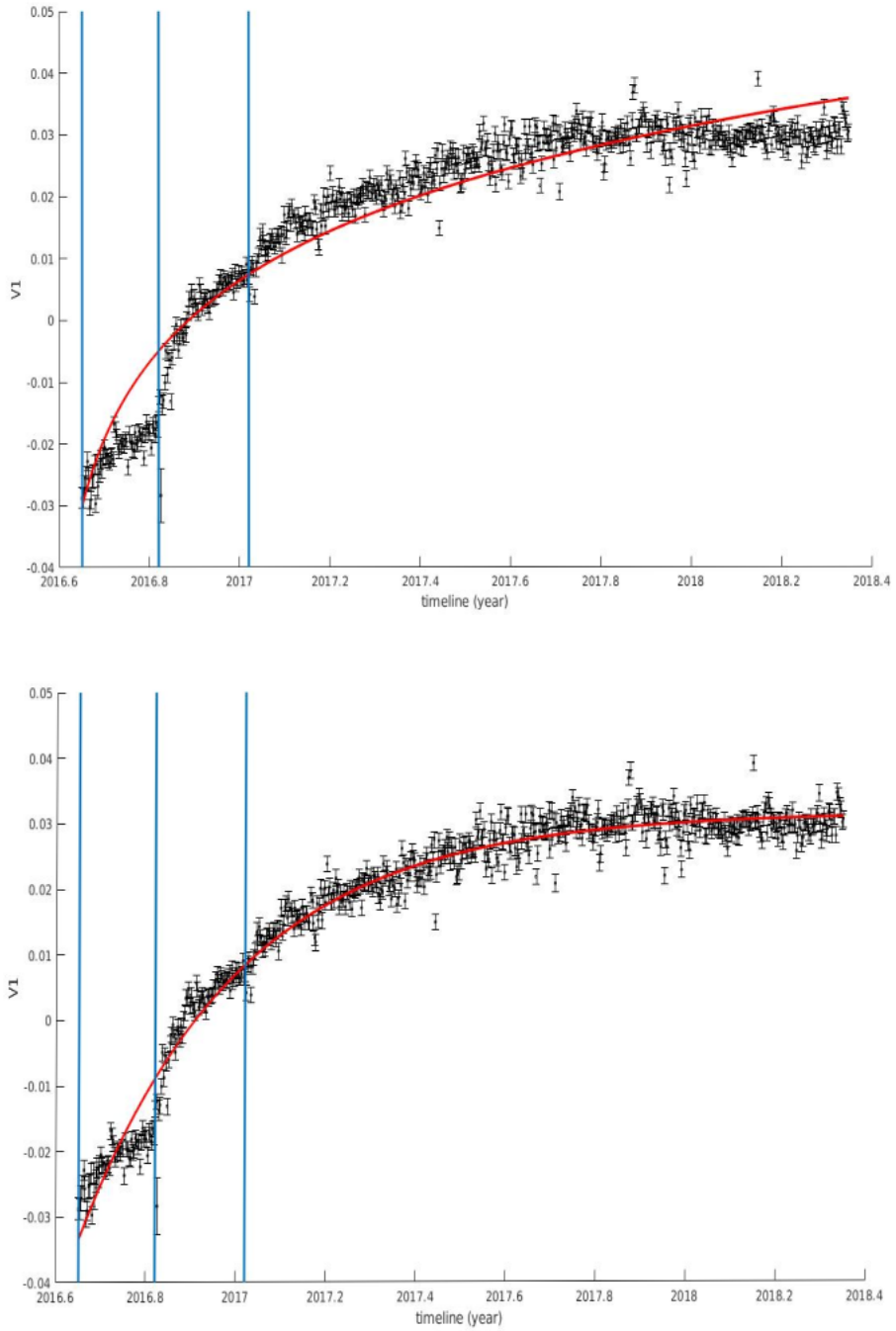

Figure 3.11. Temporal evolution of the first component (V_1) and a logarithmic (upper panel) and exponential (lower panel) fit. Cyan vertical lines mark the offsets epochs.

An exponential function reproduces the temporal evolution of the IC1 better than a logarithmic one, however the decay times obtained are very similar. As we can see both from figures and from tables 3.3 and 3.4, considering a post seismic transient for each mainshock improves significantly the fit.

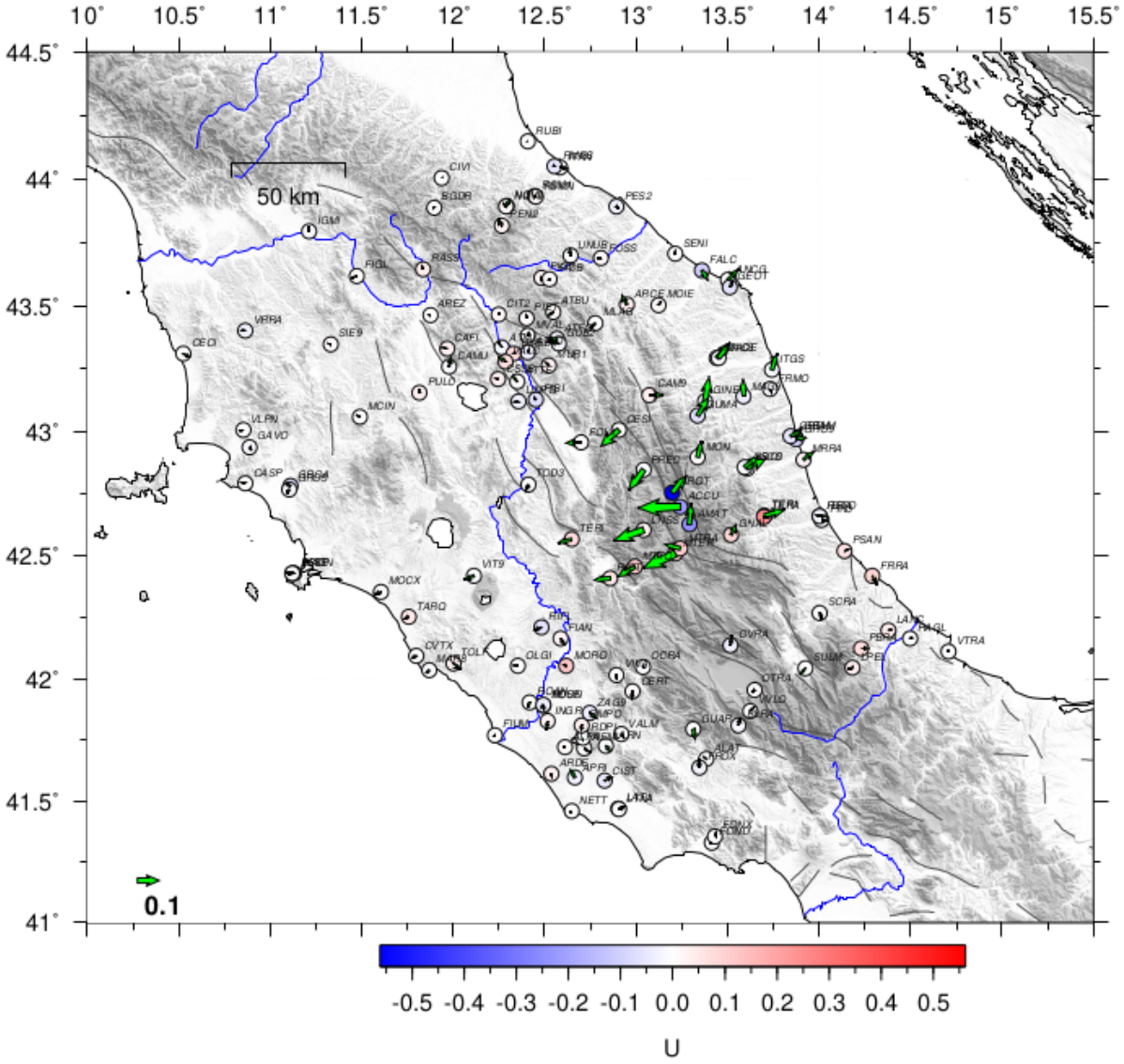

Figure 3.12. Figure shows the spatial response of stations to the first component (U_1). Green arrows stand for the horizontal response, color of circles for the vertical response.

Chapter 4

Inversion

In this chapter the procedure adopted in order to perform an inversion of the cumulative post seismic displacement will be described. As it has already been stated, this is a linear inversion of the spatial part of the first IC (i.e. the U_1) and it will eventually lead to a model of the spatial distribution of the afterslip on the activated faults.

The following steps are required to get to the final model:

- computation of Green functions;
- definition of the geometry of faults adopted in the inversion;
- regularization of the inverse problem.

The Green functions adopted, which relate slip at depth with the displacement recorded by GPS stations, are computed within the ICAIM Matlab code. Each value of the Green function (one for the slip along the dip direction, and one for the slip along the strike direction of each patch in which the faults are divided) is calculated once the dataset has been defined as it depends on the source-receiver distance.

4.1 Faults geometry

A fundamental role for the inversion of the afterslip component is played by the definition of the faults involved. The starting point were those faults already present in literature (Cheloni et al., 2017,2019), i.e. the "coseismic faults" already presented in chapter 2. Noteworthy, these coseismic solutions are quite similar for what concerns the main structures.

Such faults were modified due to the fact that afterslip usually occurs out of areas interested by co-seismic slip. Thus, the main idea was to extend the coseismic faults. The modifications were made following these criteria:

1. the seismicity pattern reveals the extension of the structures involved in the seismic event. It is an indication of the dimension of the faults (Chiaraluce et al., 2017). Therefore the post seismic faults were constructed to embed the locations of the aftershocks. This resulted in larger and deeper faults (figure 4.1). Moreover, profiles of seismicity clearly highlight the presence of an antithetic structure (see figure 4.2)

2. the presence of surface ruptures (figure 4.1) were used to costrain the faults traces

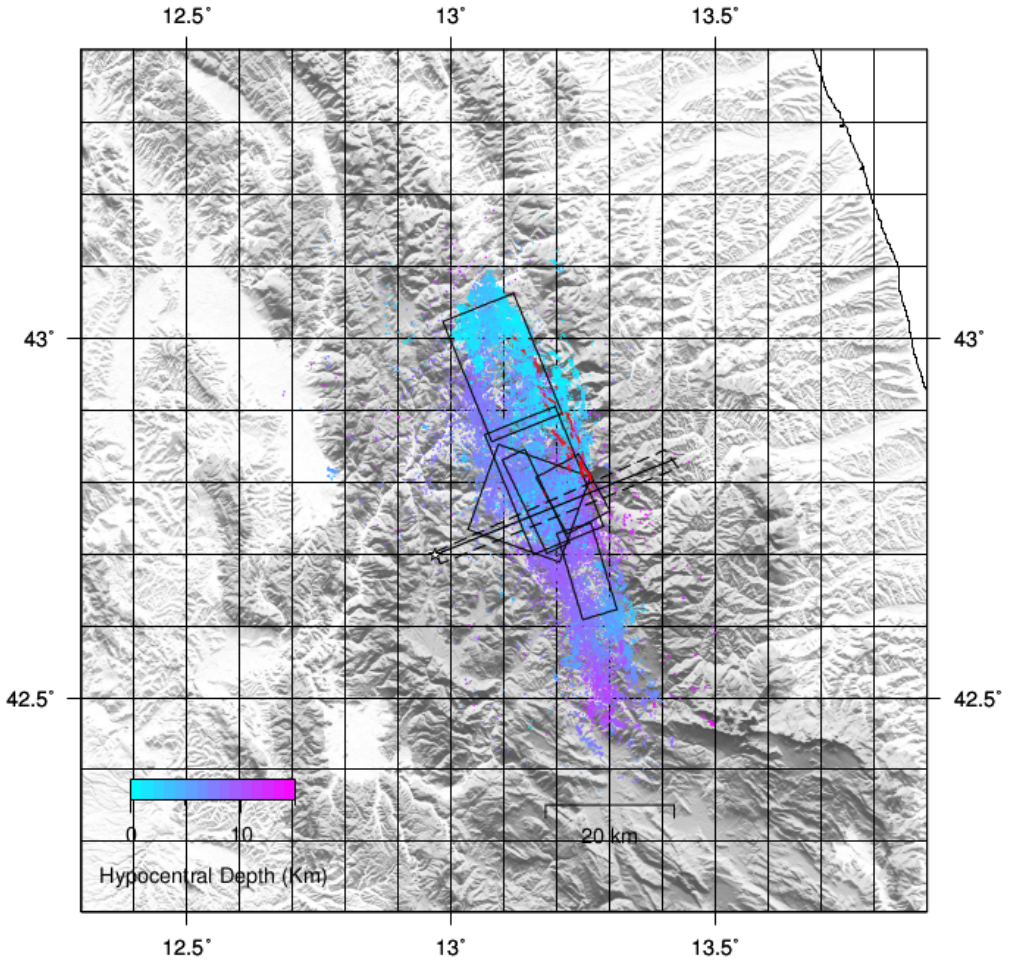

Figure 4.1. Faults drawn (black rectangles) are those from Cheloni et al. (2017), the trasverse line is the direction of the section portayed in figure 4.2. Dots show the location of aftershocks and colour their depth. Red dots represent coseismic rupture.

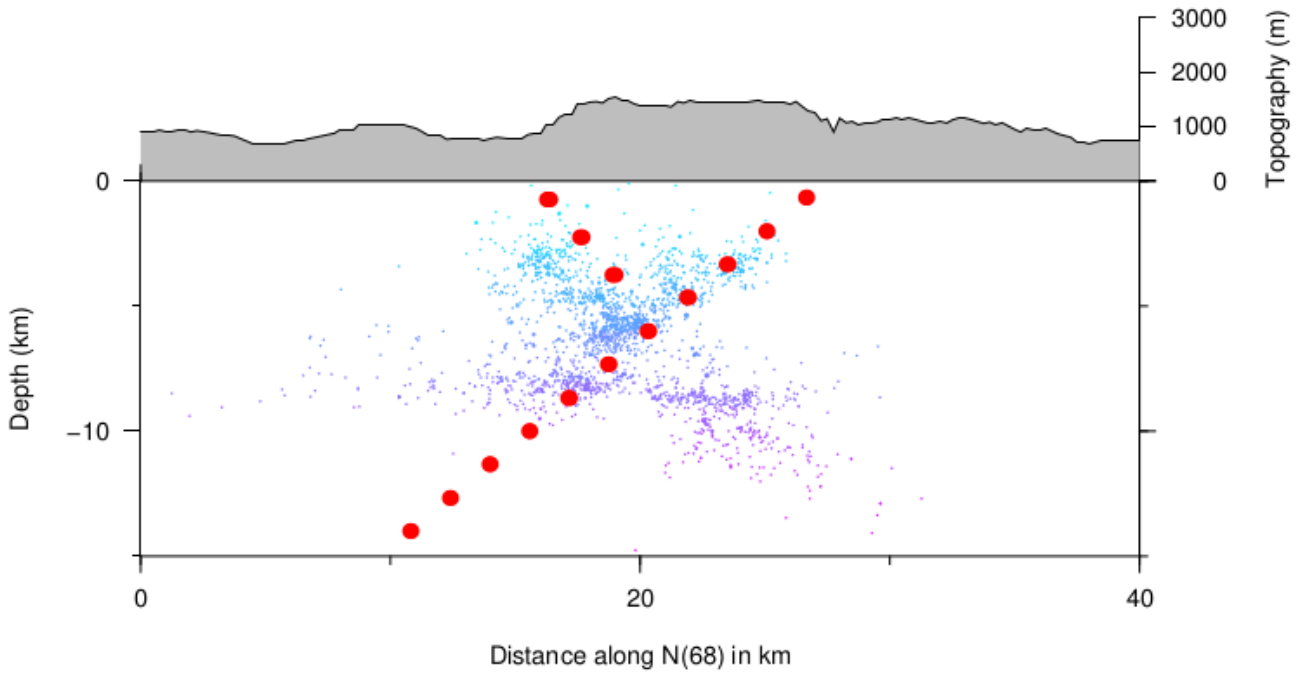

Figure 4.2. Seismic section along the 68°N direction (see figure 4.1). The presence of the antithetic faults is highlighted by red dots.

3. the coseismic solution were retrieved using not only GPS data, but also InSAR measurements, which allowed a more complex geometry of faults. Due to the overlapping of the main structures hypotesized by Cheloni et al. (2017, 2019), we were not able to find a clear solution. This is because of the high number of parameters to extimate in a small area, with little amount of available data. Thus the position of the southern fault was changed to take off the faults intersection.

The faults were subdivided in patches using the Matlab software. Provided the top left and right corner locations, depth of top and bottom of the fault, width of the fault and number of patches along the dip and strike direction, it is possible to get as an output a gridded fault. The main features of the three structure used in the inversion are summed up in the following tables:

Table 4.1. Faults adopted in this study.

		Northern main fault			
Top right corner	Top left corner	Depth top	Depth bottom	Strike	Dip
13.29°, 42.73°	13.08°, 43.13°	0 km	12 km	159°	40°

		Southern main fault			
Top right corner	Top left corner	Depth top	Depth bottom	Strike	Dip
13.40°, 42.41°	13.27°, 42.72°	0 km	15 km	163°	50°

		Antithetic fault			
Top right corner	Top left corner	Depth top	Depth bottom	Strike	Dip
13.09°, 42.88°	13.17°, 42.70°	0 km	5.5 km	339°	51°

The geometry of faults involved in the Central Italy sequence is represented in figure 4.3:

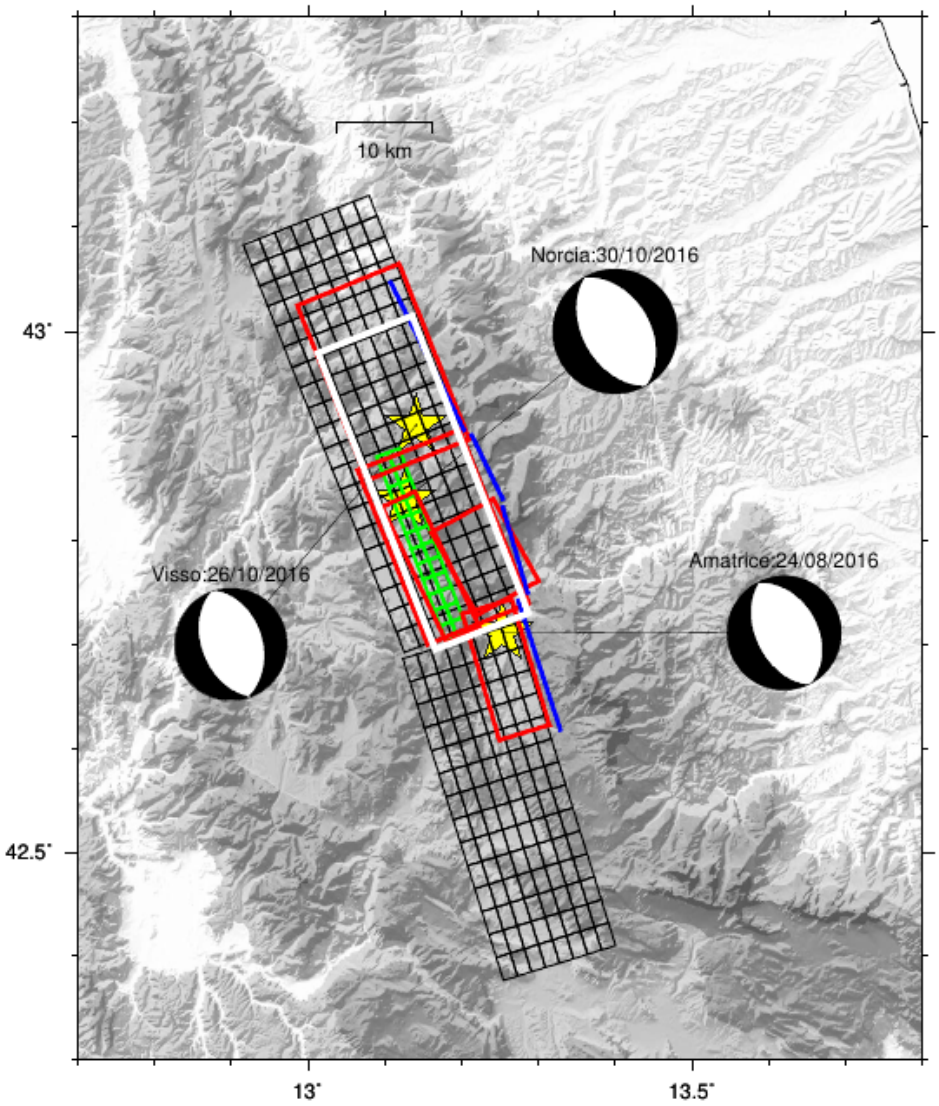

Figure 4.3. Black gridded planes are the principal faults and green gridden plane is the antithetic fault used for the inversion of the IC1. Red rectangles represent the faults in Cheloni et al. (2017); white rectangle represents the master fault for Norcia earthquake of Cheloni et al. (2019); blue lines show the trace of the principal strucures used in Walters et al. (2018). Yellow stars represent the epicenters of the events.

As it can be noticed from figure 4.3 and table 4.1 the coseismic structures are quite similar one another; the post seismic planes used in this study show the modifications that were made to such structures: indeed they are larger and reach larger depths (keeping almost the same dip and strike), and the main plains do not intersect.

The coseismic solution were also compared to the retrieved "post seismic solution", to

validate our results for both the slip distribution and slip magnitude (assessed through the seismic momentum).

4.2 Regularization

The regularization step is required when dealing with an ill-posed problem: if a problem is underdetermined there is an infinite number of solutions to it. In our case the number of unknows is equal to the slip in the dip and in the strike direction for each patch of the adopted faults (namely 614 parameters to estimate); the number of equations is given by the time-series recorded by the 139 GPS stations (more specifically three times this number as we have a time series for the east, north and up component of position). The addition of further information, which artificially make our problem overdetermined, goes by the name of *regularization of the problem*. In this case, where a slip distribution on fault planes is seeked, a common approach to regularize the problem is "smoothing" the solution.

The approach adopted in this thesis requires to tune the weights of the exponential correlation between patches as proposed by Radiguet et al. (2006) (see section 3.7, equation 3.6). Working on the length factor λ and on the standard deviation of parameters σ_m it is possible to find a plausible solution to this ill-posed problem. In particular λ defines the distance for patches to be correlated: large λ produced smoothed slip distributions and vice versa. σ_m defines the distance of the patches from the a-priori model $\mathbf{m}_0$ (which is assumed null). σ_m is implicitly assumed homogeneous for the fault, however the ICAIM Matlab code permits to assign a σ_m value to each patch, thus giving more importance to some regions of the fault (note that a small σ_m means that the solution is close to the null $\mathbf{m}_0$ model).

In this thesis different values of λ have been tried, ranging from the patch dimension (~ 2 km) to 100 km. A common approach used to assess the best value of σ_m, for every λ, is the *L-curve*. An L-curve is typically elbow-shaped an relates the $L_2 - norm$ of the misfit and the roughness of the model. Such curve is obtained fixing the λ value and carrying out the inversion for various σ_m. Both misfit and roughness depend on the couple (λ, σ_m), therefore every point of the L-curve depends on the σ_m used in the specific inversion (bearing in mind that λ has been previously fixed). Usually given a λ value, a σ_m close to the elbow point represents a good compromise between a very rough model (which would be capable of well explaining the dataset but would produce an irrealistic slip distribution) and a good reproduction of data.

However L-curves do not always assume such a regular shape and they do not always provide completely reliable parameters. Still the L-curve can be used as an indicator of the model response to the regularization parameters.

4.3 Inversion's results

As it has already been said, the inversion in geophysical problems can, in theory, lead to an infinite number of solutions. At the beginning an inversion with only the main structures has been performed: although complicated geometries for this seismic sequence are present in literature, it shall not be given for granted that all of them were active in the post-seismic phase. This very first inversion led to the following model (figure 4.4):

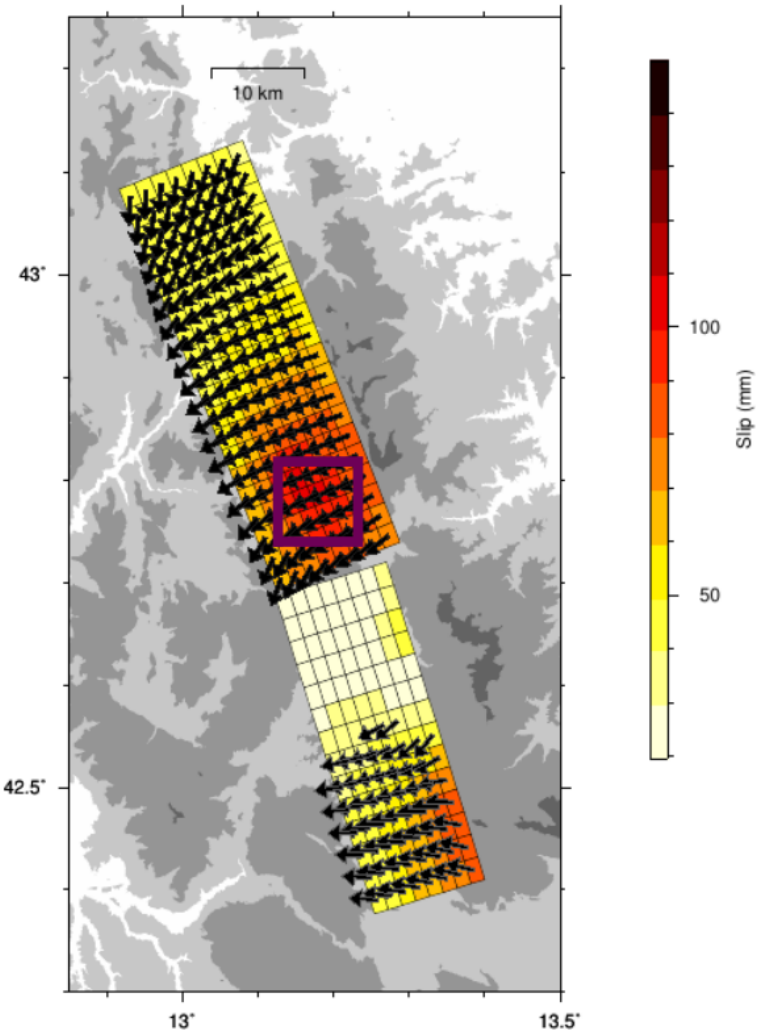

Figure 4.4. In figure the results of the inversion carried out with only the master faults. Black arrows show the slip direction (plotted only for those patches exceeding 30% of maximum slip).

Figure shows that most of the afterslip occurred on the northernmost structure, which shows a concentration of slip in the Arquata area (purple rectangle fig. 4.4) , but slipped

entirely. Slip exhibits mainly a normal behaviour. As it can be noticed, this model is unable to reproduce data, and this is particularly true for 'ARQT' station (figure 4.5).

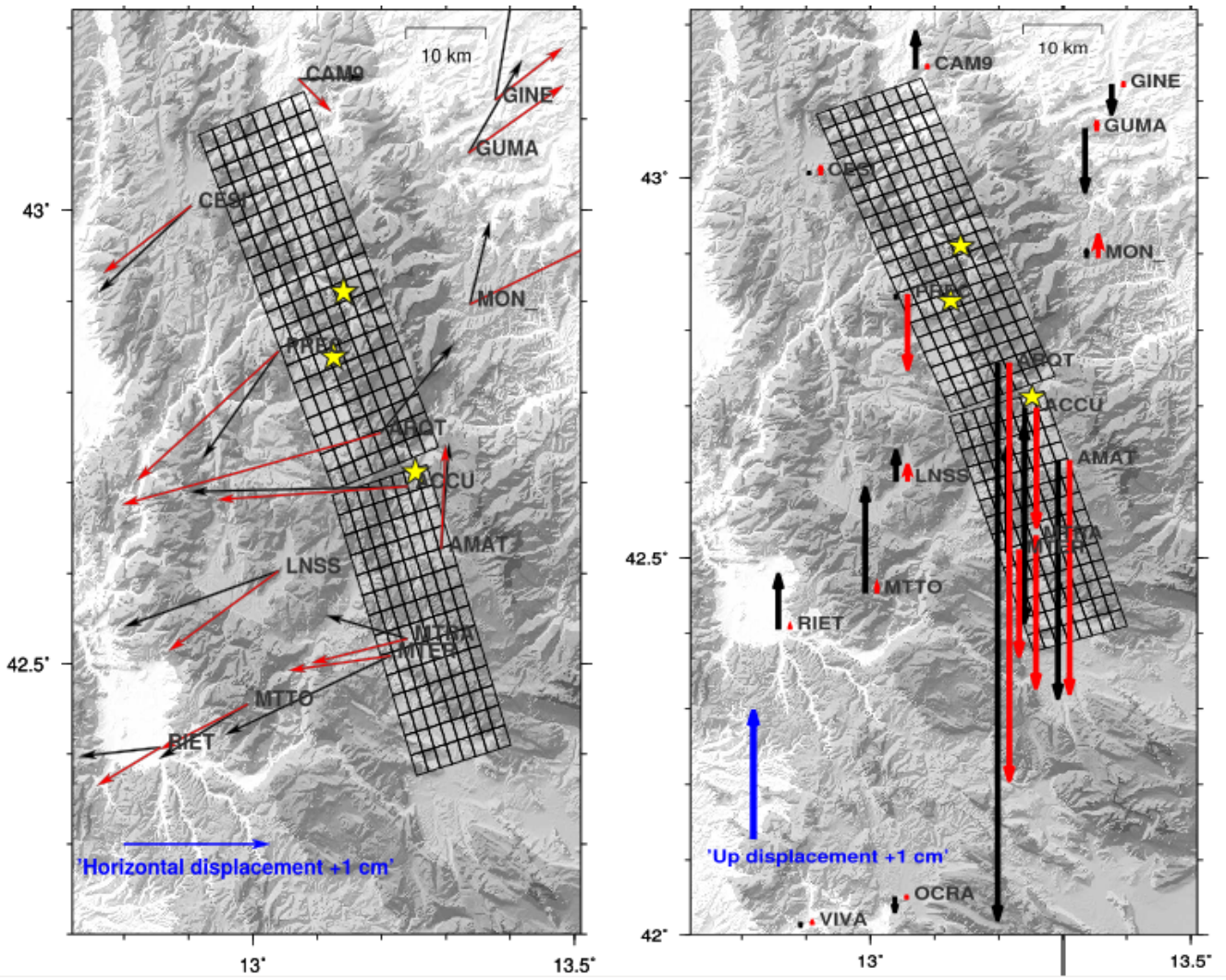

Figure 4.5. Reconstruction of the cumulated ground displacement modeled through the ICA (in a time span 24^{th} of August - March 2018) resulting from the first model. Black arrows stand for the displacement reconstructed through the ICA, red arrows the modeled displacement. Right panel embeds the upwards data reconstruction, left panel embeds the horizontal reconstruction. Blu arrows give the displacement length scale.

This led to a second inversion which accounted also for an antithetic fault:

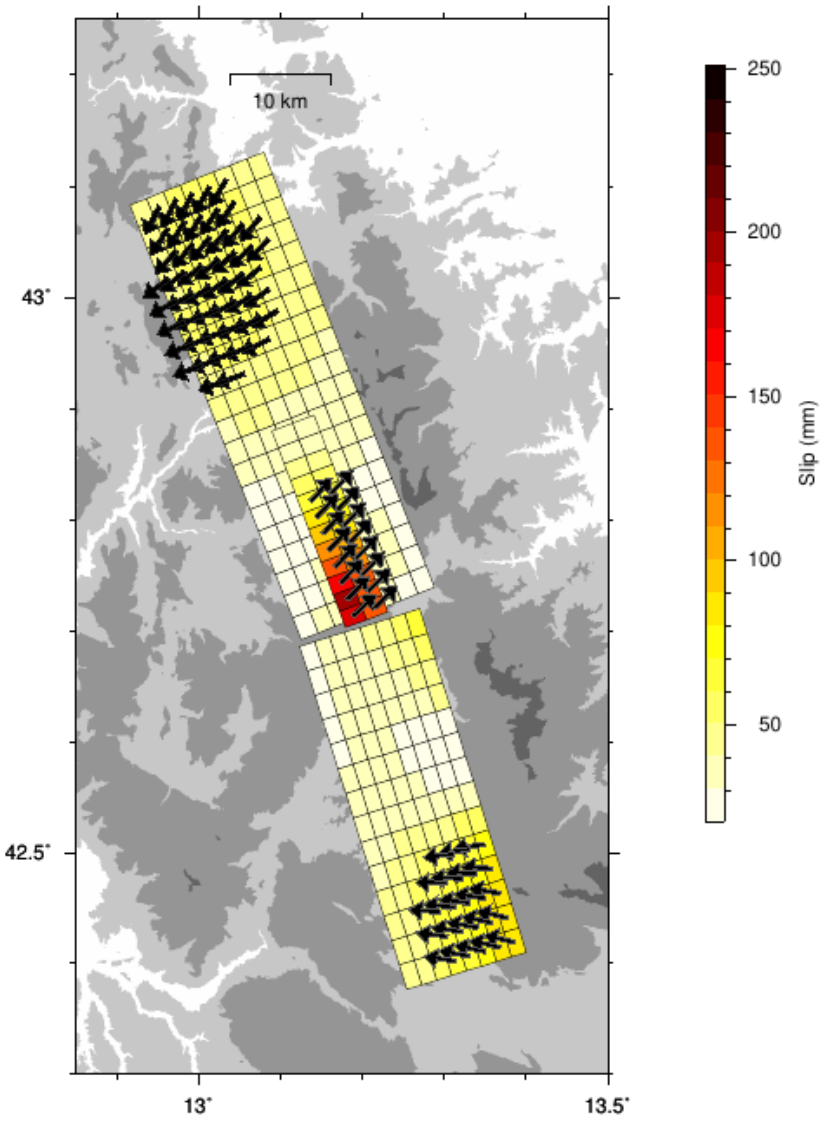

Figure 4.6. Results of the second inversion carried out with the master faults and the antithetic fault. Black arrows as in figure 4.4.

It is evident the central role played by the antithetic fault, both from the amount of afterslip that it exhibits (figure 4.6) and from the improvement of data explanation (figure 4.7).

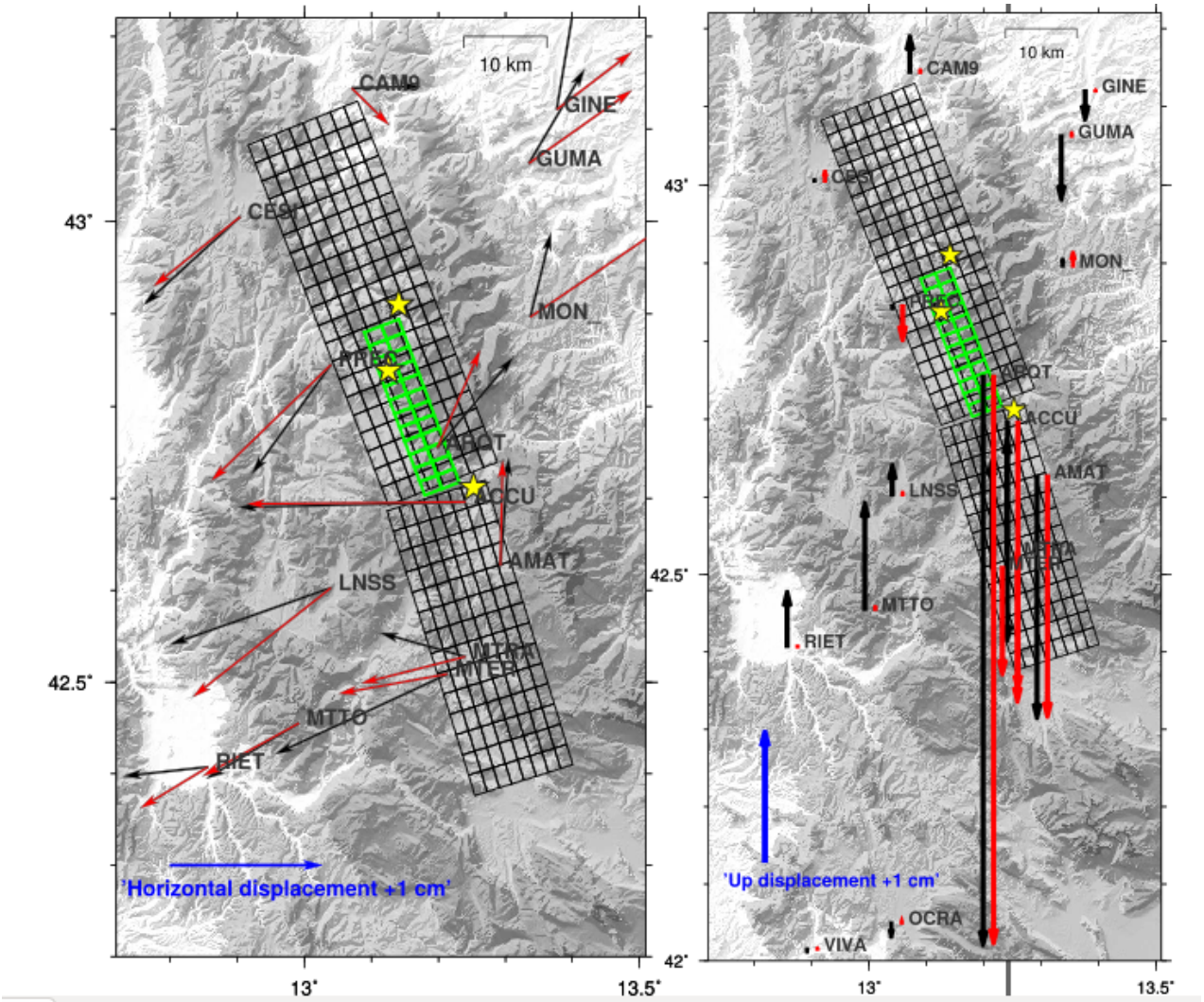

Figure 4.7. Data reconstruction (as in figure 4.5) resulting from the second model. Left panel embeds the horizontal reconstruction and right panel vertical reconstruction.

The regularization parameters selected are summarized in table 4.2

Table 4.2. Regularization parameters for the first two models

	Northern fault	Southern fault	Antithetic fault
1^{st} model	$\lambda = 35$ km $\sigma_m = 10^{-0.2}$ mm	$\lambda = 25$ km $\sigma_m = 10^{-0.2}$ mm	
2^{nd} model	$\lambda = 35$ km $\sigma_m = 10^{-0.2}$ mm	$\lambda = 25$ km $\sigma_m = 10^{-0.2}$ mm	$\lambda = 10$ km $\sigma_m = 10^{-0.35}$ mm

The characteristic lengths of correlation between patches λ chosen during the regularization are comparable to the data spatial resolution, estimated as an avarage distance among stations. The L-curve approach, previously introduced, has been used to estimate the best σ_m values.

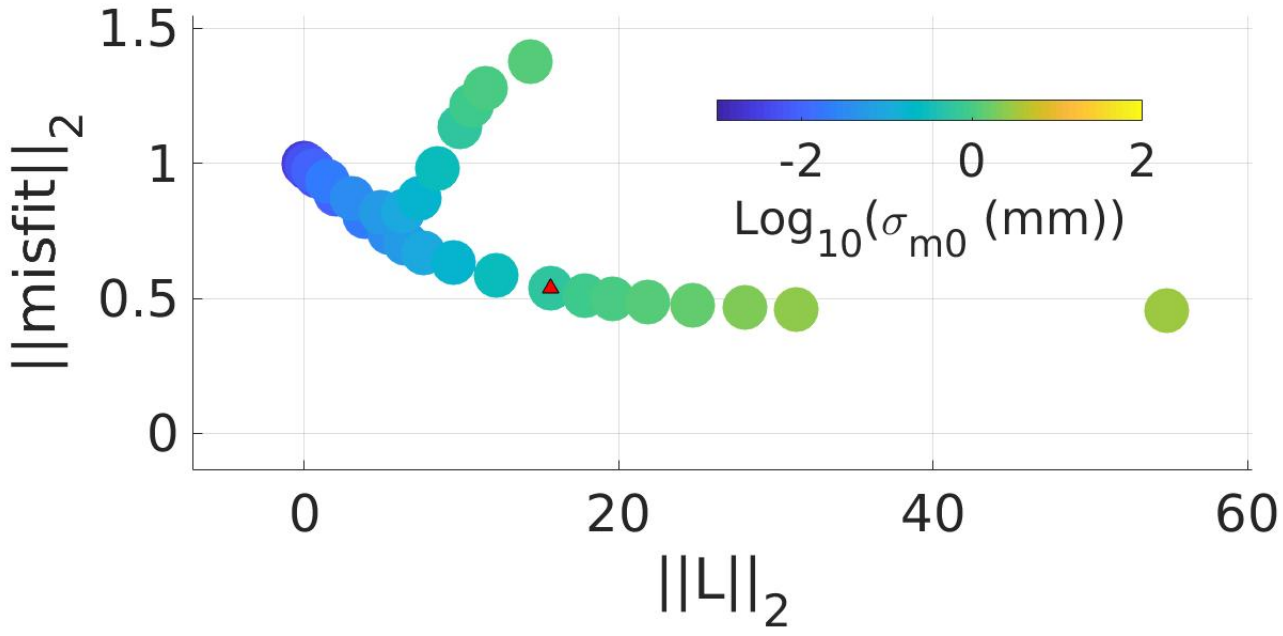

Figure 4.8. The $L-curve$ criterion for the second model. Red triangle shows as a reference the configuration with $\sigma_m = 10^{-0.25}$ mm. λ values are as in table 4.2

In this case the L-curve does not show an elbow-shaped form, in particular similar values of σ_m produce different values of $misfit$ and roughness (fig. 4.8). To draw the L-curve the same σ_m value was given to the three faults but, as it has been explained in section 4.2, it is possible to perform inversions assigning a different σ_m to each fault.

The oscillations of the L-curve have been interpreted as the necessity of a tuning of the σ_m, seeking for those values which gave a slip distribution as localized as possible and exhibiting normal fault behaviour. The red triangle in figure 4.8 is the starting point for such tuning which eventually led to the final values chosen (table 4.2).

In the next table (4.3) the $L_2 - norm$ of misfit and χ^2 are summarized for these two models:

Table 4.3. Statistics for the first two models

	$\|\|misfit\|\|_2$	χ^2	χ^2_{red}
1^{st} model	0.793	437574	0.872
2^{nd} model	0.688	298925	0.596

It is evident, both from a visual point of view (figure 4.5 and 4.7) and a statistical point of view (table above), that adding this secondary fault improves significantly the explanation of the ground displacement modelled through the ICA.

However these preliminary models do not show a convincing afterslip distribution as it is too distributed. Therefore further models have been investigated.

We get to alternative (and with a more localized) distributions shown in the following figures (first final model from fig 4.9 to 4.12, second final model from fig 4.13 to 4.15):

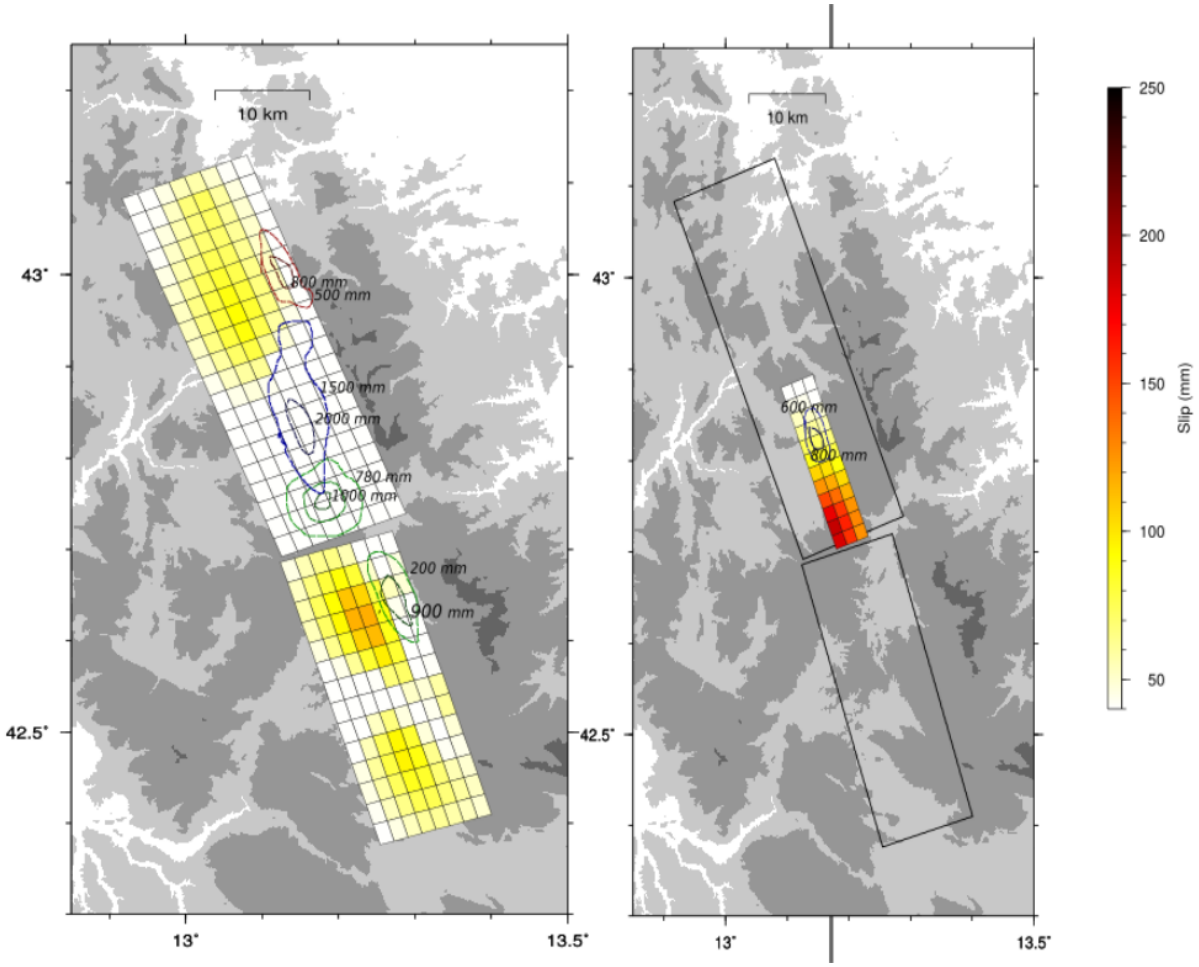

Figure 4.9. Results of the third inversion: left panel portrays the afterslip distribution on masterfaults whereas right panel on the antithetic fault. Dashed lines show the co-seismic slip distribution for the Amatrice (green), Visso (red) and Norcia (blue) earthquakes, as in Cheloni et al. (2019).

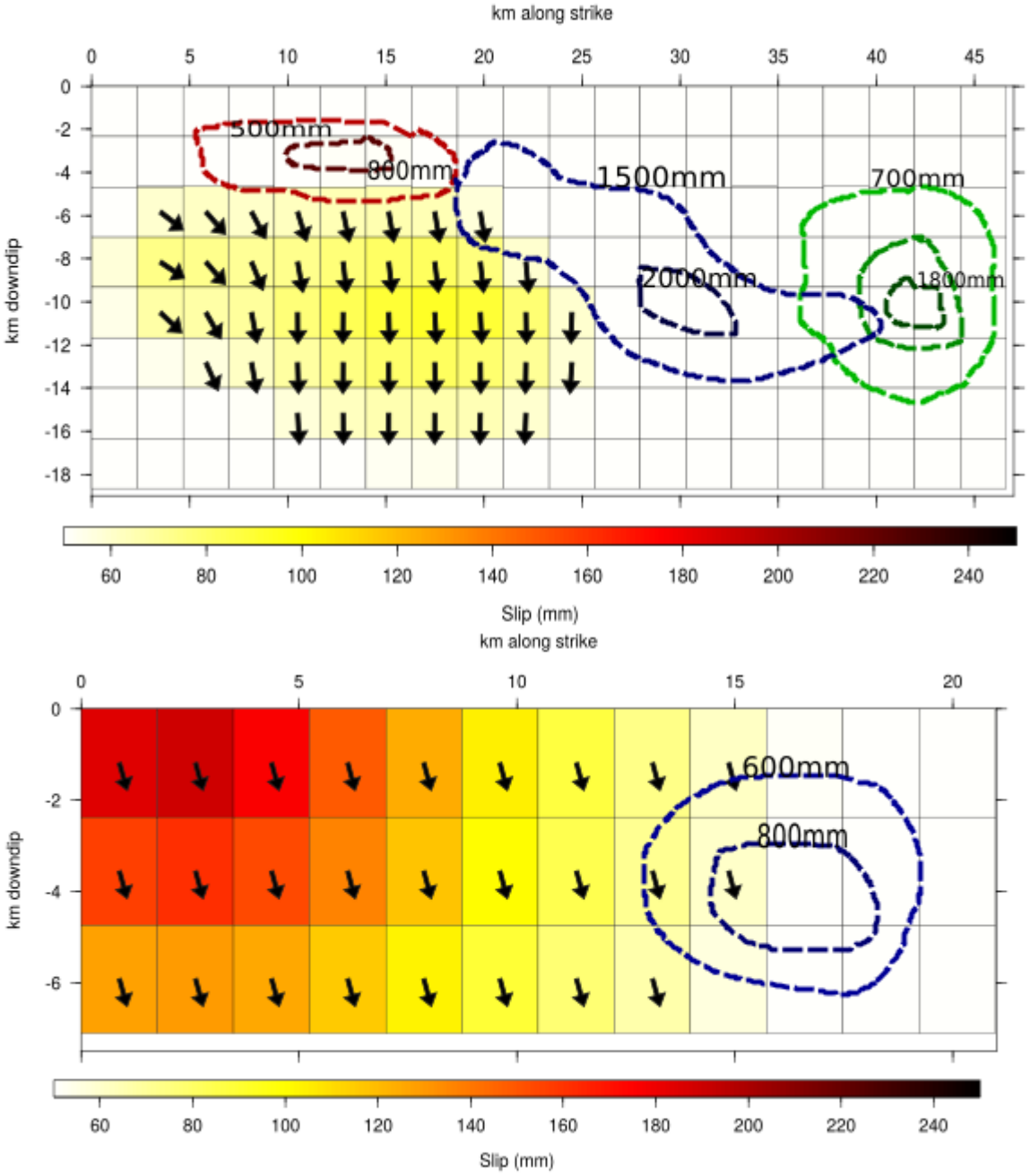

Figure 4.10. Afterslip distribution on the northernmost masterfault (upper panel) and on the antithetic fault (lower panel) in a strike-dip reference system. Rake is plotted only for those patches exceeding 30% of maximum slip. Dashed lines as in figure 4.9.

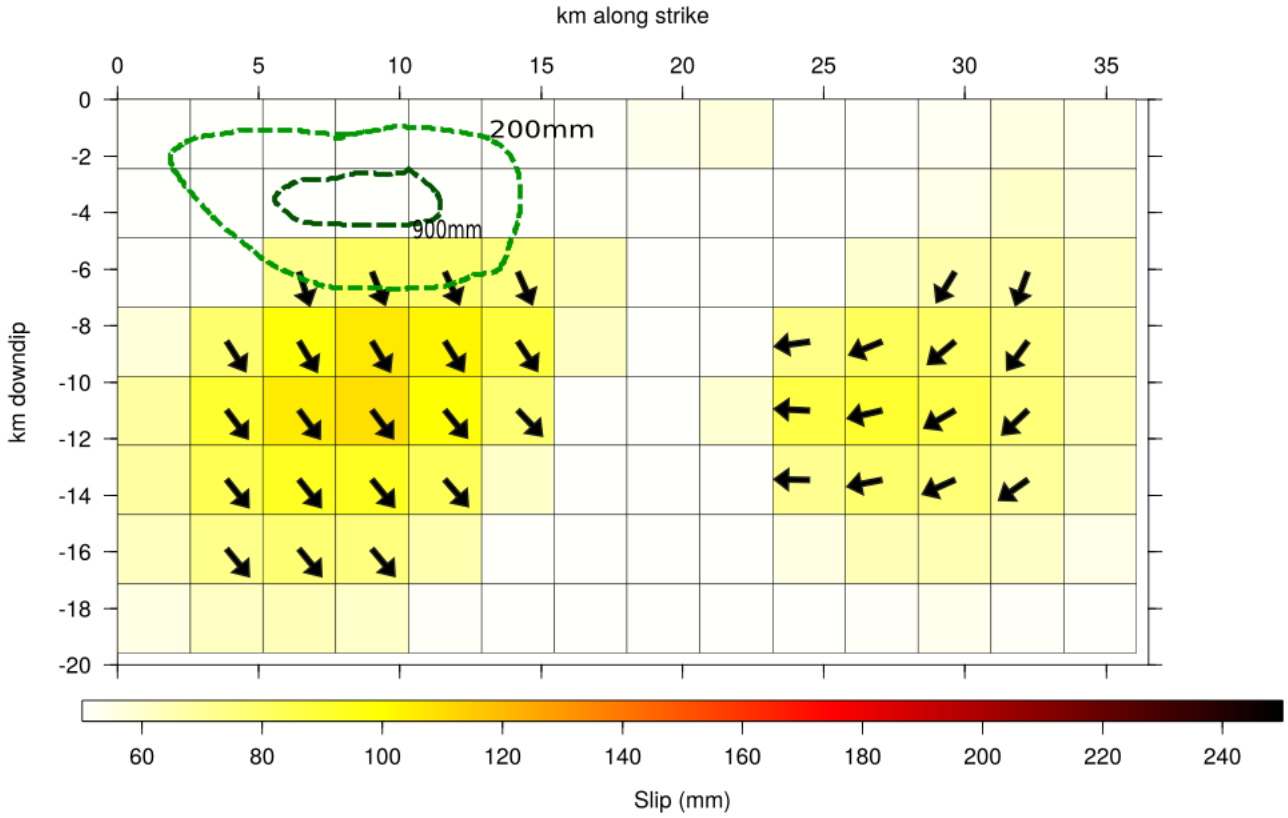

Figure 4.11. Afterslip distribution on the southernmost masterfault in a strike-dip reference system. Rake is plotted only for those patches exceeding 30% of maximum slip. Dashed lines as in figure 4.9.

This third model has both some common features and some differences with the second preliminary model: the antithetic fault is essential to the explanation of the dataset and the northernmost main fault shows an afterslip distribution concentrated in the northern patches (although it is more localized in this final model than in the previous one). On the other hand the southernmost fault shows a quite different slip distribution, with two main slipping areas instead of one placed in its upper left angle (figure 4.6 and 4.9).

The next figure shows the improvement of data explanation brought by this final model (see figure 4.7 and 4.12): data reconstruction is sligthly better for all of the near fault stations and it has considerably improved of ARQT.

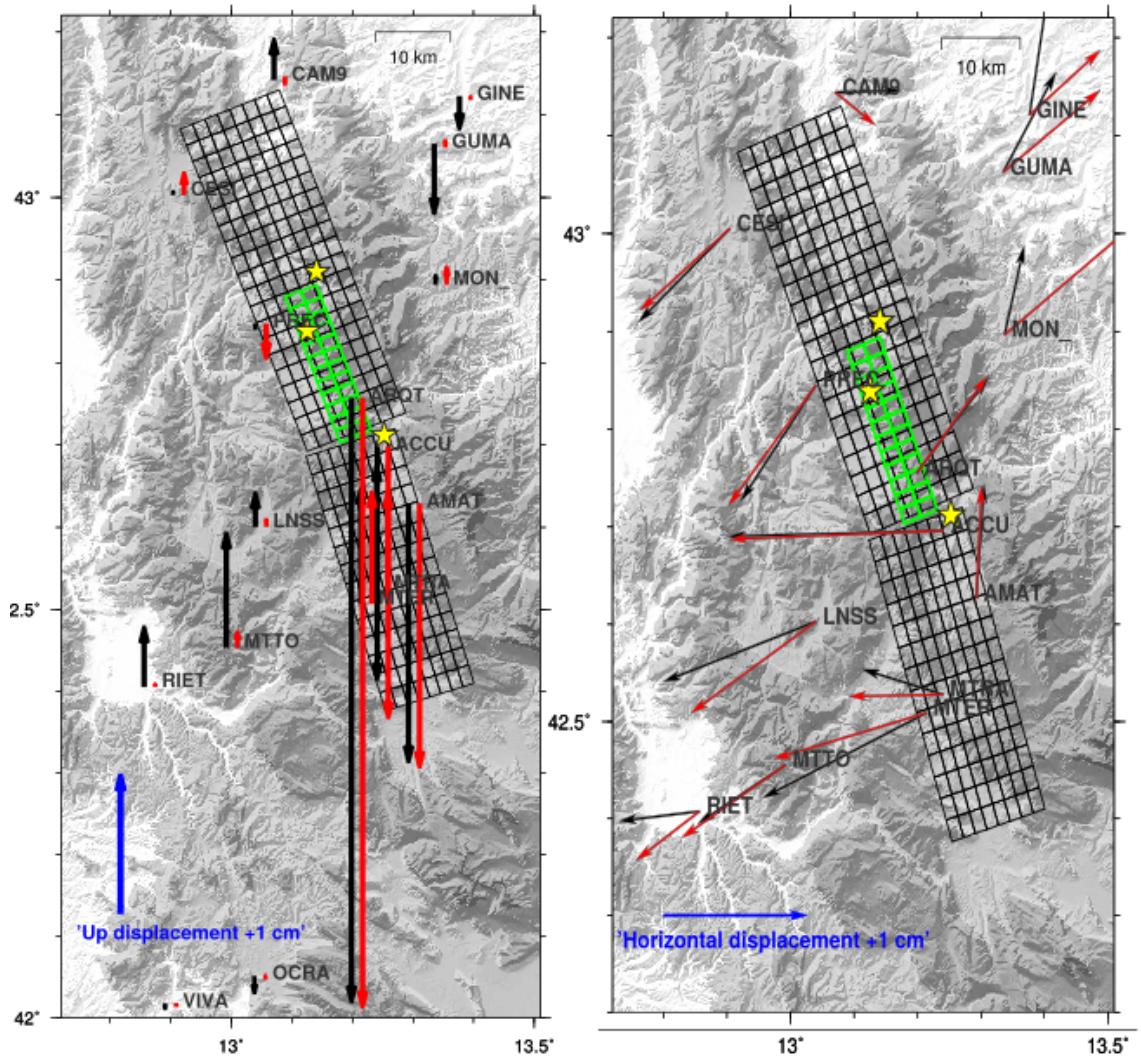

Figure 4.12. Data reconstruction, as in figure 4.5, resulting from the third model. Left panel embeds the vertical reconstruction and right panel horizontal reconstruction.

In the upcoming images the second final model is presented:

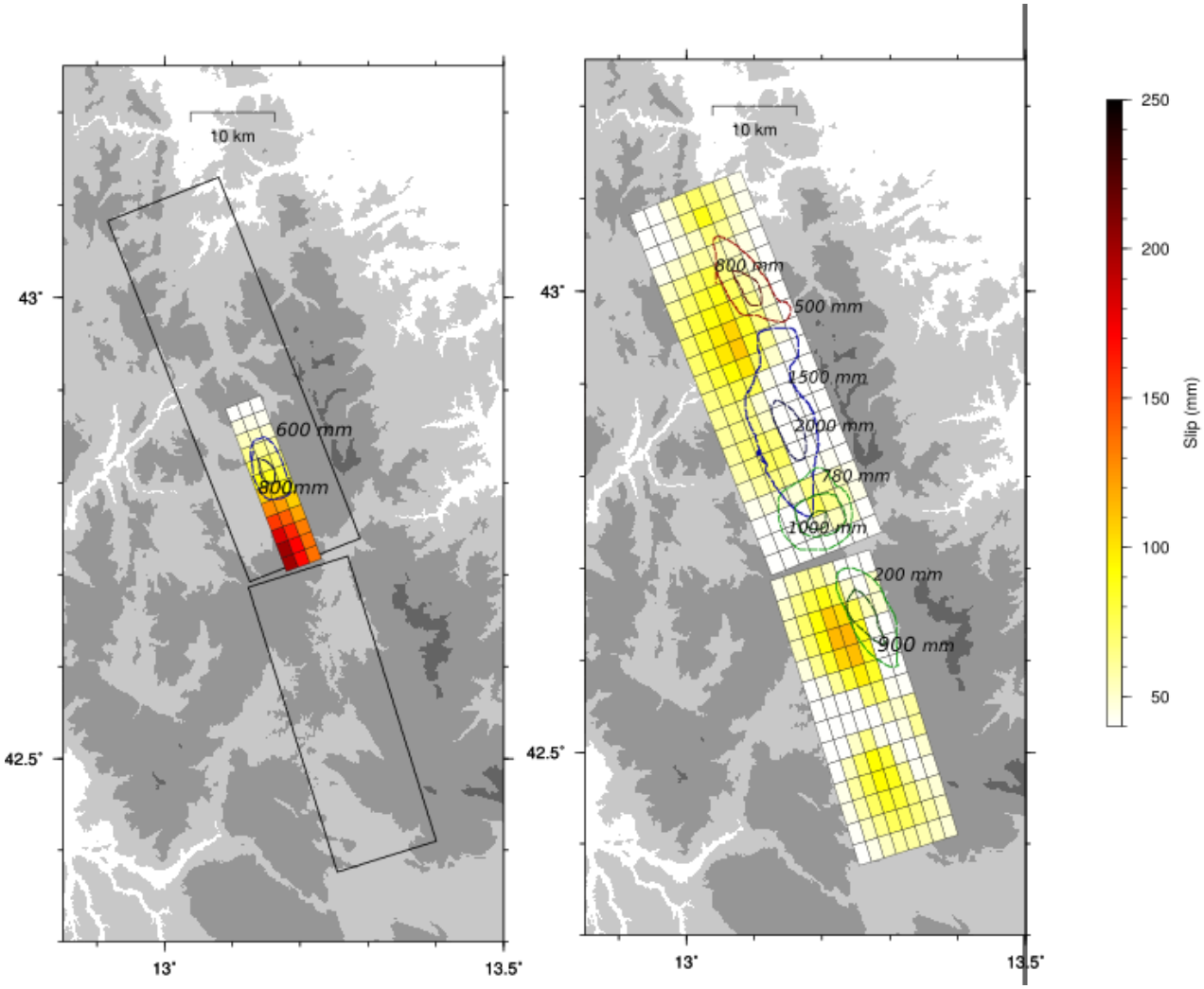

Figure 4.13. Results from the fourth inversion: right panel portrays the afterslip distribution on masterfaults whereas left panel on the antithetic fault. Dashed lines show the co-seismic slip distribution for the Amatrice (green), Visso (red) and Norcia (blue) earthquakes, as in Cheloni et al. (2019).

Basically, the main difference among the third model and this one stands in the slip distribution of the northern fault (figures 4.9 and 4.13): indeed it is more distributed in this second solution than in the previous one (see figures 4.10 and 4.14). This fact affects the maximum slip on the antithetic fault, but the situation remains the same for what concers the southern fault (figures A.2 and A.1 in Appendix A). The small difference among the regularization parameters of the third and fourth model does not significantly change the afterslip distribution of the southernmost fault, which is mostly constrained by a scarce number of stations, none of them being in its footwall.

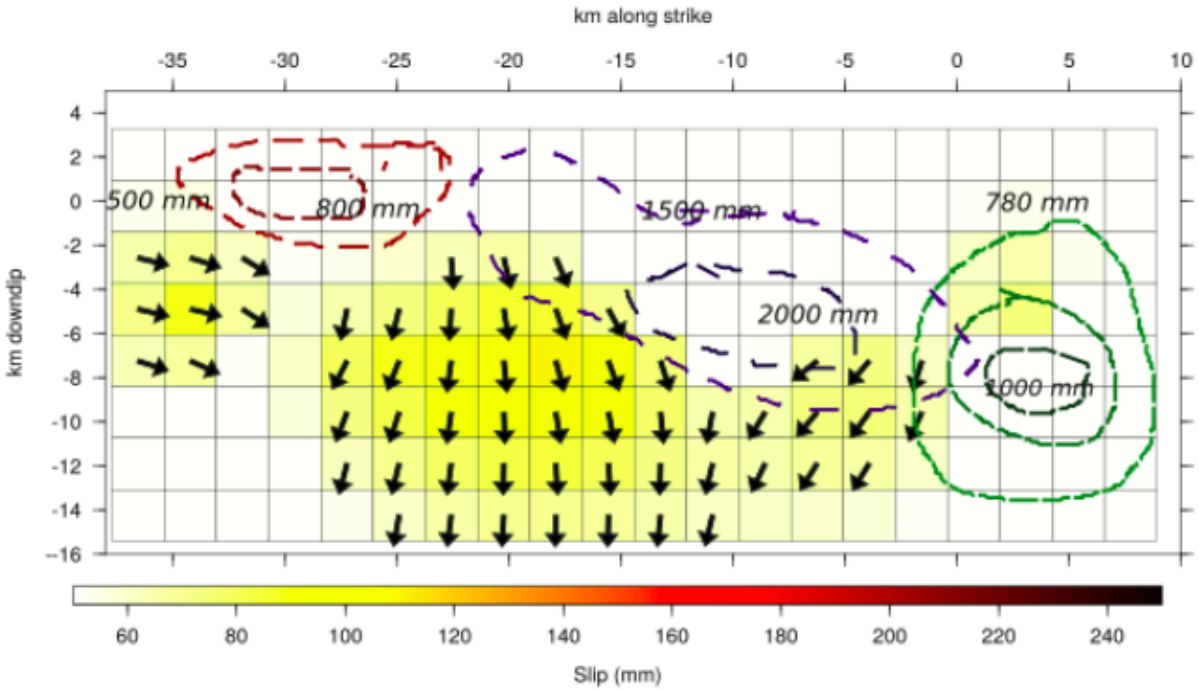

Figure 4.14. Afterslip distribution on the northernmost masterfault for the fourth model in a strike-dip reference system. Rake is plotted only for those patches exceeding 30% of maximum slip. Dashed lines as in figure 4.9.

The explanation of data does not differ much as it can be seen from figures 4.12 and 4.15 and from table 4.5.

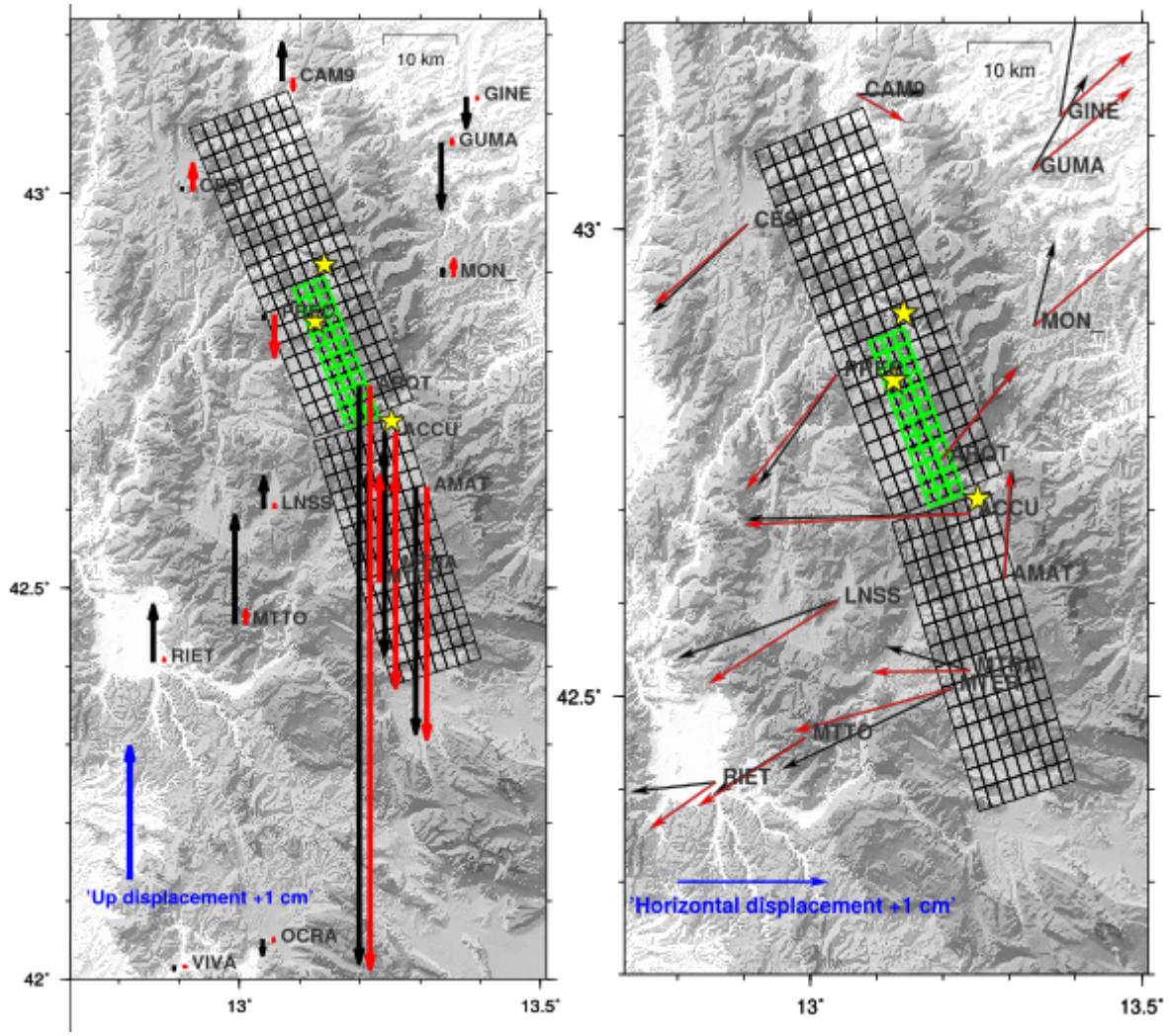

Figure 4.15. Data reconstruction, as in figure 4.5, resulting from the fourth model. Left panel embeds the vertical reconstruction and right panel horizontal reconstruction.

The regularization parameters for the final models are summarized in table 4.4

Table 4.4. Regularization parameters for the last two models.

	Northern fault	Southern fault	Antithetic fault
3^{rd} model	$\lambda = 8$ km $\sigma_m = 10^{-0.3}$ mm	$\lambda = 15$ km $\sigma_m = 10^{-0.35}$ mm	$\lambda = 10$ km $\sigma_m = 10^{-0.35}$ mm
4^{th} model	$\lambda = 10$ km $\sigma_m = 1$ mm	$\lambda = 10$ km $\sigma_m = 10^{-0.55}$ mm	$\lambda = 10$ km $\sigma_m = 10^{-0.35}$ mm

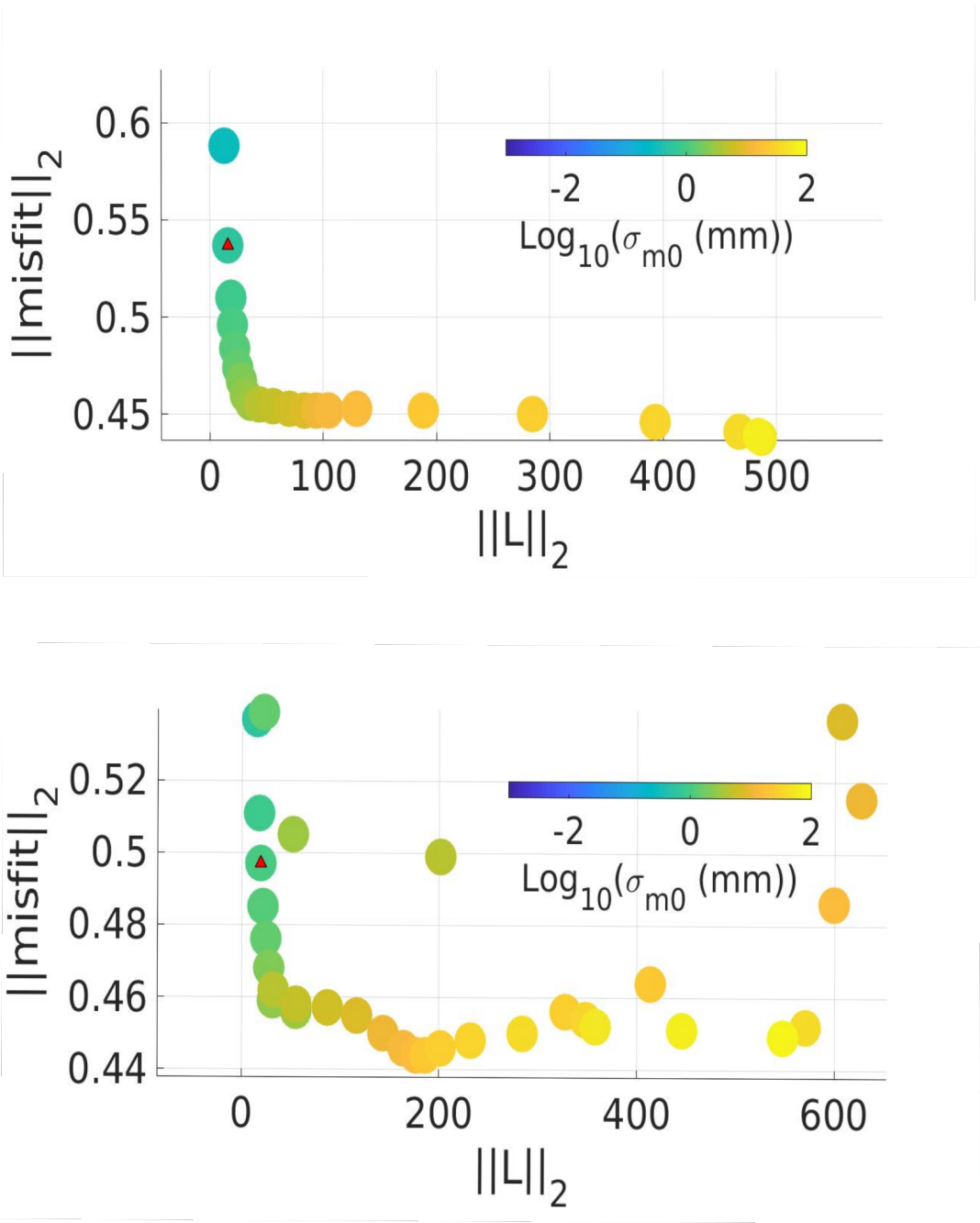

Figure 4.16. The $L-curve$ criterion for the third (upper image) and fourth (lower image) models. Red triangles refer to $\sigma_m = 10^{-0.35}$ mm (upper panel) and $\sigma_m = 1$ mm (lower panel), shown as a reference. λ values are as in table 4.4

The lengths λ for the main structures have been taken smaller than the values used in the preliminary models. This choice was made to obtain an afterslip distribution more localized.

- For what concerns the third model, the $L-curve$ shows a regular shape (upper panel of figure 4.16) that suggests a uniform choice of σ_m for the three faults. The $L-curve$ criterion would suggest to pick the regularization parameters in the corner of the curve ($10^{0.4}$ mm $< \sigma_m < 10^{0.8}$ mm). Such models have been investigated and produced patches with inverse slip. These solutions have been rejected owing to fact that the tectonic framework requires a normal behaviour. Eventually σ_m values have been taken the closest to the corner point, with the constrain of keeping a normal slip behaviour.
- The $L-curve$ for the fourth model does not show a regular shape (lower panel of figure 4.16). This fact suggests, as for the second model presented in this section, the necessity of tuning the σ_m values for the different faults. The final parameters (table 4.4) have been chosen constraining the slip to have a normal behaviour, seeking an afterslip distribution as localized as possible and decreasing to zero to the edges of the slipping areas.

The statistic values for the third and fourth models are summarized in table 4.5

Table 4.5. Statistics for the final models

	$\|\|misfit\|\|_2$	χ^2	χ^2_{red}
3^{rd} model	0.584	299742	0.598
4^{th} model	0.582	304917	0.608

Such values are quite similar one another and are comparable to those obtained for the second preliminary model (table 4.3). Even though statistically comparable, the third and fourth models show a more realistic distribution of slip than the preliminary model: the afterslip distribution is indeed more localized (figure 4.6 and figures 4.9, 4.13) and concerns patches which are complementary to the coseismic slipping areas. This is the reason why they have been chosen as final models. Having said that, it is not possible, either from a mathematical point of view, or from a physical point of view, to choose

among the two definitive models which, in principle, can both represent the selected solutions.

In figures 4.17 and 4.18 the time series derived from IC analysis (black circles) and the modeled data (red lines) is portrayed. The model here exploited is the last one, but the data reconstruction is similar to the one of the third model as testified by table 4.5, figures 4.12 and 4.15.

The most significant components of the four near field stations portrayed are well reproduced, whereas the model shows some discrepancies with the less significan ones (see the scale of the east time series of AMAT (fig. 4.17), the vertical time series of CESI and the north time series of ACCU (fig. 4.18)).

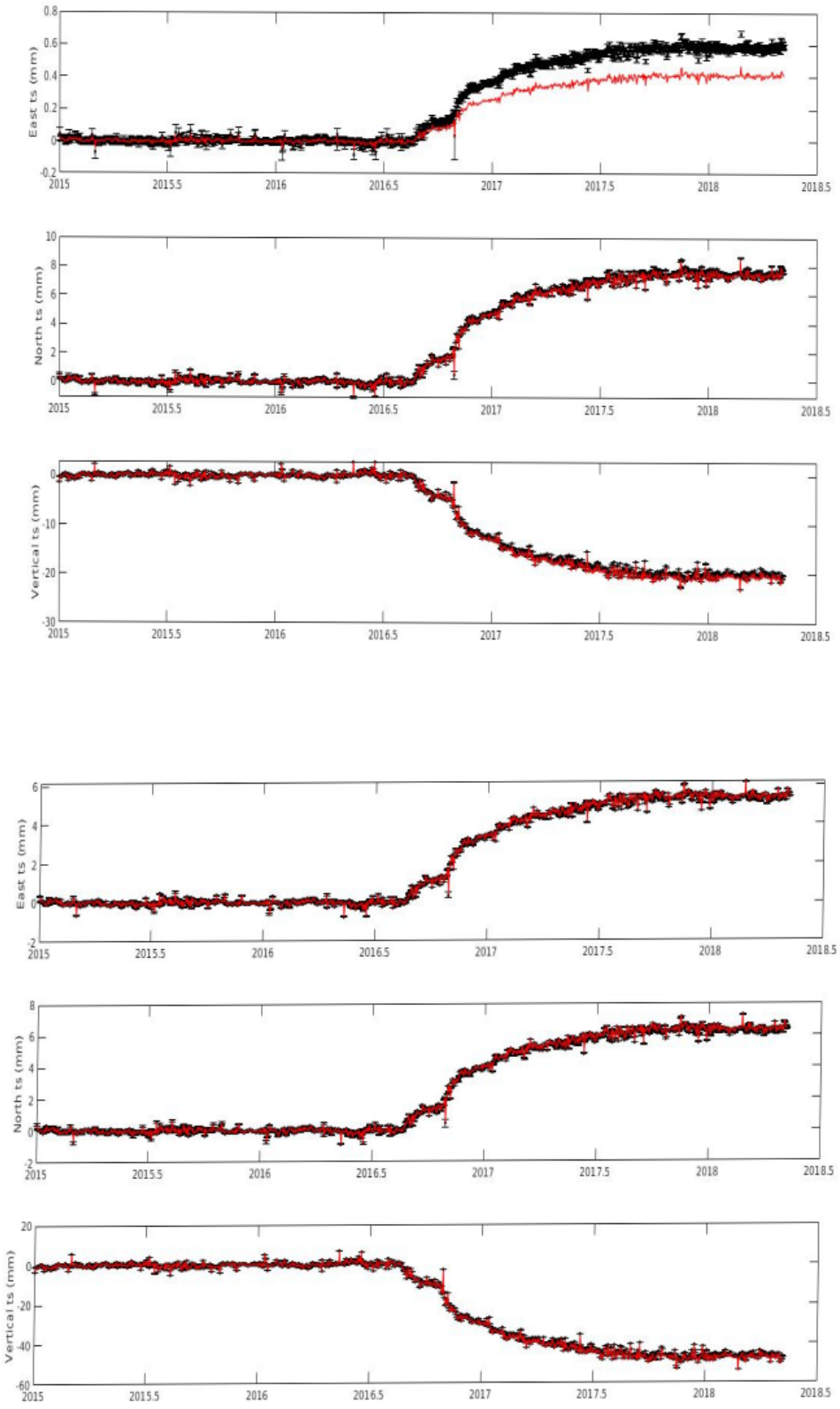

Figure 4.17. Figure shows the ICA reconstruction (black circles) and the data modeled (red lines) along the east, north and up direction (respectively upper, middle and lower panel), for stations AMAT (upper panels) and ARQT (lower panels).

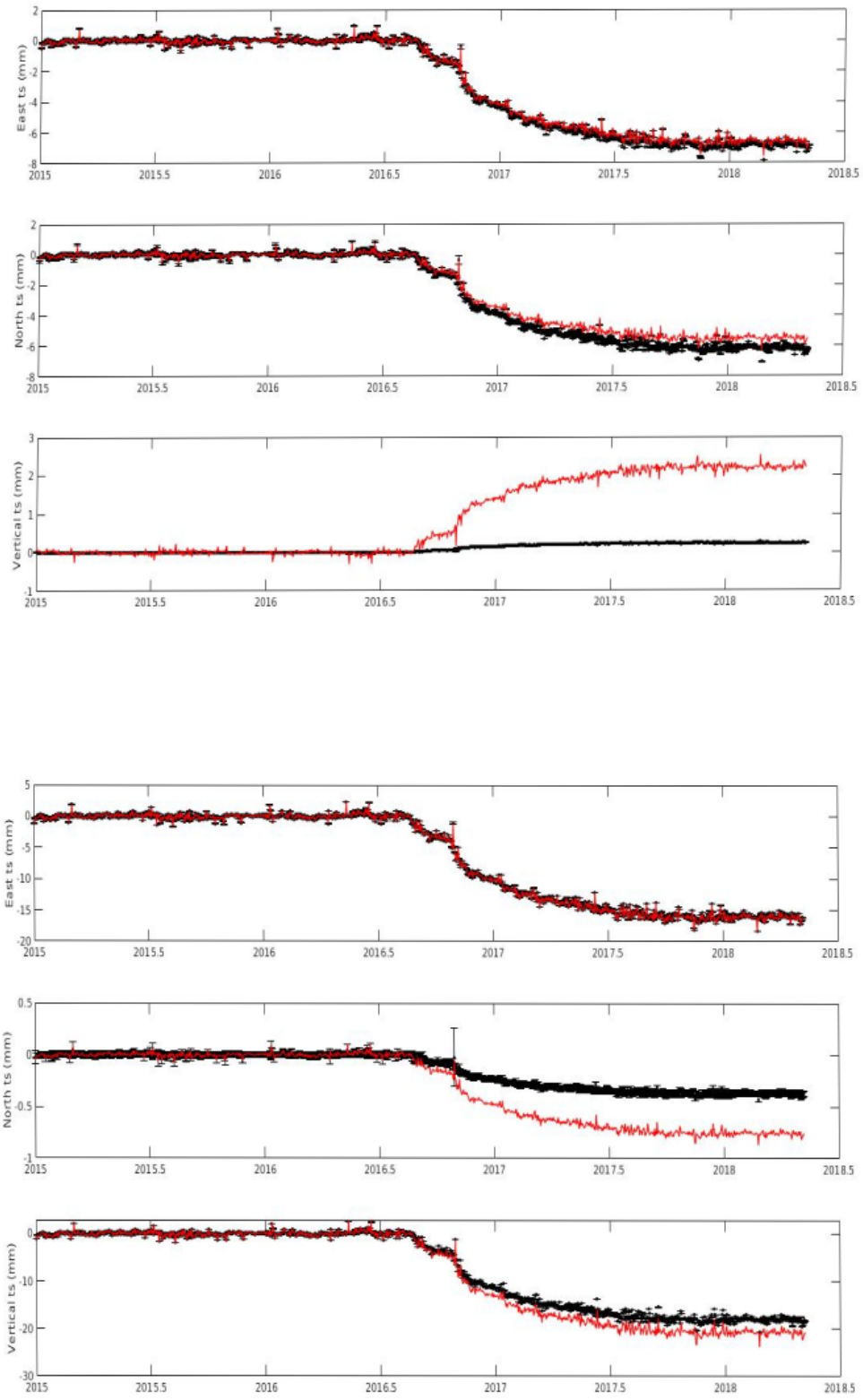

Figure 4.18. Figure shows the ICA reconstruction (black circles) and the data modeled (red lines) along the east, north and up direction (respectively upper, middle and lower panel), for stations CESI (upper panels) and ACCU (lower panels).

Chapter 5

Conclusions

In this thesis ground displacements time-series recorded at GPS stations have been analyzed to retrieve, and eventually invert, the post seismic transient deformation which followed the three main events that struck Central Italy in 2016, in order to investigate possible scenarios of afterslip distribution.

As it has been explained in section 3.8, three post seismic transients can be distinguished in the IC1 (fig. 3.9): the first one followed the Amatrice earthquake, the second one followed the Visso and Norcia earthquakes (which occurred in a time span of only 4 days and are therefore indistinguishable), the third one followed the minor events of January 2017. This latter overlapped with the Norcia post seismic signal and, due to the fact that the January 2017 earthquakes had a much smaller magnitude than the Norcia earthquake, did not significantly modify it. An attempt to separate the Amatrice post seismic signal and the Norcia post seismic signal (which includes the Visso, Norcia and the January 2017 events) has been made. The vbICA was not able to isolate the single post-seismic signals associated with each mainshock. We tried to perform analyses on specific time-intervals, but the limited number of epochs between the events makes very difficult to clearly separate the three expected post-seismic decays, therefore our study takes into account only one post seismic transient for the whole sequence.

As it has already been mentioned, our final solution consists of two alternative models, namely the third one (fig. 4.9) and the fourth one (fig. 4.13) proposed in the last section of the previous chapter. It is worth repeating that, even though the second model presented shows, on the whole, a better agreement with data (see tables 4.3 and 4.5 which summarize the $||misfit||_2$ and χ^2), it cannot explain just as well near field data (fig. 4.7). Eventually it has been ruled out due to the slip distribution that it proposes (fig. 4.6), indeed afterslip is unlikely to occur on the corners of faults and in such a distributed shape. Thus the second model is likely to have overfitted the data. Remarkably, even widening the faults surface of the second model, afterslip is always localized on the edges of the faults.

As it has been stressed out in the previous section the final models share some similarities:

1. Starting off from the explanation of data, their capability is comparable. This can be immediately spotted from maps (figures 4.12 , 4.15), but also comparing the $||misfit||_2$ (respectively 0.584 and 0.582) and the χ^2_{red} (respectively 0.598 and 0.608).

2. The antithetic fault plays a key role in the post seismic phase, as the highest values of afterslip are found on this plane ($\sim$ 20 cm).

3. On the southern principal fault mainly two groups of patches slipped : the northernmost area shows prevalently a normal behaviour with maximum slip of $\sim$ 13 cm, the southernmost area shows a transcurrent behaviour with maximum slip $\sim$ 10 cm. This situation holds for both models.

Some differences arise when it comes to the northern principal fault: in the first model slip is more concentrated and occurs mainly in the northern part of the plane (below the Visso coseismic rupture, fig. 4.10) with a maximum value of $\sim$ 10 cm. In the second model slip spreads over a wider area with a maximum of $\sim 10 - 11$ cm occurring between the Visso and the Norcia coseismic rupture (fig. 4.14). Some slip ($\sim 7 - 8$ cm) is also present below the Norcia coseismic rupture, and on the northermost edge of the plane (maximum slip $\sim$ 10 cm).

The solutions here presented suggest that the antithetic fault accomodates most of the afterslip. From the comparison between figure 4.5 and figures 4.7, 4.12, 4.15 it is clear that, under the ICAIM assumption that the observed postseismic deformation (IC1 in our case) is due to afterslip, and supposing that afterslip occurs on normal faults, the ARQT station components cannot be explained without considering the antithetic fault and, more in general, the addition of such fault brings a significant improvement of data explanation for the whole GPS network. As we saw in the introduction (section 1.3), according to Rice and Gu (1983) besides afterslip (mechanism (ii) in figure 1.5) other physical mechanisms can promote time-dependent strain changes following an earthquake. Time dependent localized subsidence of $\sim$ cm was observed in the first two weeks after the Norcia earthquake by Pousse-Beltran at al. (2018), exploiting time series acquired through Sentinel-1A/1B SAR. According to such study, the deformation is located in the south extremity of the Norcia coseismic rupture, near Arquata del Tronto, and has been associated with the drying up of the aquifer present in that area (Petitta et al., 2018). Pousse-Beltran at al. (2018) propose that this localized deformation is mostly due to afterslip on the OAS thrust (section 2.1.1), but a role of poroelastic deformation (physical mechanism (iii)) in figure 1.5) cannot be ruled out.

Cheloni et al. (2019) proposed aseismic slip occurring in the coseismic phase on the same antithetic fault here considered to develop afterslip during the postseismic phase. However they exploited the ALOS-2 interferogram which involves the 28 October 2016 - 11 November 2016 acquisitions. Such interferogram includes also the initial post seismic phase. Therefore in this thesis, part of the coseismic-aseismic slip proposed in Cheloni et al. (2019) might have been interpreted as early afterlip on the same fault, which in particular explain the deformation of the crust observed by Pousse-Beltran at al. (2018), as an alternative to afterslip on the OAS thrust or poroelastic deformation. As a matter of fact, slipping areas in Cheloni et al. (2019) (figure 2.8) partially overlap with the slipping areas of the models proposed in this thesis (fig. 4.10).

Afterslip on the masterfaults appears to be complementary to the coseismic slip retrieved by Cheloni et al. (2017), (2019): in particular the northernmost slipping area of the southern fault is located just below the Amatrice coseismic rupture, suggesting a downdip migration of slip (fig. 4.11 or A.1). This holds for the northern main fault as well: as we can see from upper panels of figure 4.10, 4.14 afterslip is concentrated in regions adjacent to the Visso, Norcia and Amatrice coseismic ruptures. As it has already been stated, it is not possible to determine which is the most likely solution of the two final models found, i.e. which is the most likely afterslip distribution on the northern fault. However, they both show an afterslip distribution which is complementary to the coseismic distributions taken into account, in agreement with previous studies (e.g. Gualandi et al., 2014).

In the next images aftershocks have been projected on the activated faults and superimposed to the afterslip distribution of the third (A.3) and fourth model (fig. 5.1, 5.2). The plotted aftershocks have been selected, among a complete catalogue, in a time period starting after the 24^{th} of August 2016 (Amatrice earthquake) and lasting untill March 2018. The seismicity pattern did not occur on a planar surface, therefore the events considered have been projected on the fault planes if they were located in a volume of 1.2 km away from such planes. They have also been filtered to have a $M_w \geq 2$.

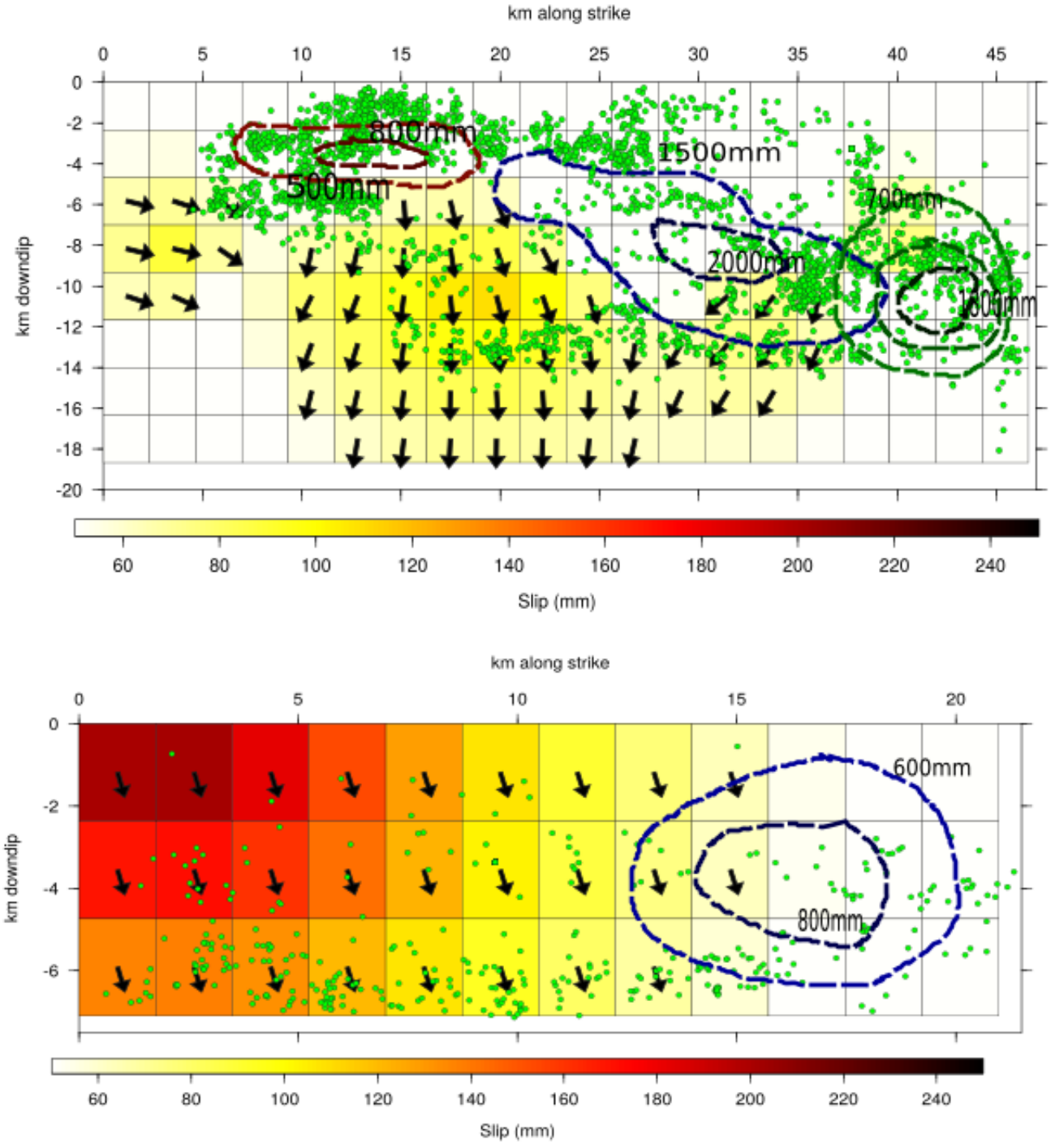

Figure 5.1. Afterslip distribution for the fourth model on the northern and antithetic faults (respectively upper and lower panel). Dashed lines show the co-seismic slip distribution for the Amatrice (green), Visso (red) and Norcia (blue) earthquakes, as in Cheloni et al. (2019). Green dots represent the seismicity recorded after Amatrice earthquake.

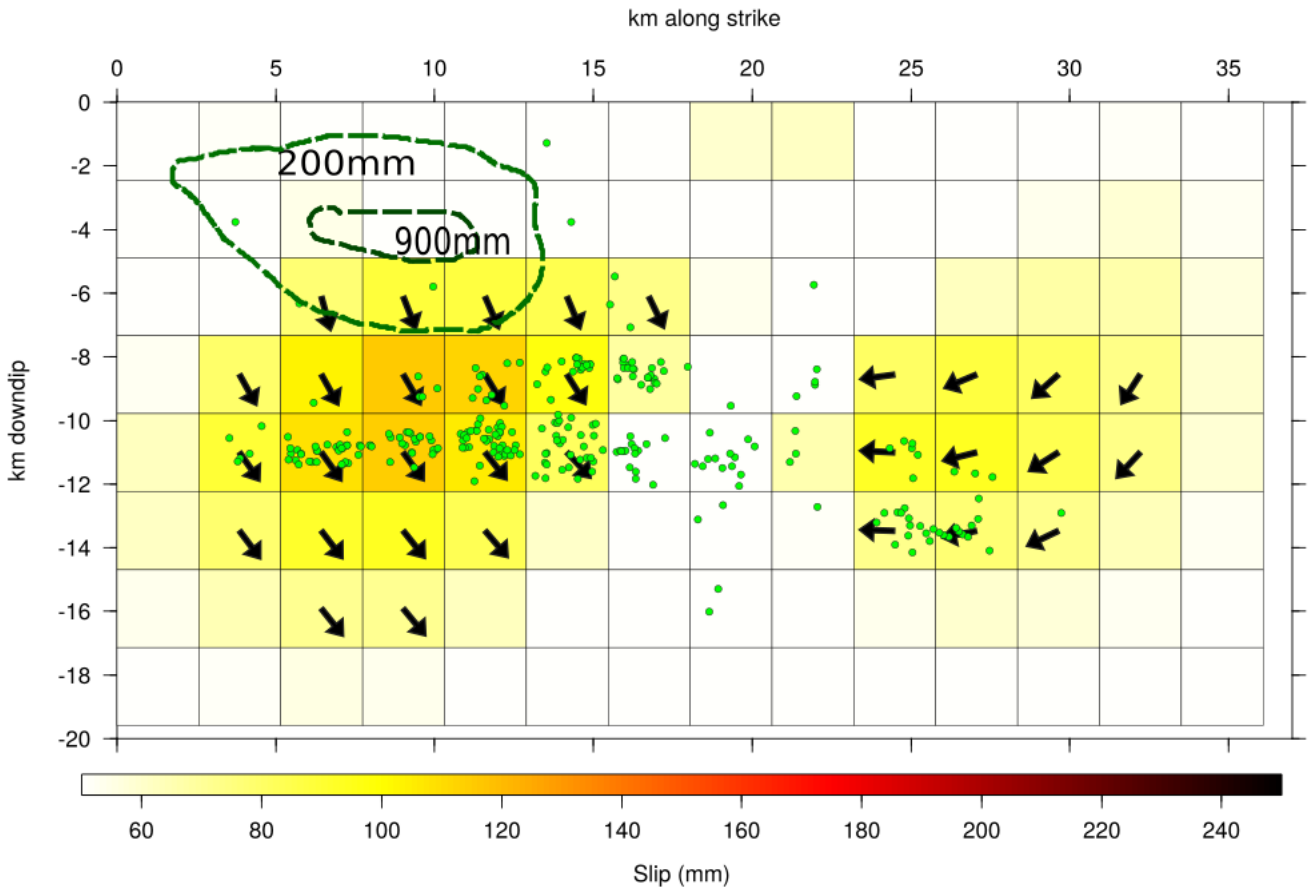

Figure 5.2. Afterslip distribution for the fourth model on the southern fault. Dashed lines and green dots as in figure 5.1.

The total amount of post seismic moment (M_0^{ps}) released in the third and fourth model is respectively 2.58×10^{18} Nm and 3.05×10^{18} Nm, corresponding to $M_w = 6.2$ and $M_w = 6.3$. The seismic sequence, considering all of the events occurred between the 24^{th} of August 2016 and March 2018, released in total a $M_0^{tot} = 9.24 \times 10^{18}$ Nm, which decreases to $M_0^{af} = 6.77 \times 10^{17}$ Nm if we do not consider the Amatrice-Visso-Norcia-January 2017 mainshocks but only the aftershocks contribution.

Since M_0^{ps} embeds the contribution given by the aftershocks, let us introduce an "aseismic moment"

$$M_0^{as} = M_0^{ps} - M_0^{af}$$

which is respectively 1.90×10^{18} and 2.37×10^{18} Nm in the third and fourth model. It is worth noticing that several aftershocks appear to be located near patches involved by afterslip (fig. 5.1, 5.2). Particularly for these aftershocks it is likely that the ICAIM

technique cannot properly separate their contribution to the M_0^{ps}.

Energy during the seismic sequence has been released mainly seismically with a ratio $\gamma = \frac{M_0^{as}}{M_0^{tot}} \sim 21 - 26\%$. Although the seismic sequence was characterized by moderate earthquakes, this value is consistent with what is usually found for large earthquakes ($\gamma \sim 10 - 40\%$, Avouac et al., 2015).

Considering only the energy released by aftershocks, such ratio rises to $\gamma = \frac{M_0^{as}}{M_0^{af}} \sim 280 - 349\%$. This γ is wider than what has been found by Gualandi et al. (2017) for a seismic swarm in the Alto Tiberina fault ($\gamma \sim 70 - 200\%$), on the other hand it is consistent with what has been found by Kyriakopoulos et al. (2013) for a seismic swarm in Greece. In Kyriakopoulos et al. (2013) work $\gamma \sim 298 - 568\%$. One difference between Gualandi et al. (2017) and Kyriakopoulos et al. (2013) estimation is that the latter assumes a constant rigidity modulus (= 30 GPa), as it has been done in this thesis.

In figure 5.3 the normalized cumulative number of aftershocks (recorded after the 24^{th} of August) and the normalized temporal IC1 are compared:

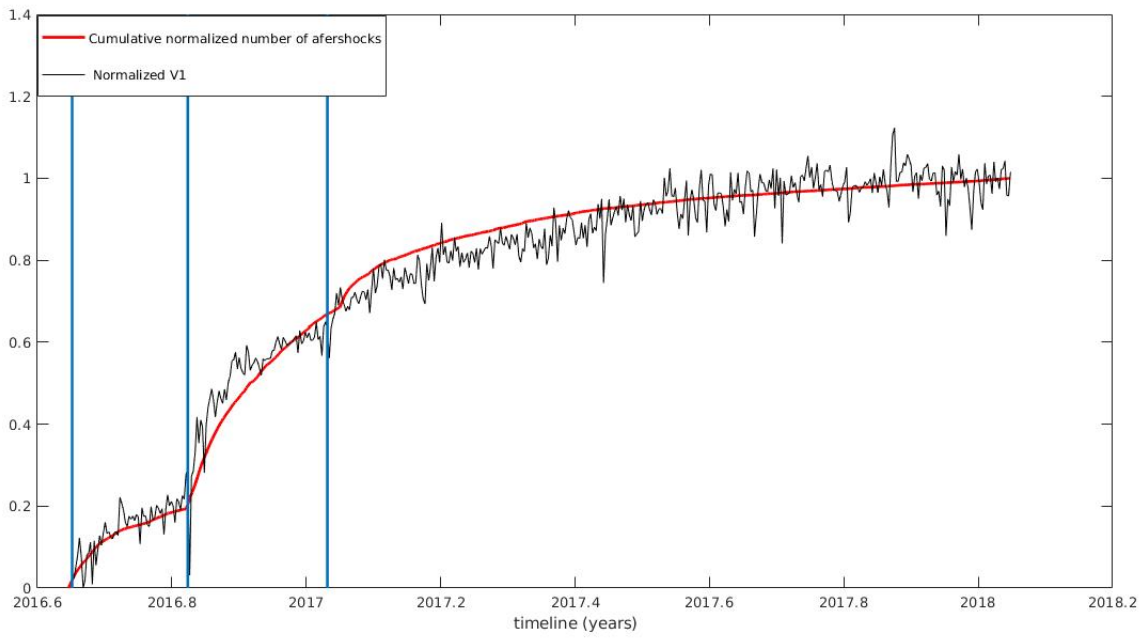

Figure 5.3. It is shown the normalized V_1 and the normalized cumulative number of aftershocks. Vertical lines mark the epoch of mainshocks.

It may be noticed that the number of aftershocks shows a trend similar to the temporal evolution of the post seismic transient: this may suggest that afterslip has triggered aftershocks, i.e. the aftereffect of the physical mechanism (ii) in fig. 1.5 by Rice and Gu (1983) (e.g. Perfettini and Avouac, 2004; Perfettini et al., 2005), in agreement with the fact that the M_0^{af} released by the aftershocks is smaller than the post seismic moment of the final models M_0^{as} (Perfettini et al., 2007). According to Perfettini et al. (2007), the aftershocks mainly occur close to the zone which ruptured coseismically and the post seismic deformation increases stress changes in areas already brought close to rupture during the mainshocks both in the vicinity of the coseismic rupture and farther away. As a matter of fact, the majority of the aftershocks are located either close to the coseismic slipping areas (upper panel of figure 5.1) or close to the patches with the highest amount of afterslip (figures 5.1 and 5.2).

To sum up, the study of the post seismic deformation that followed the 2016 seismic sequence of Central Italy led to the following conclusive remarks:

1. This sequence was characterized by three post seismic transients highlighted in figures 3.9 and 3.10, with characteristic decay time summarized in table 3.2. However, the vbICA technique allowed us to separate only one post seismic transient for the whole sequence and failed in recognizing a signal for each of the three main events.

2. The simple geometry of faults employed in this thesis was capable of satisfactorily reproducing the ICA reconstruction of ground displacement recorded at GPS stations (figures 4.17 4.18).

3. Two afterslip distributions properly model the ICA reconstruction, the main difference laying in the distribution on the northern fault (upper panel of fig. 4.10 and fig. 4.14). Both solutions show an afterslip distribution on the masterfaults complementary to the coseismic solution proposed by Cheloni et al. (2017, 2019), as shown in figures 4.10, 4.11, 4.14, A.1. The afterslip on the antithetic fault partly overlaps with the one detected by the SAR interferogram exploited by Cheloni at al. (2017, 2019). Although Cheloni et al. proposed a coseismic solution, the SAR acquisition is likely to embed an early post seismic constribution as well.

4. Afterslip on the antithetic fault is well constrained by the Arquata station, near which some poroelastic contribution cannot be ruled out (Pousse-Beltrand et al., 2018). Since this mechanism mainly affects vertical components of ground displacement (e.g. Barri et al., 1997; Chen, 2011), it could be worth to compare our solution with the one that can be obtained by applying ICAIM to the observed horizontal components only, which is a possible development of the present study.

5. Energy, if we consider the whole seismic sequence, has been released mainly seismically with a ratio $\gamma = \frac{M_0^{as}}{M_0^{tot}} \sim 21 - 26\%$; however if we compare it with the energy released by aftershocks it rises to $\gamma = \frac{M_0^{as}}{M_0^{af}} \sim 280 - 349\%$. This suggests, together with the similarity of the temporal evolution of the post seismic transient with the cumulative number of aftershocks (fig. 5.3), that afterslip might have driven the aftershock evolution.

Bibliography

1. Aringoli, D. et al. The August 24th 2016 Accumoli earthquake: surface faulting and Deep-Seated Gravitational Slope Deformation (DSGSD) in the Monte Vettore area. Annals of Geophysics (2016). doi:10.4401/ag-7199

2. Avouac, J.-P. (2015), From geodetic imaging of seismic and aseismic fault slip to dynamic modeling of the seismic cycle, Annu. Rev. Earth Planet. Sci., 43, 233–71, doi:10.1146/annurev-earth-060614-105302.

3. Barry S. I., Mercer G. N., and Zoppou C., "Deformation and fluid flow due to a source in a poro-elastic layer," Applied Mathematical Modelling, vol. 21, no. 11, pp. 681–689, 1997.

4. Boehm, J., Niell, A., Tregoning, P. and Schuh, H. Global Mapping Function (GMF): A new empirical mapping function based on numerical weather model data. Geophys. Res. Lett. 33, L07304 (2006).

5. Cheloni, D. et al. GPS observations of coseismic deformation following the 2016, August 24, Mw 6 Amatrice earthquake (central Italy): data, analysis and preliminary fault model. Annals of Geophysics (2016). doi:10.4401/ag-7269

6. Cheloni, D., Falcucci, E., Gori, S., 2019. Half-Graben Rupture Geometry of the 30 October 2016 M W 6.6 Mt. Vettore-Mt. Bove Earthquake, Central Italy. J. Geophys. Res. Solid Earth 124, 4091–4118. https://doi.org/10.1029/2018JB015851

7. Chen, Z. R., 2011, Poroelastic model for induced stresses and deformations in hydrocarbon and geothermal reservoirs:JournalPetroleum Science Engineering, Vol. 80, No. 1, pp. 41–52.

8. Chiaraluce, L. et al. The Alto Tiberina Near Fault Observatory (northern Apennines, Italy). 57, (2014).

9. Chiaraluce, L. et al. The 2016 Central Italy Seismic Sequence: A First Look at the Mainshocks, Aftershocks, and Source Models. Seismological Research Letters 88, 757–771 (2017).

10. Civico, R. et al. Surface ruptures following the 30 October 2016 Mw 6.5 Norcia earthquake, central Italy. Journal of Maps 14, 151–160 (2018).

11. Coltorti, M. and Farabollini, P. Quaternary evolution of the Castelluccio di Norcia basin (Umbro-Marchean Apennines, Italy). 8, (1995).

12. D. Dong, P. Fanf, Y. Bock, M. K. Cheng, and S. Miyazaki J. G. R. - Anatomy of apparent seasonal variations from GPS-derived site position time series - Vol. 107, No. B4, doi:10.1029/2001JB000573, 2002

13. Delouis, B., Nocquet, J.-M. and Vallée, M. Slip distribution of the February 27, 2010 Mw = 8.8 Maule Earthquake, central Chile, from static and high-rate GPS, InSAR, and broadband teleseismic data: SLIP DISTRIBUTION MAULE EARTHQUAKE. Geophys. Res. Lett. 37, n/a-n/a (2010).

14. Dixon TH. 1991. An introduction to the Global Positioning System and some geological applications. Rev. Geophys. 29:249–76

15. Floyd et al-2016-Geophysical Research Letters.

16. Gualandi, A., Serpelloni, E. and Belardinelli, M. E. Space–time evolution of crustal deformation related to the Mw 6.3, 2009 L'Aquila earthquake (central Italy) from principal component analysis inversion of GPS position time-series. Geophysical Journal International 197, 174–191 (2014).

17. Gualandi, A., C. Nichele, E. Serpelloni, Chiaraluce, L. Anderlini, D. Latorre, M. E. Belardinelli, and J.-P. Avouac (2017), Aseismic deformation associated with an earthquake swarm in the northern Apennines (Italy), Geophys. Res. Lett., 44, doi:10.1002/2017GL073687.

18. Hager BH, King RW, Murray MH. 1991. Measurement of crustal deformation using the Global Positioning System. Annu. Rev. Earth Planet. Sci. 19:351–8

19. Hsu, Y.-J., M. Simons, J.-P. Avouac, J. Galetzka, K. Sieh, M. Chlieh, D. Natawidjaja, L. Prawirodirdjo, and Y. Bock (2006), Frictional afterslip following the 2005 Nias-Simeulue earthquake, Sumatra, Science, 312, 1921– 1926.

20. Johnson, K.M., 2006. Frictional Properties on the San Andreas Fault near Parkfield, California, Inferred from Models of Afterslip following the 2004 Earthquake. Bulletin of the Seismological Society of America 96, S321–S338. https://doi.org/10.1785/0120050808

21. Kyriakopoulos, C., M. Chini, C. Bignami, S. Stramondo, A. Ganas, M. Kolligri, and A. Moshou (2013), Monthly migration of a tectonic seismic swarm detected by DInSAR: southwest Peloponnese, Greece, Geophys. J. Int., 194, 1302–1309, doi:10.1093/gji/ggt196.

22. Kositsky, A.P., Avouac, J.-P., 2010. Inverting geodetic time series with a principal component analysis-based inversion method. J. Geophys. Res. 115, B03401. https://doi.org/10.1029/2009JB006535

23. Lin, Y. N., Kositsky, A. P. and Avouac, J.-P. PCAIM joint inversion of InSAR and ground-based geodetic time series: Application to monitoring magmatic inflation beneath the Long Valley Caldera: PCAIM JOINT INVERSION. Geophys. Res. Lett. 37, n/a-n/a (2010).

24. Livio, F. A. et al. Surface faulting during the August 24, 2016, Central Italy earthquake (Mw 6.0): preliminary results. Annals of Geophysics (2016). doi:10.4401/ag-7197

25. Marone C. J., C. H. Scholz, and R. Bilham (1991), On the mechanics of earthquake afterslip, J. Geophys. Res., 96, 8441 – 8452

26. Mavrommatis, A. P., Segall, P. and Johnson, K. M. A decadal-scale deformation transient prior to the 2011 M w 9.0 Tohoku-oki earthquake: MAVROMMATIS ET AL. Geophys. Res. Lett. 41, 4486–4494 (2014).

27. Nespoli M., Belardinelli M.E., Gualandi A., Serpelloni E., and Maurizio Bonafede, "Poroelasticity and Fluid Flow Modeling for the 2012 Emilia-Romagna Earthquakes: Hints from GPS and InSAR Data," Geofluids, vol. 2018, Article ID 4160570, 15 pages, 2018. https://doi.org/10.1155/2018/4160570.

28. Okada, Y. Surface deformation due to shear and tensile faults in a half-space. Bulletin of the Seismological Society of America 75, 1135–1154 (1985).

29. Perfettini, H., Avouac, J.-P., 2004. Postseismic relaxation driven by brittle creep: A possible mechanism to reconcile geodetic measurements and the decay rate of aftershocks, application to the Chi-Chi earthquake, Taiwan: DYNAMICS OF BRITTLE CREEP. J. Geophys. Res. 109. https://doi.org/10.1029/2003JB002488

30. Perfettini H., Avouac J.-P. Modeling afterslip and aftershocks following the 1992 Landers earthquake https://doi.org/10.1029/2006JB004399

31. Perfettini, H., J.-P. Avouac, and J.-C. Ruegg (2005), Geodetic displacements and aftershocks following the 2001 Mw = 8.4 Peru earthquake: Implications for the mechanics of the earthquake cycle along subduction zones, J. Geophys. Res., 110, B09404, doi:10.1029/2004JB003522.

32. Petitta, M., Mastrorillo, L., Preziosi, E. et al. Hydrogeol J (2018) 26: 1009. https://doi.org/10.1007/s10040-017-1717-7

33. Radiguet, M. et al. Spatial and temporal evolution of a long term slow slip event: the 2006 Guerrero Slow Slip Event: Evolution of the 2006 Guerrero SSE. Geophysical Journal International 184, 816–828 (2011).

34. Rice, J.R., n.d. Earthquake aftereffects and triggered seismic phenomena 33.

35. Savage J.M., Svarc J.L., Prescott W.H., 2003. Near-field postseismic deformation associated with the 1992 Landers and 1999 Hector Mine, California, earthquakes J. geophys. Res. 108B92432 doi: arXiv:astro-ph/10.1029/2002JB002330

36. Scholz, C. Brittle Tectonics: A Non-linear Dynamical System. (2014). doi:10.1007/978-0-387-30440-3-44

37. Segall, P. and J.L. Davis (1997). GPS applications for geodynamics and earthquake studies. Annu. Rev. Earth Planet.

38. Serpelloni, E., Faccenna, C., Spada, G., Dong, D. and Williams, S. D. P. Vertical GPS ground motion rates in the Euro-Mediterranean region: New evidence of velocity gradients at different spatial scales along the Nubia-Eurasia plate boundary: GPS VERTICAL DEFORMATION IN EUROPE. J. Geophys. Res. Solid Earth 118, 6003–6024 (2013).

39. Serpelloni, E., Casula, G., Galvani, A. and Baldi, P. - Data analysis of permanent GPS networks in Italy and surrounding regions: application of a distributed preocessing approach.

40. Serpelloni E., Pintori F., Gualandi A., Scoccimarro E., Cavaliere A., Anderlini L., Belardinelli M. E., Todesco M.: Hydrologically Induced Karst Deformation: Insights From GPS Measurements in the Adria-Eurasia Plate Boundary Zone.

41. Srebro, N. and Jaakkola, T. Weighted Low-Rank Approximations. 8

42. Tarantola A. - Inverse Problem Theory and Methods for Model Parameter Estimation - SIAM, 2005

43. Tinti, E., Scognamiglio, L., Michelini, A. and Cocco, M. Slip heterogeneity and directivity of the M L 6.0, 2016, Amatrice earthquake estimated with rapid finite-fault inversion: Rupture Process of 2016 Amatrice Event. 43, (2016).

44. W.G, E. et al. Coseismic effects of the 2016 Amatrice seismic sequence: first geological results. Annals of Geophysics (2016). doi:10.4401/ag-7195

45. Walters, R. J. et al. Dual control of fault intersections on stop-start rupture in the 2016 Central Italy seismic sequence. Earth and Planetary Science Letters 500, 1–14 (2018).

Appendices

Appendix A

Figures

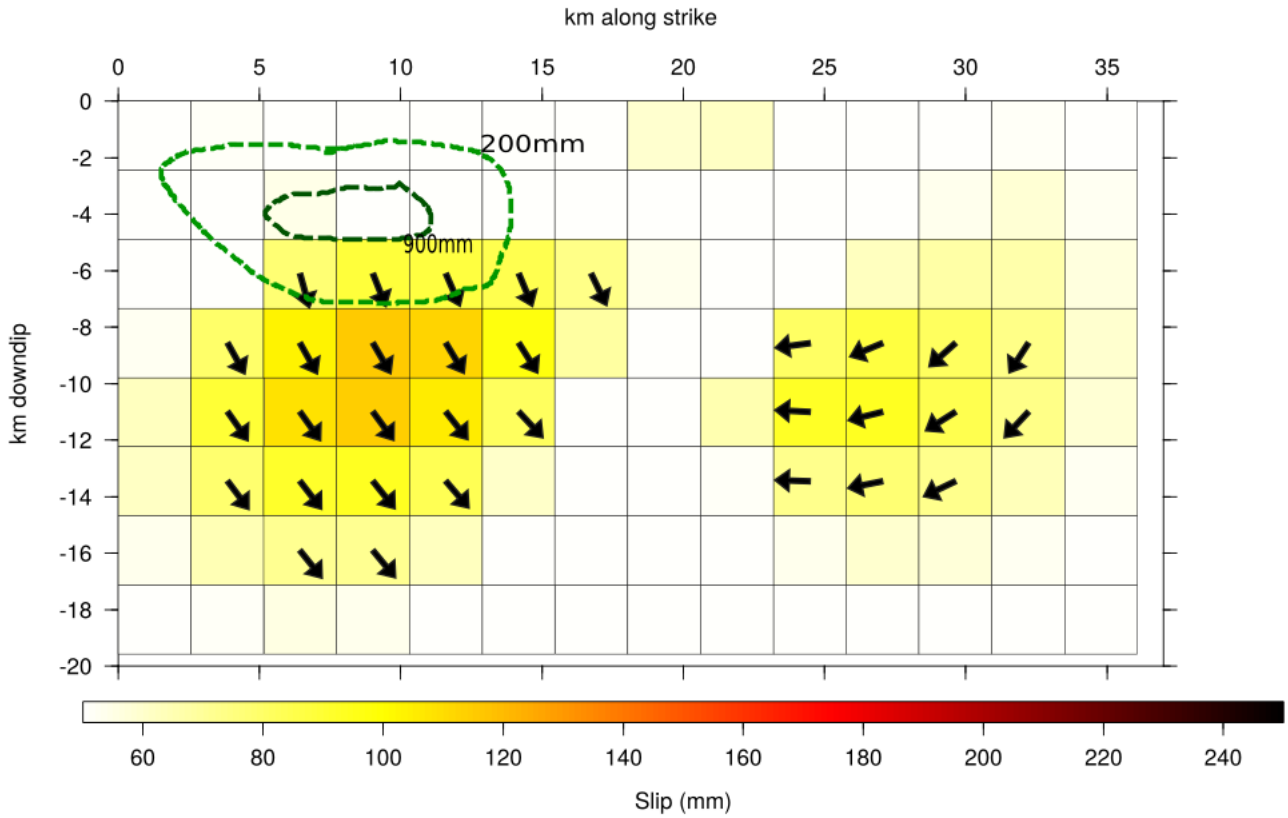

Figure A.1. Afterslip distribution for the fourth model on the southernmost masterfault in a strike-dip reference system. Rake is plotted only for those patches exceeding 30% of maximum slip. Dashed lines show the co-seismic slip distribution for the Amatrice (green), Visso (red) and Norcia (blue) earthquakes, as in Cheloni et al. (2019).

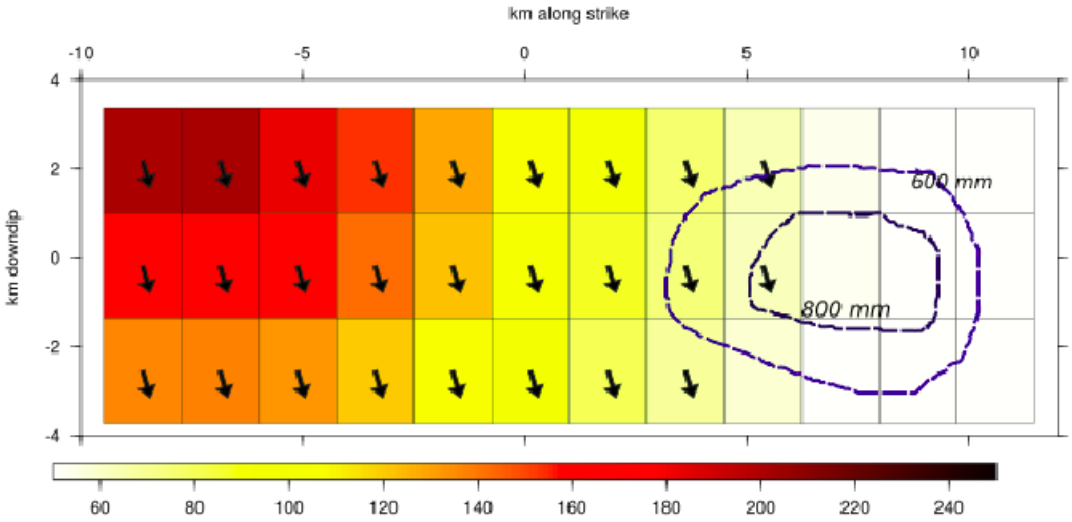

Figure A.2. Afterslip distribution on the antithetic fault for the fourth model in a strike-dip reference system. Rake is plotted only for those patches exceeding 30% of maximum slip. Dashed lines show the co-seismic slip distribution for the Amatrice (green), Visso (red) and Norcia (blue) earthquakes, as in Cheloni et al. (2019).

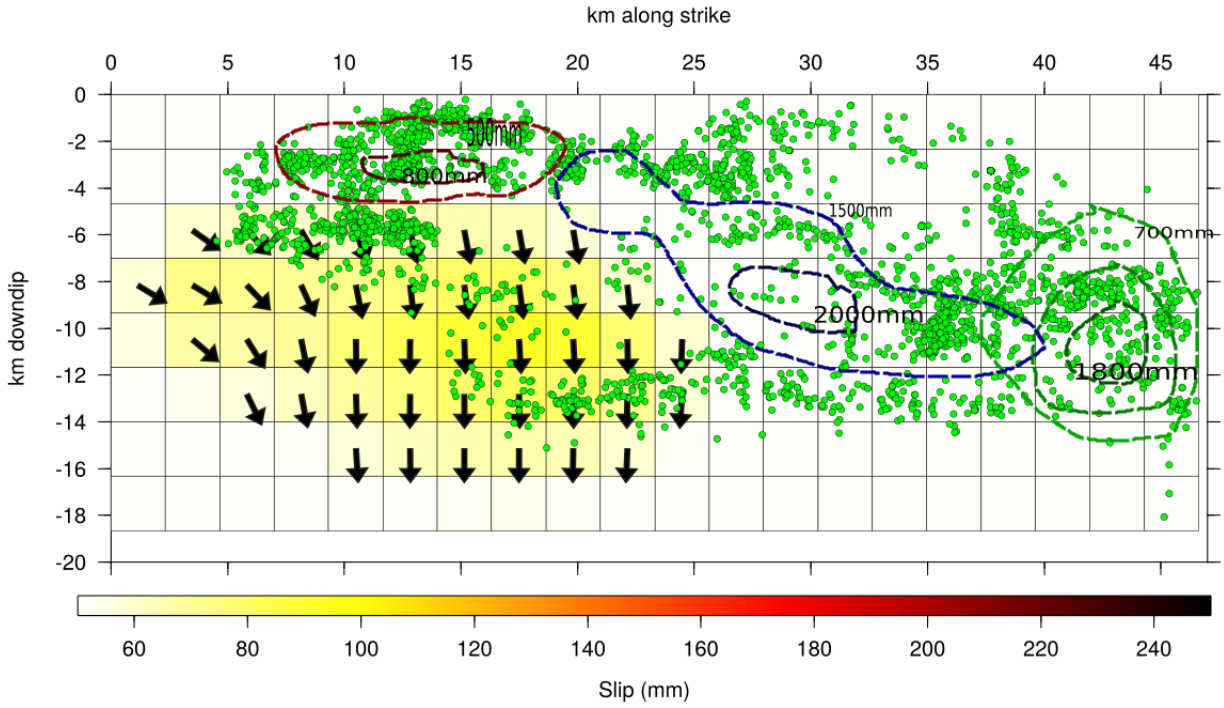

Figure A.3. Afterslip distribution for the third model on the northern fault. Green dots represent the seismicity recorded after Amatrice earthquake. Dashed lines show the co-seismic slip distribution for the Amatrice (green), Visso (red) and Norcia (blue) earthquakes, as in Cheloni et al. (2019).

Appendix B

GPS Stations list

NAME	LONGITUDE (°)	LATITUDE (°)
'ACCU'	13.2412	42.6961
'ALAT'	13.3835	41.6729
'ALPA'	12.6114	41.7224
'AMAT'	13.2924	42.6265
'ANCG'	13.5020	43.6028
'APRI'	12.6646	41.5968
'ARCE'	12.9494	43.5049
'ARDE'	12.5367	41.6122
'AREZ'	11.8749	43.4637
'ARQT'	13.1987	42.7550
'ASC9'	13.6061	42.8521
'ASCC'	13.5930	42.8573
'ATBU'	12.5478	43.4760
'ATFO'	12.5671	43.3701
'ATLO'	12.4071	43.3151
'ATMI'	12.2673	43.3340
'ATTE'	12.3505	43.1998
'BGDR'	11.8949	43.8891
'BLRA'	13.5603	41.8103
'CAFI'	11.9662	43.3292
'CAM9'	13.0708	43.1439
'CAMU'	11.9775	43.2589
'CASP'	10.8652	42.7908
'CECI'	10.5266	43.3110
'CERT'	12.9818	41.9491
'CESI'	12.9046	43.0050
'CIST'	12.8293	41.5840
'CIT2'	12.2479	43.4671
'CIVI'	11.9386	44.0066
'CSSB'	12.2454	43.2093
'CVTX'	11.7973	42.0952
'FALC'	13.3583	43.6401
'FIAN'	12.5877	42.1644
'FIGL'	11.4735	43.6187

NAME	LONGITUDE (°)	LATITUDE (°)
'FIUM'	12.2301	41.7715
'FOL1'	12.6988	42.9549
'FOND'	13.4149	41.3299
'FONX'	13.4321	41.3560
'FOSS'	12.8066	43.6890
'FRMO'	13.7314	43.1684
'FROX'	13.3466	41.638 0
'FRRA'	14.2922	42.4177
'GAVO'	10.8889	42.9366
'GEOT'	13.5110	43.5745
'GINE'	13.3764	43.1206
'GNAL'	13.5198	42.5837
'GRAM'	13.8705	42.9755
'GRO9'	13.8749	42.9684
'GROA'	11.1093	42.7818
'GROS'	11.1052	42.7659
'GRTM'	13.8450	42.9798
'GUAR'	13.3122	41.7944
'GUB2'	12.5775	43.3510
'GUMA'	13.3352	43.0628
'IGMI'	11.2138	43.7956
'INGR'	12.5148	41.8281
'ITGS'	13.7439	43.2450
'ITRA'	14.0018	42.6585
'ITRN'	12.5831	44.0486
'LANC'	14.3805	42.1983
'LARN'	12.8330	41.7281
'LAT1'	12.9014	41.4708
'LNSS'	13.0402	42.6028
'LPEL'	14.1832	42.0469
'LTNA'	12.9048	41.4673
'M0SE'	12.4933	41.8931
'MAC8'	13.4393	43.2931
'MACE'	13.4509	43.2941
'MAG9'	13.5878	43.1383
'MAON'	11.1307	42.4282
'MAR8'	11.8680	42.0364
'MCIN'	11.4890	43.0582
'MLAG'	12.7787	43.4309
'MOCX'	11.6040	42.3536
'MOIE'	13.1235	43.5032
'MON'	13.3371	42.8968
'MORO'	12.6190	42.0525
'MRRA'	13.9160	42.8853
'MTER'	13.2143	42.5088
'MTRA'	13.2400	42.5278
'MTTO'	12.9927	42.4555

NAME	LONGITUDE (°)	LATITUDE (°)
'MUR1'	12.5247	43.2632
'MVAL'	12.4066	43.3821
'NEMI'	12.7176	41.7177
'NETT'	12.6475	41.4607
'NOV2'	12.2912	43.8962
'NOV9'	12.2906	43.8947
'OCRA'	13.0390	42.0495
'OLGI'	12.3551	42.0547
'OTRA'	13.6460	41.9549
'OVRA'	13.5151	42.1376
'PAGL'	14.4981	42.1644
'PBRA'	14.2285	42.1242
'PEN2'	12.2651	43.8173
'PES2'	12.8927	43.8934
'PIBI'	12.4531	43.1279
'PIET'	12.4019	43.4507
'PIN3'	14.0144	42.6436
'PIO9'	12.4824	43.6117
'PIOB'	12.5261	43.6075
'PREC'	13.0399	42.8453
'PSAN'	14.1390	42.5188
'PSST'	11.1201	42.4280
'PSTE'	11.1201	42.4280
'PULC'	11.8162	43.1551
'RASS'	11.8356	43.6468
'RDPI'	12.7103	41.7604
'RIET'	12.8571	42.4076
'RIFL'	12.4811	42.2100
'RMES'	12.5535	44.0518
'RMPO'	12.7032	41.8111
'ROAN'	12.4195	41.9037
'ROUN'	12.4937	41.8932
'RSM1'	12.4453	43.9356
'RSMN'	12.4507	43.9335
'RSTO'	14.0015	42.6584
'RUBI'	12.4091	44.1501
'SCRA'	14.0021	42.2681
'SENI'	13.2150	43.7076
'SIE9'	11.3314	43.3485
'SULM'	13.9259	42.0429
'TARQ'	11.7575	42.2539
'TER1'	13.7004	42.6621
'TERA'	13.6981	42.6571
'TERI'	12.6495	42.5670
'TOD3'	12.4098	42.7875
'TOLF'	12	42.0640
'UMBE'	12.3286	43.3112

NAME	LONGITUDE (°)	LATITUDE (°)
'UNPG'	12.3557	43.1194
'UNUB'	12.6402	43.7005
'VALC'	12.2849	43.2790
'VALM'	12.9178	41.7755
'VIT9'	12.1116	42.4194
'VIVA'	12.8916	42.0154
'VLPN'	10.8521	43.0056
'VRRA'	10.8651	43.4007
'VTRA'	14.7079	42.1104
'VVLO'	13.6232	41.8696
'ZAG9'	12.7478	41.8624